TU Delft

Structural assessment of a calcium silicate element masonry assemblage using an equivalent frame modelling approach

Master Thesis

Oana Veronica Damian

June, 2018

Structural assessment of a calcium silicate element masonry assemblage using an equivalent frame modelling approach

Department of Building Engineering

Faculty of Civil Engineering and Geosciences

Delft University of Technology

Personal details

Oana Veronica Damian

Graduation committee:

Prof. Dr. Ir. J.G. Rots, *Faculty of Civil Engineering and Geosciences*

Dr.ir. H.R. Schipper, *Faculty of Civil Engineering and Geosciences*

Dr. Rita Esposito, *Faculty of Civil Engineering and Geosciences*

Preface

This thesis is written in order to obtain my Master Degree in Building Engineering at Delft University of Technology. The subject of this report focuses on the structural assessment of a calcium silicate element masonry assemblage using an equivalent frame modelling approach. The research is carried out under the guidance of Delft University of Technology. The experimental tests reported in this thesis and used as benchmark for the model validation were part of an experimental campaign funded by NAM (contract number UI63654). Technosoft supported with the license of the 3Muri software.

I would like to thank my graduation committee for their helpful advice and for their guidance throughout this process. I would also like to thank my family and friends for their support.

Oana Veronica Damian

Summary

In the last few years, a significant increase in the seismic activity has been observed in the northern part of the Netherlands (Groningen region) due to geo-resources exploitation. This raised the need of assessing the current building stock, which is mainly made of low-rise unreinforced masonry structures. In order to fulfil this objective, an extensive testing campaign has been developed at TU Delft that aims to provide a well-documented benchmark that can be further used in the development of numerical models.

The case study of this thesis is a typical Dutch terraced house built after 1980 and made of calcium silicate element masonry. The main research objective focuses on the structural assessment of an unreinforced masonry house using an equivalent frame (EF) modelling approach. The thesis aims to prove the effectiveness of this method in predicting the structural behavior. This simplified analysis approach is preferred because it can capture the behavior of a structure with a significant reduction in computational time and effort. Moreover, other studies presented in literature show that the equivalent frame model can be successfully used to predict the structural behavior under lateral loads.

The EF modelling approach is based on the principle that every structural element, such as piers and spandrels, can be represented by an equivalent beam element. The approach is mainly suitable to describe the behaviour of structures with regular geometry for which the in-plane failure is the predominant failure mechanism. In this thesis work, the commercial software 3Muri is used.

As a first step, the EF model is calibrated by simulating the in-plane response of single piers. The comparison between experimental and numerical results gives a good agreement in terms of lateral capacity and failure mechanism. This calibration phase allows setting the modelling choices used in the analysis of the assembled structure.

In order to evaluate the performances of the EF model, the quasi-static cyclic pushover tests on a masonry assembled structure is simulated. A model sensitivity study is performed to investigate the effect of different modelling choices. The main aspects studied are: the coupling between the piers in the facades (frame effect), the distribution of the floor load on the piers and the flange effect due to the interaction between the transversal walls and the piers.

The analyses performed show that the level of coupling and interaction between the piers is one of the most important parameters that defines the structural behavior. In the case of the analysed structure, the absence of spandrels highlighted the need of ad-hoc modelling choices to simulate the coupling between the piers in the façades. During the lateral deformation, the floor acts as a rigid horizontal element allowing for the formation of a portal effect. However, in the EF modelling approach the contribution of the floor is not considered in these terms. To simulate this effect, fictitious beam elements have been introduced in the 3D model to simulate the coupling between the piers; their stiffness is varied to study the effect of a weak and strong coupling. In comparison with experimental results, a weak coupling between piers leads to an underestimation of the lateral force capacity and a different failure mechanism. On the contrary, assuming a stronger coupling between piers leads to better approximation of the behaviour in terms of both force and displacement capacity as well as failure mechanism. Consequently, the coupling between the façade piers plays an important role on the structural response.

Since the overburden can influence the in-plane response of piers, the initial distribution of the floor load on the piers has been studied. Variations have been carried out considering the floor as a unidirectional slab spanning between the transversal walls, a bidirectional slab or a unidirectional slab spanning between the façades. As expected, when the load distribution on the piers is increased, the lateral capacity of the structure increases, both in terms of total base shear force and ultimate displacements. Considering the case of a bidirectional floor provides the best approximation of experimental results. It has been noticed that a large variation in axial force is obtained during the analysis as a consequence of the rocking of the piers. This effect leads to a complete uplift of the floor with respect to the transversal walls. However, this behavior does not occur in the real structure and thus the force redistribution considered by the EF model affects the bending capacity of the piers, leading to a different failure mechanism and unreliable results.

In order to exclude any undesired uplift of the floor and to consider the contribution of the transversal walls to the in-plane response of the façade piers, a 2D model considering the flange effect is adopted. In the 2D model, the transversal walls are replaced by fictitious walls without stiffness and the flange effect is considered as an additional vertical load. The 2D model analysis predicts the correct failure mechanism. By daring the flange length, variation in the estimate of the force and displacement capacity are observed. The best approximation of the experimental results is obtained by considering a flange length equal to 6 times the thickness of the adjacent pier.

To evaluate the accuracy of the EF model, a comparison with the simplified lateral mechanism analysis ("SLaMA") approach is performed. The analytical results are in agreement with the numerical results of the EF model and the SLaMA method offers a good indication of the most vulnerable elements in the structure and the most probable failure mechanism that can develop.

The EF model results are underestimated due to the simplified assumptions that are made throughout the modelling process and analysis. The uncertainties encountered during the modelling process are mainly related to the software limitations. Further research is necessary in this direction, so that more modelling aspects will be possible in 3Muri, such as the possibility to define and compute the flange effect of intersecting walls. It is also recommended that further research focuses on other types of masonry buildings, so that a more exhaustive conclusion on the ability of the EF model approach can be obtained.

Table of Contents

List of figures

List of tables

1 Introduction

The Netherlands is historically not characterized by a strong natural seismicity and thus the earthquake research and the effect of seismic actions on the existing buildings is negligible. However, an increased frequency of minor earthquakes caused by geo-resources exploitation that has been registered in the northern part of the Netherlands over the last few years (van der Voort & Vanclay, 2015) has raised the need of assessing the existing structures.

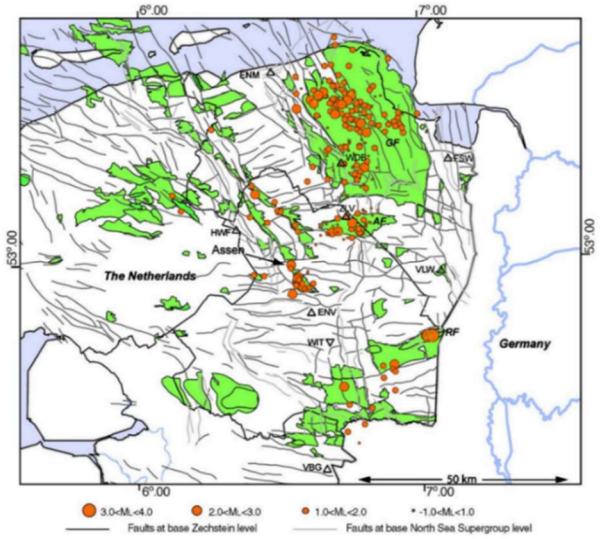

Figure 1.1 Gas exploitation (green) and seismicity (orange circles) in the northern part of The Netherlands (Van Eck, Goutbeek, Haak, & Dost, 2006)

The vast majority of the building stock in Netherlands is composed of unreinforced masonry and is not designed to withstand seismic loading. Calcium silicate element masonry is often used for structural walls in unreinforced masonry houses across areas characterized by a low seismic activity and has been frequently used in the Netherlands starting with 1980's, especially in the construction of terraced houses (Figure 1.2).

Figure 1.2 Typical terraced Dutch houses (Muir, Beazley, Jury, Kam, & den Hertog, 2017)

The occurrence of small earthquakes in the area extended the need for the evaluation of the structural behavior of the existing unreinforced masonry houses. To fulfil this objective, an extended campaign including laboratory tests on masonry components and cyclic pushover tests on full-scale assembled structures has been developed at TU Delft. These tests can provide an exhaustive description of the mechanical properties and behavior of structural components and masonry assemblies.

During the month of February 2017, a full-scale masonry structure was tested to determine the structural response of the construction under quasi-static cyclic loading. The experiment also provided information regarding the capacity and ductility of the structure, as well as the crack initiation and propagation. The aim of the test was to provide a well-documented benchmark that can be further used for numerical analysis. Predicting the structural response of existing unreinforced masonry buildings can be difficult and the process requires numerical models and analytical design methods that need to be validated by experimental results.

1.1 Research objective and strategy

The report focuses on the structural assessment of an unreinforced masonry structure using an equivalent frame (EF) model. Due to their simple approach and reduced computational costs, EF models are often used in engineering practice for the seismic assessment of buildings. In this thesis work, their accuracy and efficiency is evaluated to simulate the response of an assembled structure representative of a typical modern Dutch terraced house. The software 3Muri Ver. 11.0.8. is used for the numerical analysis.

This research is centered around the quasi-static cyclic pushover test performed on the calcium silicate element masonry assemblage at TU Delft during the large-scale testing campaign 2016/2017. The experimental results are used for the calibration and validation of the EF model. First, the EF model is calibrated based on the results of the in-plane tests on single components. After that, the model is used to simulate the behavior of the assembled structure; a parametric study is performed to evaluate the influence of different modelling choices (Figure 1.3).

Additionally, analytical calculations are performed to validate the numerical results.

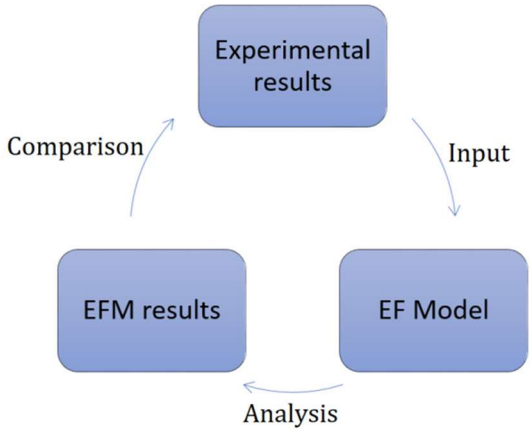

Figure 1.3 Research strategy

The main research question of this thesis work is:

> *How effective is the equivalent frame model for predicting the structural response of unreinforced masonry structures?*

The question is approached from different perspectives that can be formulated in the following sub-questions:

- What are the main in-plane failure mechanisms of masonry piers when they are integrated in a structure?
- How is the structural behavior of the piers influenced by the other structural components, such as floor and transversal walls?
- What are the main parameters influencing the global structural behavior?

1.2 Structure of the report

An overview of each section of the thesis is presented below:

- *Chapter 1* represents an introductory section and offers a description of the main research question, as well as an overview of the thesis.
- *Chapter 2* is part of the literature study and provides a short description of the behavior of unreinforced masonry at material and component level. Special attention is given to the case of calcium silicate element masonry.
- *Chapter 3* presents a summary of the different modelling approaches that can be used to simulate the behavior of masonry structures. These modelling techniques range from simple

techniques (Equivalent Frame Method), to more complex models (micro-modelling). A more detailed description of the equivalent frame (EF) model approach is provided, together with a short overview of other studies on unreinforced masonry structures using the same analysis approach.

- *Chapter 4* focuses on the methods used for modelling the seismic behavior and presents a summary of the different approaches that can be found in literature regarding the structural assessment of masonry structures under seismic loading.

- *Chapter 5* focuses on the case study and describes the experimental results of the tests performed at TU Delft on the full-scale calcium silicate element masonry walls subjected to quasi-static cyclic in-plane loading and on the full-scale calcium silicate element masonry assemblage.

- *Chapter 6* presents the calibration of the EF model against the experimental findings obtained from the in-plane tests on single walls. The numerical results are verified also by means of analytical calculations in terms of force capacity.

- *Chapter 7* presents the analysis of the assembled structure by means of the calibrated EF model. A parametric study is carried out investigating the effect of: the coupling between the façades piers, the floor load distribution on the piers and the flange effect due to the interaction between transversal walls and façades piers.

- *Chapter 8* presents the simplified lateral mechanism analysis (SLaMA) approach. This analytical approach is compared with the numerical results of Chapter 7 and with the experimental results.

- *Chapter 9* concludes the thesis by summarizing the main outcomes of the research and by providing suggestions for future research.

2 Masonry behavior

2.1 Masonry typology

Masonry is a material composed of individual units bonded together by mortar. Due to the simplicity of the construction technique, this material is still being widely used today.

The most common materials for masonry units are clay, stone (limestone, marble and granite), concrete or even glass blocks, while the mortar is a mixture of cement, lime, sand and water in various combinations. As a consequence, masonry can have different properties depending on the mechanical property and composition of the constituents, as well as on the size of the individual units, the joint thickness and arrangement of brick units. (Mosalam, Glascoe, & Bernier, 2009)

Depending on the construction method used, masonry can be classified as it follows:

- Unreinforced masonry (URM), which consists of masonry walls without steel reinforcing bars embedded within them (Figure 2.1, a).
- Reinforced masonry, where steel reinforcing bars are embedded within the masonry walls (Figure 2.1, b).
- Confined masonry (e.g. infill), where masonry walls have vertical and horizontal reinforced concrete elements built on all four sides of the wall panel (Figure 2.1, c).

While for the reinforced masonry and confined masonry, steel and concrete play a role in the behavior of the masonry, for the unreinforced masonry, the interaction between units and mortar is the governing parameter for the behavior of the entire masonry structure.

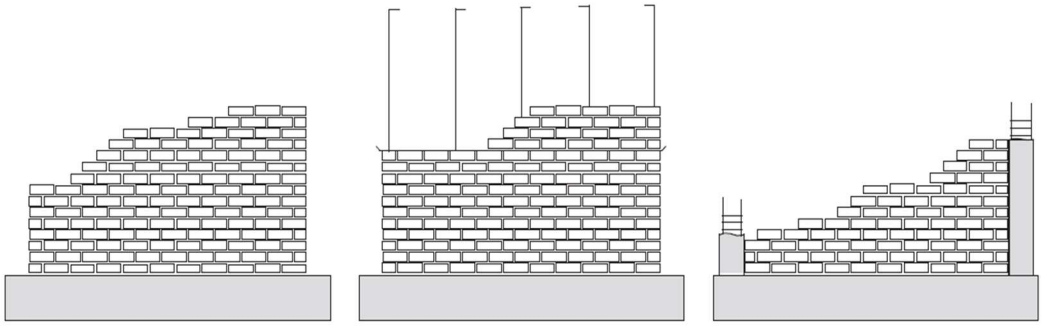

Figure 2.1 Different types of masonry constructions: (a) URM; (b) reinforced masonry; (c) confined masonry (Barazza, 2012)

Special attention should be given to calcium silicate elements (CS elements) masonry, since the work of the thesis is focusing on the structural behavior of a calcium silicate masonry assemblage.

The CS elements (Figure 2.2) consist of a mixture of 92% sand, 8% lime and water. Their properties are determined by the chemical reaction between the sand and lime mixture and the pressure applied during the moulding procedure (Vermeltfoort, 2008).

Due to their smooth and level surfaces, resulting from their specific moulding and hardening process, the CS elements allow for the use of thin mortar layers with a thickness between 2 and 3 mm.

CS elements are produced in three-unit sizes: brick, block and element and the term “element” is used to differentiate their size from the traditional brick or block sizes. A calcium silicate element has a length between 900 and 1000 mm, a height between 520 and 650 mm, a thickness between 100 to 300 mm and weighs 10 to 40 times more than the regular unit (Ng andu, Martens, & Vermeltfoort, 2006).

These elements are commonly used for the internal wythe of cavity walls, while clay bricks are often used for the external wythe. The interior side of the inner leaf of the walls is usually finished with plaster. The exterior side is finished with insulation. (Schipper, Ham, & Ravenshorst, 2017)

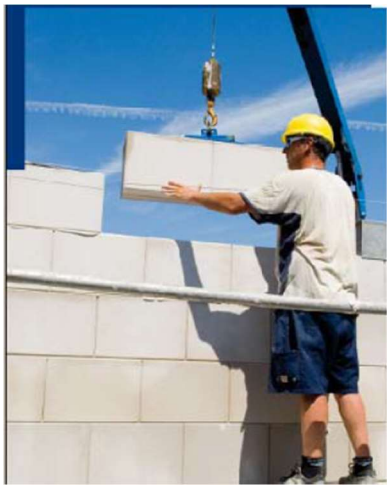

Figure 2.2 Building with CASIEL (Vermeltfoort, 2008)

2.2 Material behavior

Mechanical properties of masonry can be obtained from standard material tests. When masonry constituents are tested individually, their interaction is neglected, which can lead to inaccurate approximations. In the following section, material properties and behavior of masonry are detailed.

2.2.1 Unit behavior

Compressive behavior of masonry units

The structural behavior of masonry units is not homogeneous and isotropic. The compressive strength of masonry units is usually determined by performing a compression test, after which the stress-strain curve of the unit can be obtained (Barazza, 2012). Experimental results found in literature (Kaushik, Rai, & Jain, 2007) showed that the brick units behaved linearly up to 30% of the peak load. Further on in the loading process, the behavior of brick units became highly nonlinear (Figure 2.3).

The compressive part of the stress-strain diagram is used for the determination of the modulus of elasticity of clay brick units. Some reports (Kaushik et al., 2007) recommend for the elasticity module E_b a value of: $150 \cdot f_b \leq E_b \leq 500 \cdot f_b$, while others (Barazza, 2012) recommends a value of $E_b = 355 \cdot f_b$ for calcium silicate bricks.

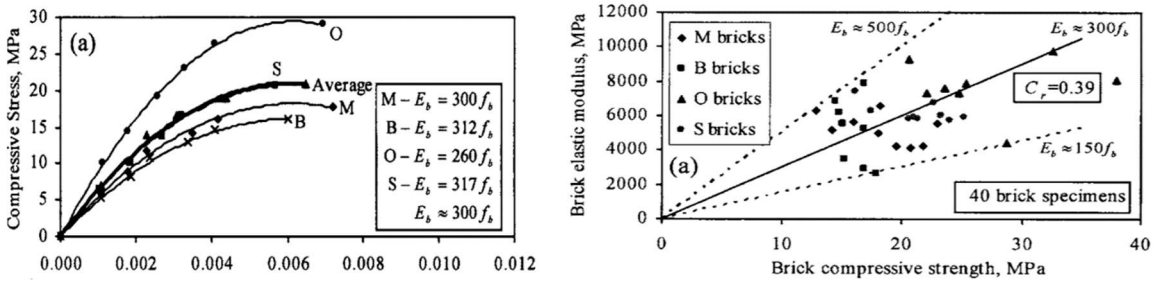

(a) (b)

Figure 2.3 Compressive stress-strain curve (a) and variation of modulus of elasticity (b) for brick units (Kaushik et al., 2007)

The material of masonry units has a quasi-brittle behavior and when units are subjected to compression, the fracture behavior can be described by the following stages: micro-cracks initiation, crack interaction, crack propagation and macrocracks growth (Figure 2.4):

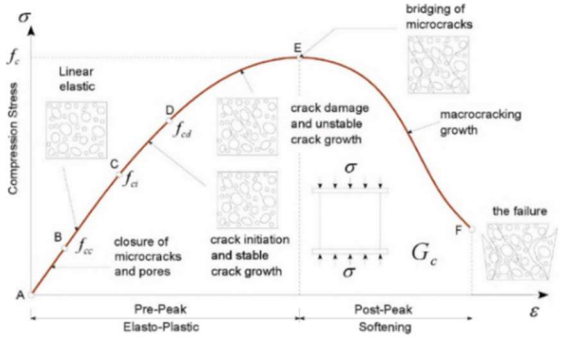

Figure 2.4 Typical behavior of quasi-brittle materials under axial compression (Bakeer, 2009)

The compression strength of CS elements is also determined from compression tests on cubes and prisms. The compressive properties of CS elements were determined experimentally by Vermeltfoort (Vermeltfoort, 2008) and the results are summarized in the Figure 2.5:

Code	$f'_{d,EL}$	f'_{wall}	E-modulus	
CS 12	16	8.4	6250	
CS 20	20	10.2	9500	
CS 28	28	13.6	12000	values according
CS 36	36	16.8	14000	to NEN 6790

Figure 2.5 *Compressive properties of CS elements and CS element masonry (N/mm²) (Vermeltfoort, 2008)*

Tensile behavior of masonry units

The tensile behavior of masonry units can be outlined by performing a series of tests such as: "uniaxial tensile strength test", "flexural tensile strength test" or "splitting tensile strength test" (Barazza, 2012).

The tensile failure of masonry units is characterized by the formation and propagation of micro cracks. This behavior of the masonry can be described by two different stages of the material during loading (Bakeer, 2009):

1. Pre-peak stage: An elasto-plastic process characterized by the development of stable micro cracks when the load increases. The peak strength f_t is reached at the end of this stage.

2. Post-peak stage: This stage is characterized by the softening behavior at the fracture zone. The micro cracks develop into macro cracks and because of the increase in distance between the two margins of the cracks, the stress begins to gradually decrease towards the zero value. The stress-displacement relation represents the softening diagram and its being characterized by the tensile strength f_t and the fracture energy G_f^I. Fracture energy is defined as the area under the softening diagram.

These stages can be visualized in Figure 2.6:

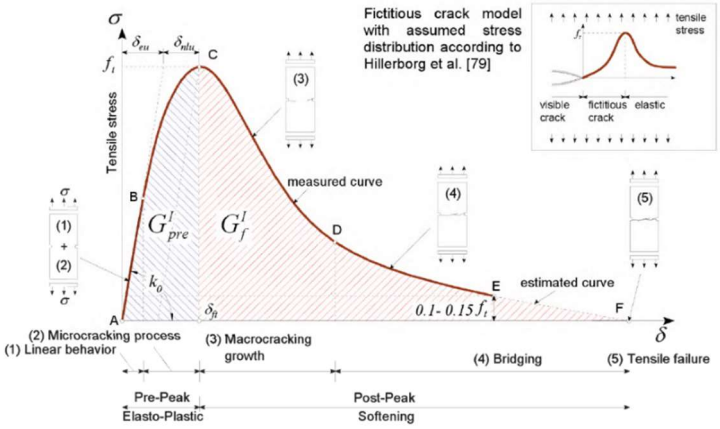

Figure 2.6 Typical behavior of quasi-brittle materials under axial tension (Bakeer, 2009)

According to Vermeltfoort (Vermeltfoort, 2008), the tensile strength of CASIELs elements is determined through splitting and bending tests performed on specimens of different sizes and has a value of approximately 2N/mm^2.

Biaxial behavior of units

Biaxial behavior of units becomes relevant in case of special types of units, such as units with perforations. However, these kinds of experiments are not developed in literature and thus the biaxial behavior of masonry units is not very well understood (Roca, González, Oñate, & Lourenço, 1998).

2.2.2 Mortar Behavior

Usually, there are different types of mortar that can be used in masonry constructions: general purpose mortar, thin layer mortar and lightweight mortar. The general purpose mortar is traditionally used in joints with a thickness larger than 3mm, the thin layer mortar can be used for joints with a thickness that varies between 1 and 3mm, while the lightweight mortar is designed to fulfill specific requirements of masonry (Barazza, 2012).

The mortar behavior can also be obtained through a series of tests. The most relevant one is represented by the simple compression test that can provide the strain curve of the mortar and the characteristic compression strength (Figure 2.7). The compression strength of the mortar depends on the proportion of the constituents and especially on the water-cement ratio (Kaushik et al., 2007). The tensile strength of the mortar can be determined by other types of tests such as: "uniaxial tensile strength test", "flexural tensile strength test", "splitting tensile strength test" (Barazza, 2012).

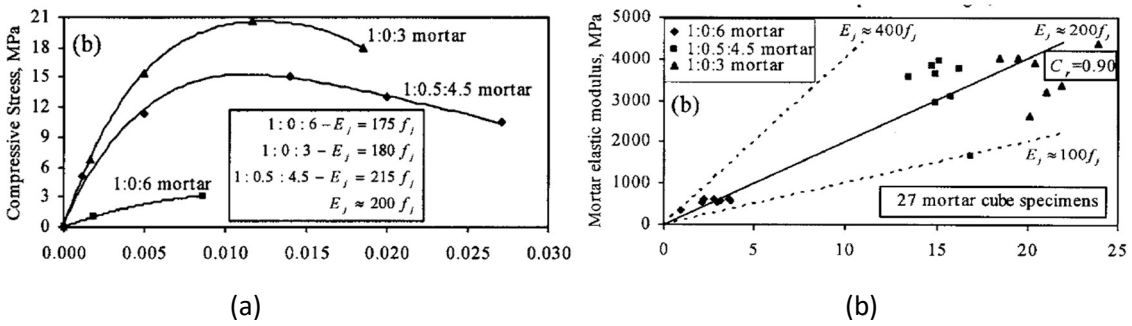

Figure 2.7 Compressive stress-strain curve (left) and variation of modulus of elasticity (right) for mortar (Kaushik et al., 2007)

2.2.3 Unit-mortar interface behavior

The interface between units and mortar is often the weakest link in the masonry assemblage and thus cracking is usually concentrated in this area. There are two types of failure that can occur in this interface: tensile failure (mode I) and shear failure (mode II) (P. B. Lourenço, 1996). Both failure modes can be described through a series of tests (Figure 2.8).

For the mode I failure, the softening curve obtained indicates a fracture energy varying from 0.005 to 0.02 Nmm/mm^2. The fracture energy G_f^I represents the amount of energy needed for the development of a unitary area of crack along the unit-mortar interface. The experimental results that

describe the mode II failure yield an exponential shear softening diagram with a residual dry friction level. The fracture energy G_f^{II} is defined by the area between the stress-displacement diagram and the residual dry friction level and has a value that varies between 0.01 to 0.25 Nmm/mm^2 (P. B. Lourenço, 1996; Roca et al., 1998).

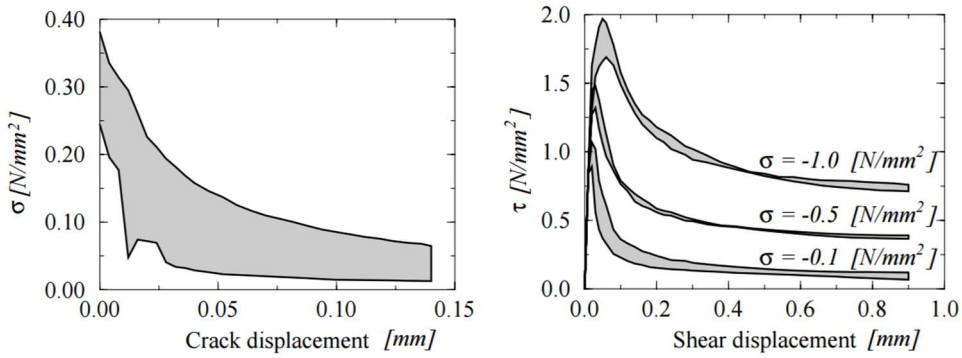

(a) (b)

Figure 2.8 Stress displacement diagram: (a) tensile bond behavior of masonry; (b) Shear bond behavior of the joints; (P. B. Lourenço, 1996)

The shear strength of thin layer joints was determined by Vermeltfoort (Vermeltfoort, 2008) through a series of tests performed on calcium silicate blocks with different levels of pre-compression (Figure 2.9). The results showed an initial shear strength of 0.58N/mm^2, with a friction coefficient of 0.56 in the pre-cracked phase and 0.47 in the post-cracked phase.

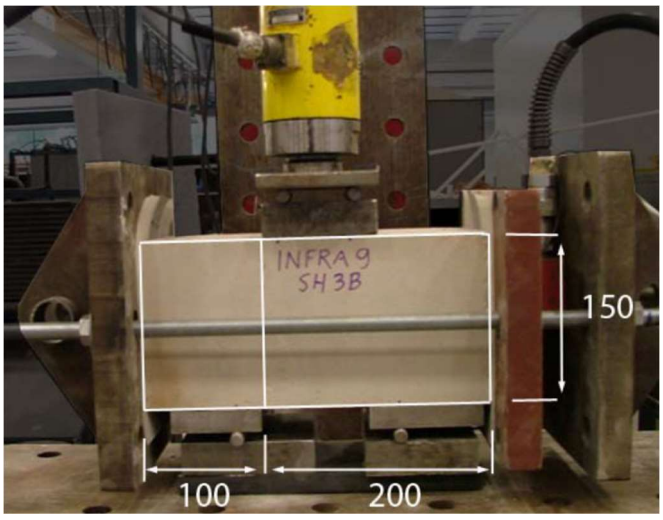

Figure 2.9 Shear test set up (Vermeltfoort, 2008)

2.2.4 Composite behavior

The behavior of the masonry as a composite can be determined through a series experimental tests on masonry specimens: compression test for Rilem specimen or diagonal tests on masonry walls (Barazza, 2012).

Compressive behavior

The mechanical properties of masonry are mostly determined from compression tests. The uniaxial compressive strength of masonry in the direction normal to the bed joints is obtained from the RILEM test, which implies a rather large and costly specimen. (Barazza, 2012; Roca et al., 1998).

According to EN 1996-1-1:2005, the characteristic compressive strength of calcium silicate masonry walls with a thin layer mortar can be determined with the following formula:

$$f_k = K \cdot f_b^{0.85} \tag{2.1}$$

where K equals 0.8 for calcium silicate masonry units.

As stated by Vermeltfoort (Vermeltfoort, 2008), tests performed by Vermeltfoort and Ng'andu on calcium silicate element walls showed that the averaged strength was 13.9N/mm^2, while the Young's modulus had a value of 10000N/mm^2. The thin layer mortar, with a thickness of 2-3 mm, did not have any significant influence on the deformation of the joint.

Tensile behavior

Failure of the masonry in tension is usually generated by the failure of the joints. When tensile loading is perpendicular to the bed joints the failure is usually related to the low tensile bond between the units and the bonds. If the masonry contains low tensile strength units, then the failure occurs when the tensile strength of the unit is exceeded. The overall tensile strength of the masonry can be approximated to the lowest value between the tensile strength of the unit and the tensile bond strength between unit and joints. The failure modes associated with the tensile loading can be divided into two types: zigzag cracks to head and bed joints (Figure 2.10, a) and vertical cracks through the units and head joints, as it can be seen in Figure 2.10, b. (P. B. Lourenço, 1996; Roca et al., 1998).

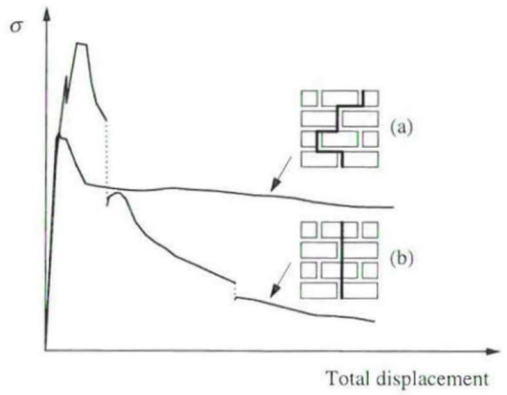

Figure 2.10 Types of failure under tensile loading (Roca et al., 1998)

Biaxial behavior

The uniaxial tests are not capable to fully describe the behavior of masonry. For a complete description on the masonry behavior, the biaxial strength envelope needs to be determined from a full stress vector in a fixed set of material axes or a combination between the principal stresses and rotation angle, as it can be observed in Figure 2.11 and Figure 2.12. (P Roca et al.)

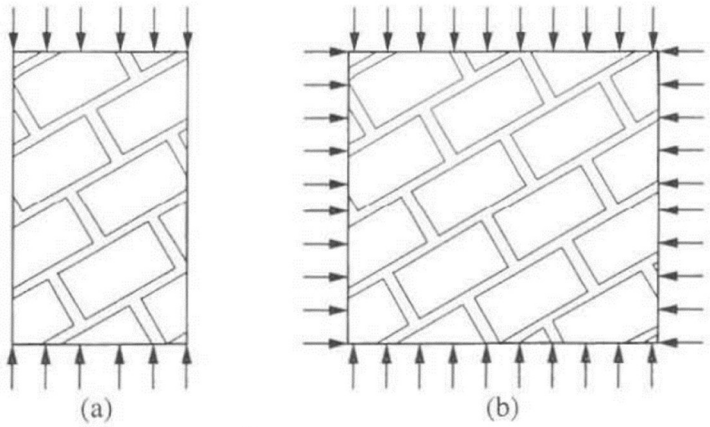

Figure 2.11 Possible test set-up for biaxial strength: (a) uniaxial loading oriented at a given angle; (b) biaxial loading at a given angle with respect to the bed joints; (Roca et al., 1998)

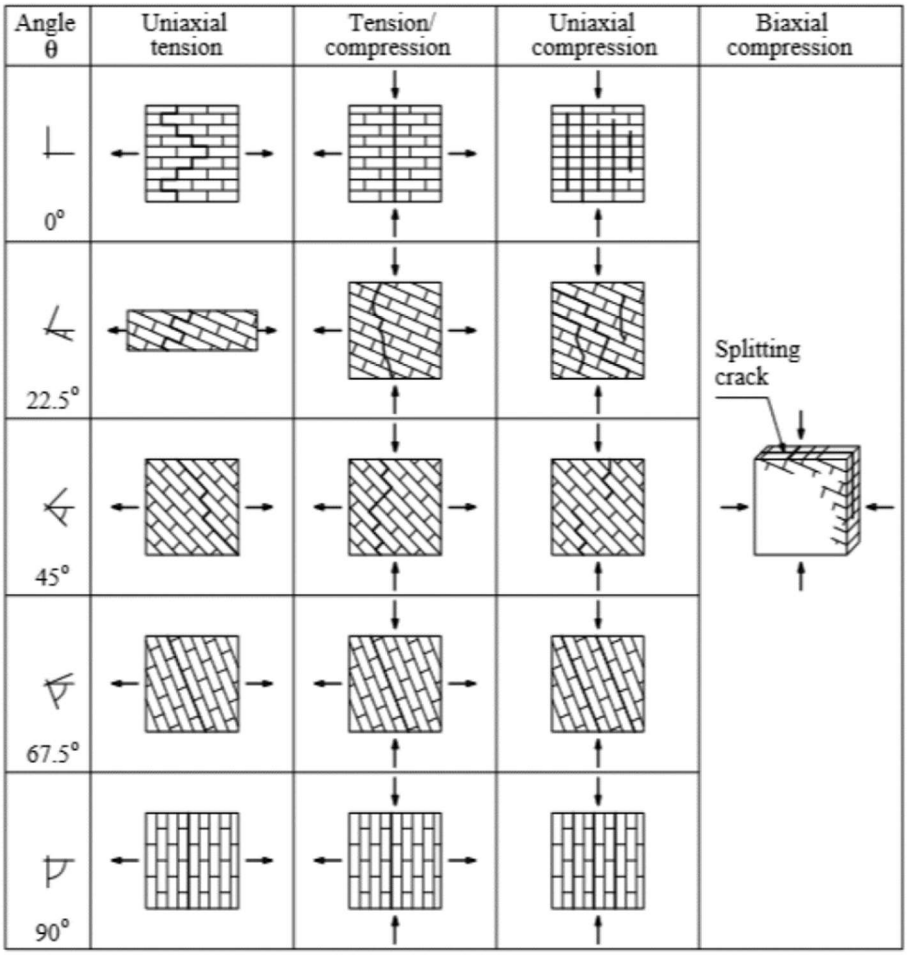

Figure 2.12 Modes of failure of solid clay units under biaxial loading (P. B. Lourenço, 1996)

2.3 Possible failure mechanisms of masonry walls

The typical failure modes for masonry include: in-plane failure and out-of-plane failure of masonry walls, combined in-plane and out-of-plane failures, anchorage failure or failure due to the lack of anchorage between walls and diaphragms. Of these failure mechanisms, the in-plane failure of URM walls seems to be the most common failure mode, while the out-of-plane failure of masonry walls represents the most serious safety hazard (Yi, 2004).

2.3.1 In-plane failure mechanisms

The in-plane behavior of masonry structures depends on the geometry and dimension of the structural walls, as well as on the mechanical properties of the masonry and boundary conditions. When examining the in-plane behavior of masonry walls, three general types of failure can be determined (Tomaževič, 2009; Yi, 2004):

a) Shear failure, characterized by the formation of diagonal cracks when the tensile strength of masonry is smaller than the tensile stresses due to external forces (Figure 2.13, a).

b) Sliding failure, characterized by the wall sliding off the horizontal mortar bed when the shear force in the pier exceeds the shear strength of bed joints (Figure 2.13, b).

c) Rocking failure, characterized by the appearance of wide flexural cracks in the corner of the masonry wall due to large flexural moments in masonry. During rocking failure, another failure mode can be identified: toe crushing. Toe crushing is a brittle failure mode that occurs when the compressive strength of the masonry is exceeded by the compressive stresses in the masonry due to external loads (Figure 2.13, c).

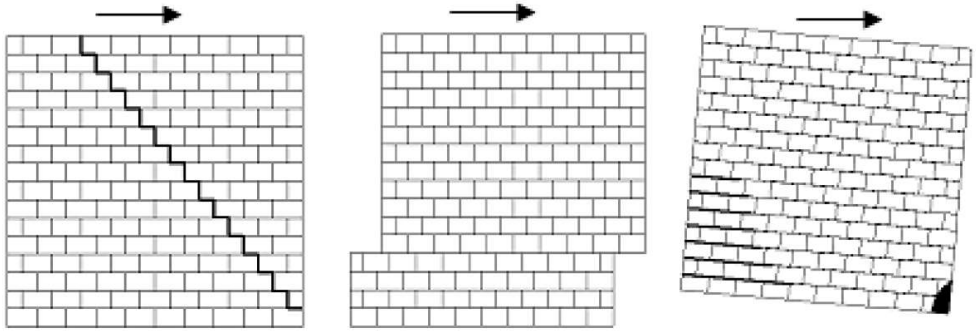

Figure 2.13 In plane failure mechanisms of unreinforced masonry walls (Farshchi, Motavalli, Schumacher, & Marefat, 2009)

2.3.2 Out-of-plane failure mechanisms

The out of plane failure of masonry elements represents a common type of failure of masonry structures subjected to seismic loading and occurs when the connections between walls or between walls and floors do not provide sufficient restrain. The overall out-of-plane behavior of unreinforced masonry structures is highly dependable on the out of plane failure of piers. The out-of-plane failure of piers, which depends substantially on the boundary conditions of the piers, can prevent the structure from reaching its full capacity (Tondelli & Beyer, 2014).

Several out-of-plane failure mechanisms are presented in Figure 2.14:

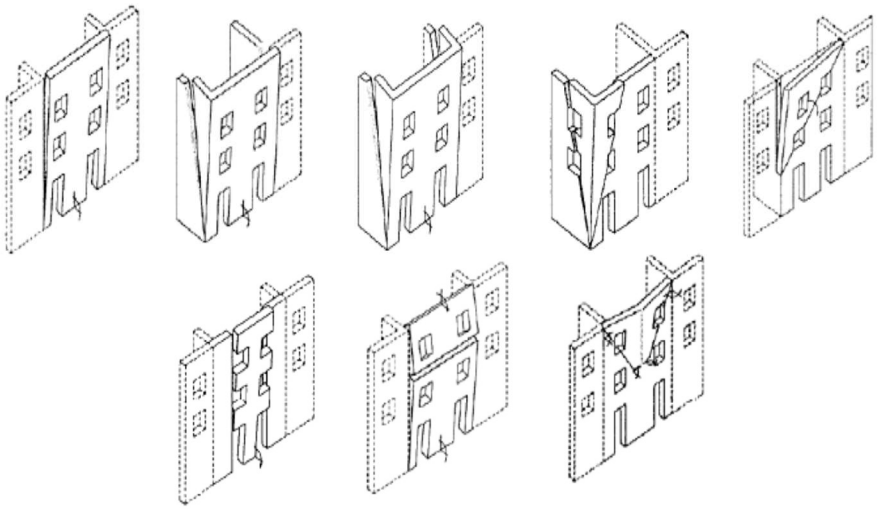

Figure 2.14 Out of plane failure mechanisms (Calvi et al., 2006)

2.4 Flange effect

A flange is considered the portion of the transversal wall that participates with the in-plane wall to resists lateral loads and has an influence on the failure mode of the in-plane loaded wall (Moon, Yi, Leon, & Kahn, 2006).

Existing simplified predictive techniques are not considering the influence of transversal walls on the failure modes of the in-plane loaded walls, and thus cannot lead to accurate results. Experimental findings show that the failure mode can change from rocking for a wall with no flanges to shear cracking for walls with flanges (Russell & Ingham, 2008), while other tests show that the position of the flanges has a great influence on the behavior of the wall. The lateral strength of the flanged wall is usually greater than the lateral strength of the wall with no flanges (Russell & Ingham, 2010). As reported by the same tests, a drift of θ_u=0.4% is considered as an acceptable limit for walls failing in shear.

According to the recommendations provided by the NZSEE guidelines (NZSEE, 2016), the length of the transversal wall that participates in the flange effect equals six times the width of the piers.

3 Modelling of masonry structures

The existing literature reveals distinct strategies to model masonry structures. The main approaches based on Finite Element Modelling (FEM) are represented by the micro and macro modeling, each of this method being characterized by different features. The main differences between these two modelling approaches refer to the level of applicability and the computational costs required. Another approach for masonry modelling is represented by the simplified equivalent frame model, which differentiates from the previous ones by a sensible reduction in computational costs. This work is focused on the equivalent frame modelling strategy and a more detailed description of this modelling approach is given is Chapter 3.2.

3.1 Modelling approaches overview

Different strategies are proposed in literature for the modelling of masonry structures. The main difference between these modelling approaches refer to the way the masonry is described and the scale and level of applicability of the analysis. The main modelling approaches are described below:

- *Micro-modelling approach*, in which each masonry component is modelled separately.
- *Macro modelling approach*, in which the entire structure is modelled as a continuum.
- *Equivalent Frame (EF) modelling approach*, in which the walls are considered as an idealized frame and are subdivided into a set of masonry panels that concentrate the nonlinear response.

Micro-modelling is one of the most accurate ways to model masonry, since the individual components of the masonry structure can be distinctly described. Using this approach allows for different failure mechanisms to be considered (Figure 3.1). These failure mechanisms can be split in joint mechanisms, unit mechanisms and combined mechanisms involving units and joints (P. Lourenço, Rots, & Blaauwendraad, 1995). Depending on the level of accuracy used in the modelling process, the micro-modelling can also be split in two approaches: detailed macro-modelling (Figure 3.2, b) and simplified micro-modelling. (Figure 3.2, c). The major drawback of this method is the demanding computational effort.

The macro-modelling approach is a very common and popular method, mainly because of the reduction in computational effort that it offers. Units, mortar and unit-mortar interface are smeared out in the continuum (Figure 3.2, d) and a relation between average stresses and strains of the masonry material is established (P. Lourenço et al., 1995; P. B. Lourenço, 1996). The anisotropic behavior masonry originates from the geometrical arrangement of individual units and mortar. However, because the macro-modelling approach considers the masonry constituents as smeared out in continuum, the description of the failure mechanism is not accurate enough and the prediction of the behavior might not be realistic.

The equivalent frame modelling approach seems particularly attractive since it can be easily applied in engineering practice and it allows a reduction in computational time and effort.

This simplified approach considers the masonry wall as an idealized frame, in which masonry panels are connected by rigid nodes. The structural walls are subdivided into piers, the main structural vertical elements, and spandrels, the main horizontal elements (Alessandro Galasco, Lagomarsino, & Penna, 2006). This discretization of the EF model is different than the discretization approach used in the micro or macro modelling approach and makes the EF model strategy very attractive because of the significant reduction in computational time. The computational time and effort is further reduced since in the EF modelling approach the walls are modelled as idealized plane frames and the nodes are considered as 2D nodes with only 3 degrees of freedom (S.T.A.DATA, n.d.-a).

Another significant difference between these modelling approaches refers to the definition of the non-linear response. In the EF model, the non-linear response of the structure is defined by the non-linear constitutive laws adopted for each masonry panel, while the non-linear behavior of a finite element model is related to the stiffness reduction that follows the material degradation and crack development in the loading process (Sionti, 2016).

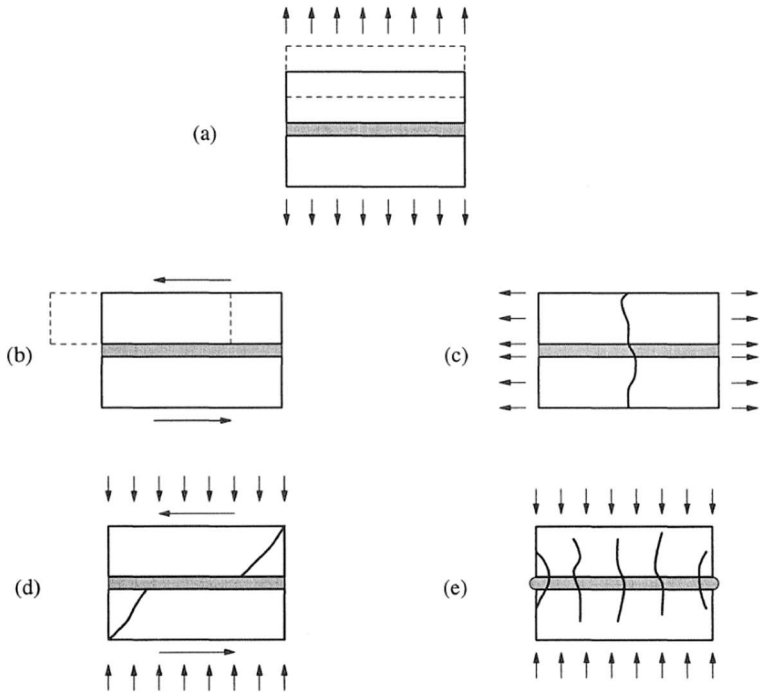

Figure 3.1 Masonry failure mechanisms: (a) Joint tension cracking; (b) joint slipping; (c) unit direct tension cracking; (d) unit diagonal tension cracking; (e) masonry crushing (P. Lourenço et al., 1995)

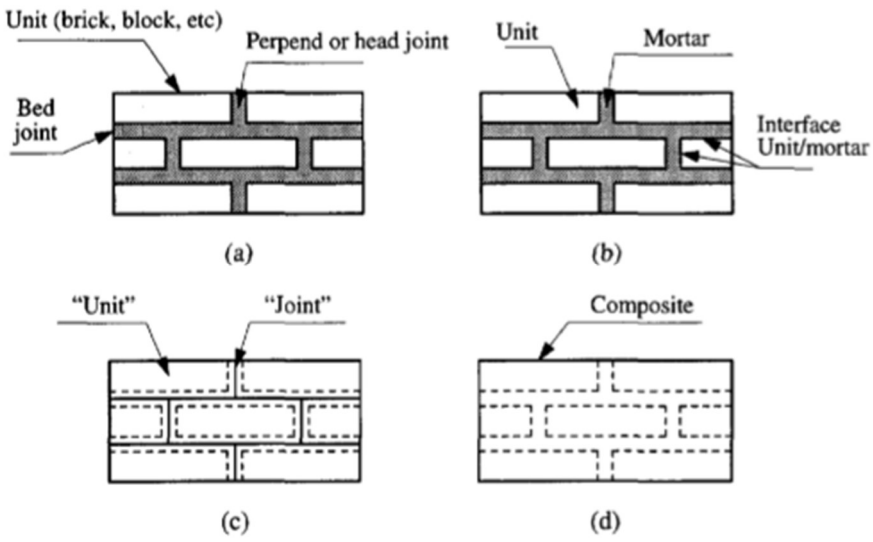

Figure 3.2 Modeling strategies for masonry structures: (a) masonry sample; (b) detailed micro-modeling; (c) simplified micro-modeling; (d) macro-modeling (P. B. Lourenço, 1996)

The micro and macro modelling are suitable for different types of structures. Micro-modelling applies to structural details and can give a better understanding of the local behavior of the structures, while macro-modelling applies to large structures composed of solid walls with large number of units and joints so that the stresses across the length will be almost uniform (P. B. Lourenço, 1996). The EF model approach is more suitable for larger structures, in which the walls can be idealized as a plane frame and the main structural elements can be easily identified. While the EF model offers a great reduction in computational time, the results are not as accurate as the ones provided by more complex models.

Nonetheless, the accuracy of each modelling approach requires a complete material description, which can be difficult to achieve since the properties of the masonry vary greatly accordingly to material properties, arrangement of units, joint thickness, size of the individual units or building technique. The necessary data should be obtained from laboratory tests performed on the individual constituents of masonry.

3.2 Equivalent frame modelling

This work is focused on the equivalent frame (EF) modelling approach. While the previous approaches are based on more complex finite element models, the equivalent frame model adopts a simplified method for the analysis of masonry structures. Because of the significant reduction in computational power, this method seems particularly attractive for engineering practice. The software 3Muri will be used for the analysis of the structure using the EF approach.

As a starting point, the EF model considers the masonry walls as an idealized frame. Each wall can be discretized into a set of masonry panels connected by rigid areas, represented by nodes. The masonry panels are considered as deformable elements, while the nodes are represented by the parts of the structure that are not usually subjected to damage during lateral loading. The nonlinear response of the structural elements is concentrated into the masonry panels. Adopting this modelling technique allows for the nonlinear analysis of complex unreinforced masonry structures with a reduced computational effort due to the limited required number of degrees of freedom (Alessandro Galasco, Lagomarsino, Penna, & Resemini, 2004; Lagomarsino, Penna, Galasco, & Cattari, 2013).

The steps followed in the analysis of the structural model are illustrated in Figure 3.3:

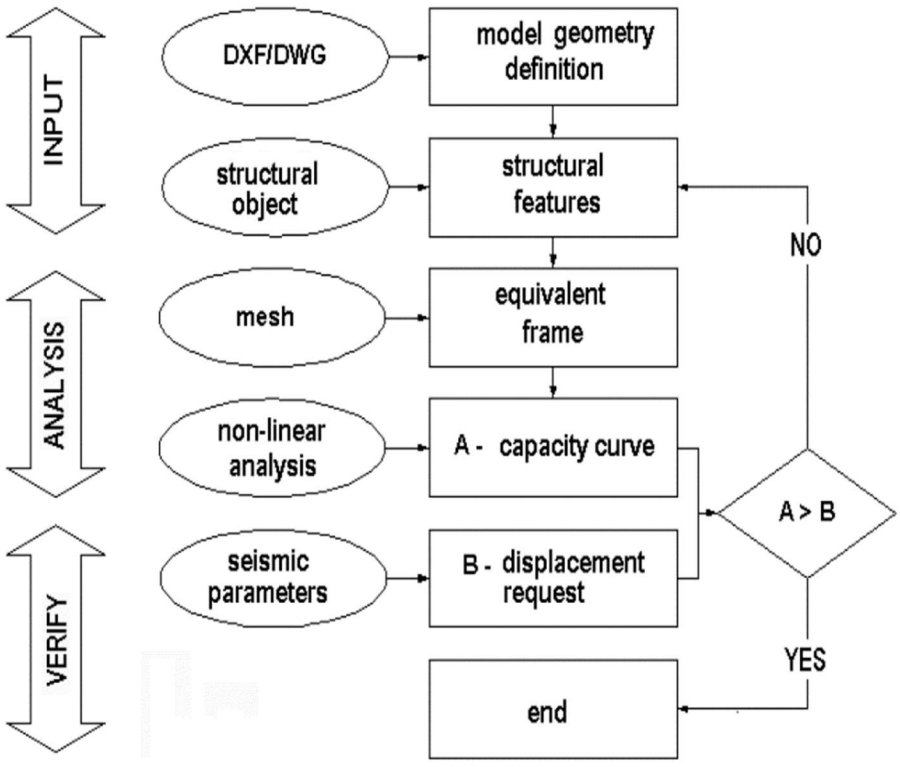

Figure 3.3 Process to follow in the verification of the structure (S.T.A.DATA, n.d.-b)

For the development of an appropriate model the following points should be considered:

- *Geometry:* The first step in the input phase is the definition of the model geometry. This includes the placement of the walls (structural objects) in the plan, as well as the dimension of the walls and the height of the floors.

- *Material properties:* The structural objects in the model are defined by their material and other geometric parameters (inertial characteristics, resistance properties). The resistance properties mainly refer to the compressive and shear strength.

- *Discretization:* This step considers that the masonry walls are schematized by different structural elements: piers, spandrels and rigid nodes. This allows for the definition of the equivalent frame.

- *Loading:* In an EF model, the loads are only applied to nodes, in a monotonic way.

- *Nonlinear analysis:* The nonlinear analysis, which assumes that the increasing loads are applied in a monotonic mode, allows for the construction of the force-horizontal displacement curve that describes the behavior of the structure when subjected to horizontal loads. These loads are applied at a control node. The position of the control node is selected in such way that the failure of the structure can be described in a complete way. The evidence found in literature shows that positioning the control node on the weaker wall provides a comprehensive description of the failure mechanism, while positioning the control node on the stronger wall does not give a complete description of the collapse, since only the first failure step of analysis can be obtained (Alessandro Galasco et al., 2006).

- *Assessment:* The assessment of the structure is based on methodologies recommended by the Eurocodes. The displacements obtained are compared with the displacement required by the codes.

As mentioned before, the main advantage of this modelling approach refers the significant reduction in computational time due to simplified discretization approach. The definition of the idealized frame leads to a lower number of elements and degrees of freedom per elements, which in turn, reduces the time and effort necessary for the analysis.

Despite the advantages of adopting this modelling strategy, several drawbacks can be found. A wall can be idealized by a "strong spandrel-weak pier" model (SSWP) that assumes a perfect coupling between piers and coincides with a fixed boundary conditions of the piers or a "weak spandrel-strong pier" model (WSSP) that assumes no coupling between piers and corresponds to a cantilever idealization (Lagomarsino et al., 2013). However, these limit cases might not always be appropriate since walls can exhibit both types of behavior and thus special attention should be given when modelling the structural elements. Moreover, the bed joint sliding failure mode cannot be described by this simplified modelling approach and a micro-modelling approach must be used for the description of this type of failure. Since the equivalent frame model approach introduces strong simplifications, a compromise between the adopted hypotheses and the actual structural system has to be found.

An appropriate representation of the characteristics of each structural element is necessary to obtain a realistic prediction of the structural behavior.

In this thesis the analysis has been carried out with software 3Muri. An overview of the modelling strategy and its applicability is presented in the next section.

3.2.1 Modelling of in-plane walls and three-dimensional structures

As mentioned before, the structural walls are represented by an idealized frame, in which masonry panels are connected by rigid nodes. In this idealization, the walls are subdivided into piers, the main structural vertical elements, and spandrels, the horizontal elements that span between two vertical supports. These main structural elements are connected by rigid nodes. (Alessandro Galasco et al., 2006).

An accurate nonlinear response depends on the correct identification of the characteristics of the main structural components of the wall, such as geometry and boundary condition, but also on the modelling of the nonlinear response of the individual structural element. Figure 3.4 shows one way to determine the geometry and dimensions of the structural elements that can be further used for the idealization of the URM wall.

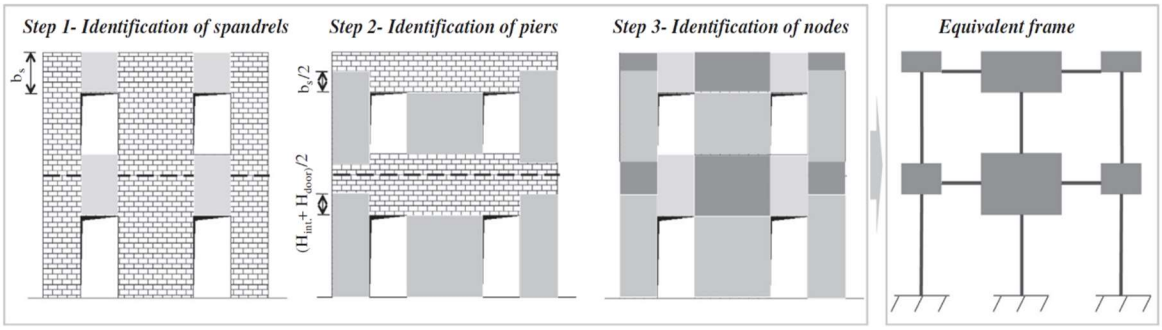

Figure 3.4 Equivalent frame idealization of a URM wall (Lagomarsino et al., 2013)

The main structural elements (piers and spandrels), represented in the model by the masonry panels, are modelled as 2-nodes elements. These deformable masonry panels, also named macro-elements (Brencich, Gambarotta, & Lagomarsino, 1998), allow the representation of the two main in-plane failure modes of masonry walls, the rocking mechanism and the shear-sliding mechanism, with a sensible reduction in the number of degrees of freedom (Brencich et al., 1998; Penna, 2005). With a macro-element defined by two nodes *i* and *j,* and with each node characterized by three degrees of freedom in the plane of the element (horizontal displacement *u, axial* displacement *w* and rotation *φ),* the kinematics of the masonry panels can be described by a vector of eight degrees of freedom (Figure 3.5). The axial displacement δ and the rotation θ represents the two degrees of freedom of the central zone (Alessandro Galasco et al., 2004). The influence of the axial load on the failure criteria of a single masonry panel is illustrated in Figure 3.6.

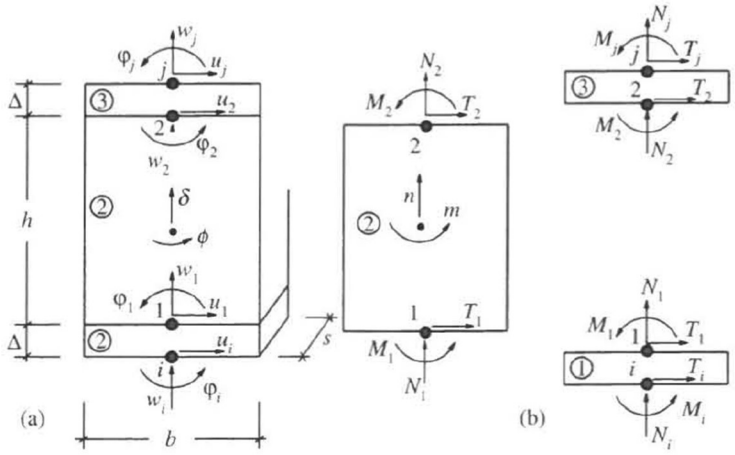

Figure 3.5 Kinematic variables of the non-linear macro-element (Penna, 2005)

The nonlinear beam element model implemented in 3Muri software assumes that the loads are only applied to the nodes and no loads act along the element (Lagomarsino et al., 2013). This leads to an element described by six degrees of freedom, for which the elastic stiffness element matrix can be assembled:

$$\begin{Bmatrix} T_i \\ N_i \\ M_i \\ T_j \\ N_j \\ M_j \end{Bmatrix} = \begin{bmatrix} \frac{12EJ}{h^3(1+\psi)} & 0 & -\frac{6EJ}{h^2(1+\psi)} & -\frac{12EJ}{h^3(1+\psi)} & 0 & -\frac{6EJ}{h^2(1+\psi)} \\ 0 & \frac{EA}{h} & 0 & 0 & -\frac{EA}{h} & 0 \\ -\frac{6EJ}{h^2(1+\psi)} & 0 & \frac{EJ(4+\psi)}{h(1+\psi)} & \frac{6EJ}{h^2(1+\psi)} & 0 & \frac{EJ(2-\psi)}{h(1+\psi)} \\ -\frac{12EJ}{h^3(1+\psi)} & 0 & \frac{6EJ}{h^2(1+\psi)} & \frac{12EJ}{h^3(1+\psi)} & 0 & \frac{6EJ}{h^2(1+\psi)} \\ 0 & -\frac{EA}{h} & 0 & 0 & \frac{EA}{h} & 0 \\ -\frac{6EJ}{h^2(1+\psi)} & 0 & \frac{EJ(2-\psi)}{h(1+\psi)} & \frac{6EJ}{h^2(1+\psi)} & 0 & \frac{EJ(4+\psi)}{h(1+\psi)} \end{bmatrix} \begin{Bmatrix} u_i \\ w_i \\ \phi_i \\ u_j \\ w_j \\ \phi_j \end{Bmatrix}$$

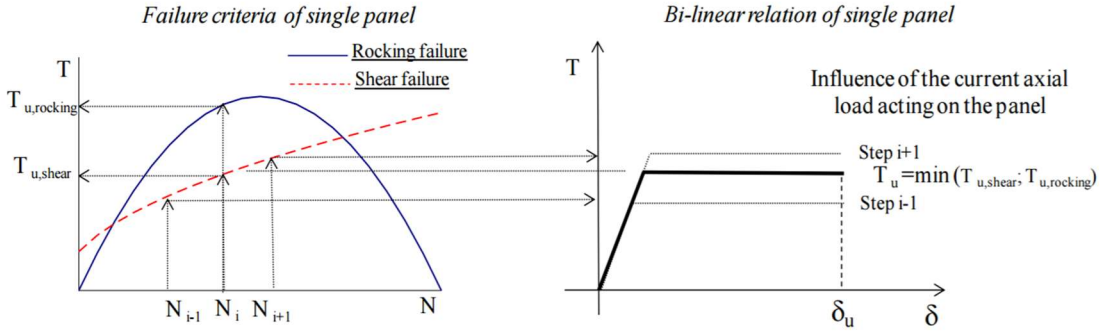

Figure 3.6 Influence of the axial load acting on the masonry panel (S.T.A.DATA, n.d.-a)

The procedures of the equivalent frame modelling of the in-plane loaded walls represents the starting point for the modelling of the global behavior of the three-dimensional structures. An accurate structural behavior can be obtained only if a proper connection between the vertical and horizontal elements is considered. Thus, the three-dimensional structure resumes to the strategy of assembling the masonry walls and to the modelling of diaphragms (Lagomarsino et al., 2013).

3.2.2 Assembling of masonry walls

The three-dimensional assembling of the masonry walls starts from the definition of a global Cartesian coordinate system (X, Y, Z), in which the planar walls can be modelled as idealized planar frames in the local coordinate system (Lagomarsino et al., 2013). In this way, the internal nodes that belong to a single wall are still characterized by 3 degrees of freedom, while the connecting nodes, that belong to more than one wall have 5 degrees of freedom in the global coordinate system (Figure 3.7). Because of the membrane behavior between the walls and floors, the rotation around the vertical axis Z can be neglected (Alessandro Galasco et al., 2006).

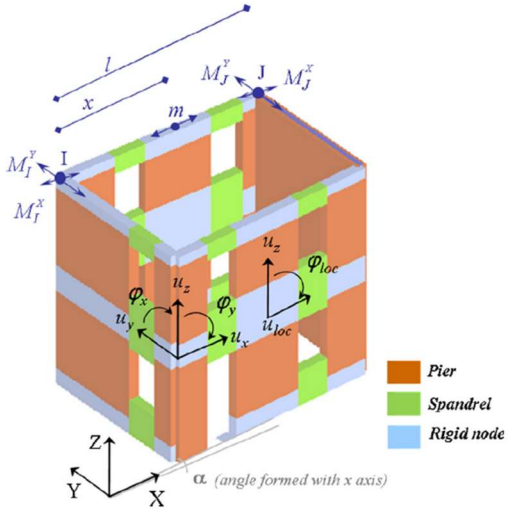

Figure 3.7 3D assembling of masonry walls (Lagomarsino et al., 2013)

3.2.3 Modelling of floors

The overall structural behavior of the building depends on the stiffness of the diaphragms. Floor diaphragms can be modelled in 3Muri as orthotropic membrane with 3 or 4 node elements and two displacement degrees of freedom per each node: u_x, u_y (Lagomarsino et al., 2013). The floors are characterized by one warping direction with Young modulus E_1, by Young modulus E_2, with a direction perpendicular to the warping, by the Poisson coefficient ν and by the elasticity tangential module $G_{2,1}$. The modules E_1 and E_2 represents the stiffness of the floor in two directions, while the $G_{2,1}$ represents the shear rigidity of the floor (S.T.A.DATA, n.d.-a).

3.2.4 Benchmarks

This part of the literature study presents an overview of other studies on URM structures using an EF modelling approach. These studies were chosen because their structural characteristics are similar with the characteristics of the URM structure studied in this report. The main objective is to show the capability of the EF approach, in general, and the capability of the 3Muri software, in particular. The limitations of this modelling approach are also illustrated. All the models have been validated by comparisons with experimental tests or accurate FEM models.

- *Pavia house (Magenes, Kingsley, & Calvi, 1995)*

The first model has been tested both experimentally and numerically. The experiment has been performed at the University of Pavia, Italy (Magenes et al., 1995). During the experiment, a full scale, two-storey URM building prototype was tested under quasi-static applied displacements at floor levels in such way that the distribution of lateral forces was proportional to the seismic weights. Four concentrated forces were applied to the longitudinal walls at floor levels to simulate the seismic forces (Figure 3.8).

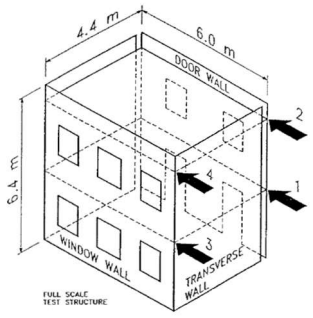

Figure 3.8 Pavia house building prototype (Magenes et al., 1995)

The analysis performed with the software 3Muri (A Galasco, Lagomarsino, Penna, & Cattari, 2002) aims to simulate the real testing conditions and shows a fair agreement with the experimental tests. The results are also in agreement with other numerical simulations (Figure 3.9), even though all the theoretical models provide an overestimation in strength (Rizzano & Sabatino, 2010).

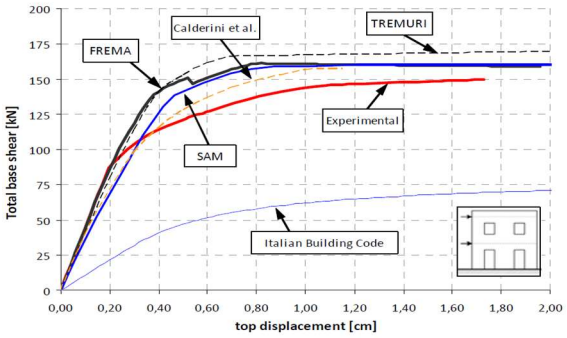

Figure 3.9 Capacity curves comparison for the Pavia house (Rizzano & Sabatino, 2010)

- *Typical masonry residential building (Ademović & Oliveira, 2012)*

The following example shows the capability of 3Muri software in terms of predicting the structural capacity by comparing the results of the analysis done with equivalent frame model (3Muri software) with the results of a finite element analysis (DIANA software).

The structure in this study is a typical masonry structure with 7 levels built in 1960s in Bosnia and Herzegovina. The load bearing walls are the transversal walls (walls in Y direction), while the longitudinal walls are not considered load-bearing due to their weakening by the many openings as shown in Figure 3.10, a.

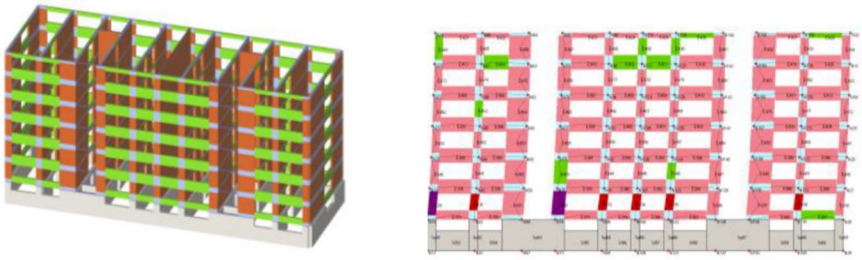

(a) (b)

Figure 3.10 EF model (a) and failure mechanism (b) (Ademović & Oliveira, 2012)

As it can be observed in Figure 3.11, the pushover curves in Y direction for the two modelling approaches are similar. The maximum load coefficient in 3Muri is only 7% higher than the load coefficient assumed by DIANA. The difference is easily explained by the fact that 3Muri assumes a rigid connection between spandrels and piers. The curve obtained from the equivalent frame model approach is also characterized by a horizontal plateau after the maximum strength is reached due to the elastic-ideal plastic constitutive curves of the structural elements.

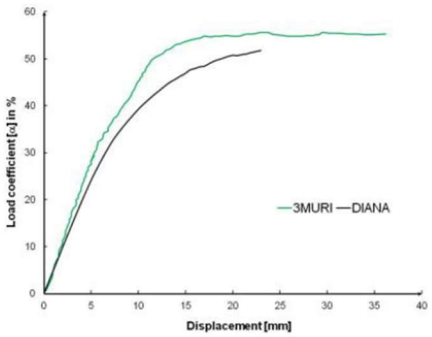

Figure 3.11 Capacity curve comparison (Ademović & Oliveira, 2012)

While DIANA offers a more detailed view of the crack propagation, with clear localization of the cracks and damage, 3Muri is able to show a global view of the damage and to identify the failure mechanism (Figure 3.10, b) with less computational time.

- *Two storey, seven-bay masonry wall in-plane loaded (Salonikios, Karakostas, Lekidis, & Anthoine, 2003)*

The next study illustrates the capability of the EF modelling approach in general, since the wall is analyzed using a different software. The wall is analyzed using an equivalent frame model in SAP 2000 and FREMA (Rizzano & Sabatino, 2010) and the results are validated against a discrete finite element analysis (Salonikios et al., 2003).

The comparison between the capacity curves shows a good agreement in terms of both stiffness and maximum lateral strength, proving once again that the equivalent frame model can provide an accurate response of the global behavior of the unreinforced masonry structures. The results of the analyses are illustrated in Figure 3.12:

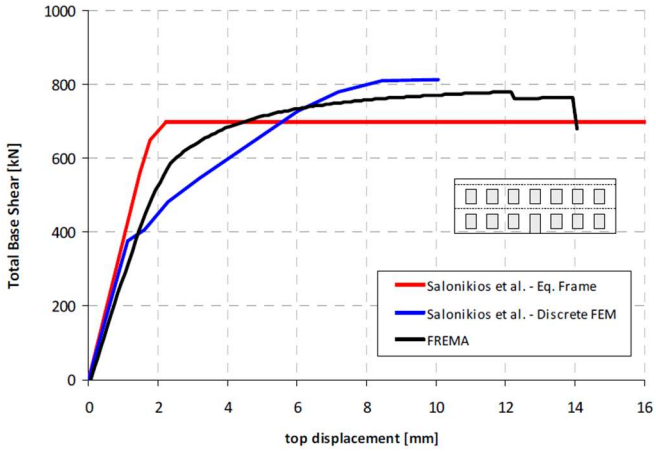

Figure 3.12 Capacity curve comparison of the seven-bay masonry wall (Rizzano & Sabatino, 2010)

The overestimation in strength observed in all the previous EF models can be explained by the rigid connections assumed by the software between the piers and spandrels. The accuracy of the results is closely related to the complexity of the model and even though there is a good correlation between the simplified models and the more complex finite element models, the EF model still has some limitations. A finite element model is able to provide a very detailed crack pattern with a localization of the damage and cracks in the structure. On the other hand, the EF modelling approach is only able to provide a global view of the damage and the main failure mode. However, the computational time required for the EF model is considerably reduced.

All the previous examples show that 3Muri can provide reliable results when compared with the experimental outcome or the results obtained from more accurate finite element analyses. These findings, together with the reduced computational effort make 3Muri a valid tool for the assessment of the structural behavior of unreinforced masonry structures.

4 Modelling of seismic behavior

4.1 Modelling approaches for seismic actions

Earthquakes can be defined as sudden slips on fault that result in ground shaking movements and radiated seismic energy and are caused by abrupt changes in the stress state of the earth (USGS, 2017).

According to Chopra (2012), the seismic action on a two-story structure can be modelled by a damped two degree of freedom system, for which the equation of motion can be described in the following way:

$$m\ddot{u} + c\dot{u} + \hat{k}u = -mu_g\ddot{(t)} \tag{4.1}$$

$$-mu_g\ddot{(t)} = P_{eff(t)} \tag{4.2}$$

Where:

m mass matrix

c damping matrix

$\hat{k}$ stiffness matrix

u floor displacement matrix

$u_g(t)$ horizontal earthquake motion

$P_{eff(t)}$ effective earthquake force

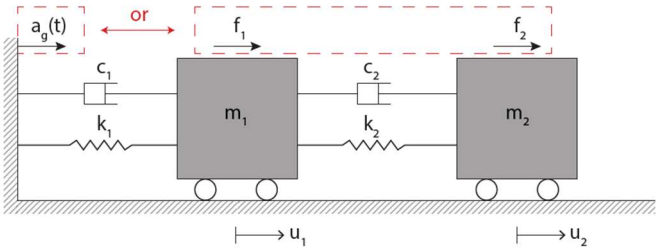

Figure 4.1 Damped two degree of freedom system (van der Mersch, 2015)

There are different methods identified in literature that can be used for the modelling of seismic actions (EN1998-1, 2004; Gupta, 1992; Kilar & Fajfar, 1997) and the main categories are summarized as follows:

- *Equivalent lateral force method*: a static analysis in which the seismic force is distributed to every floor; the generated force is concentrated at the center of mass of each floor;
- *Pushover analysis*: a simplified non-linear static analysis, in which the structure is subjected to monotonically increasing lateral loading;
- *Response spectrum analysis*: a linear dynamic analysis, in which the horizontal seismic action is represented by two orthogonal independent components, represented by the same spectrum;
- *Non-linear time history analysis*: a more complex dynamic analysis in which the seismic action is represented by ground accelerograms;

The work of this thesis focuses on the pushover analysis, since this method is applied in the research.

4.2 Pushover analysis

In a pushover analysis, the intensity of lateral loads is increased continuously until an ultimate condition is attained. The analysis monitors the horizontal forces recorded and provides information regarding the cracking pattern, plastic hinges development, yielding and value of the load for which the damage of structural elements can be observed (Themelis, 2008). The method gives a good understanding on the behavior of the structure in terms of deformations and cracking.

Eurocode 8 (EN1998-1, 2004), which defines the pushover analysis as a "non-linear static analysis under constant gravity loads and monotonically increasing lateral loads", requires that the lateral loads should be applied at the center of masses of the model, in at least two different vertical distribution. The main vertical distribution of the lateral forces are represented by the "uniform" pattern, that considers the lateral forces proportional to the story masses, and a "modal" pattern (EN1998-3, 2005).

Following a pushover analysis, the pushover curve can be determined by plotting the displacements versus the base shear force (Figure 4.2).

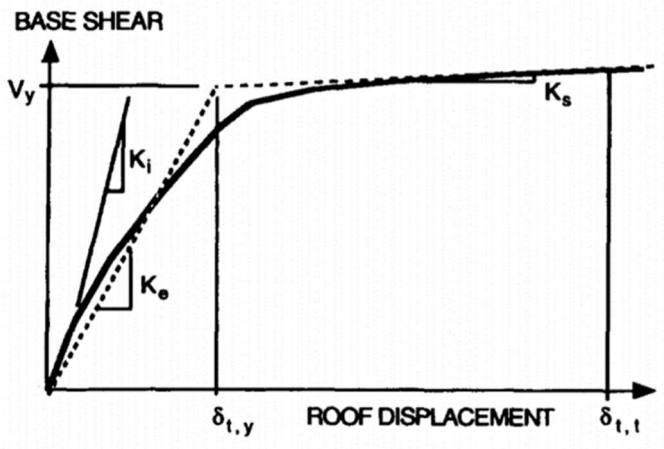

Figure 4.2 Static base shear vs roof displacement of a multi degree-of-freedom system (Krawinkler & Seneviratna, 1998)

The monotonic pushover analysis is not capable to account for the reduction in stiffness and strength of the structure created by the cumulative damage from the cyclic load, and thus a cyclic pushover analysis has to be adopted (Panyakapo, 2014). The cyclic pushover analysis (Figure 4.3) consists of a sequence of successive pushover analysis in which each pushover analysis is pushing the structure in the opposite direction of the previous load case and each load case uses the stiffness at the end of the previous load case. The cyclic pushover curve obtained provides information on the seismic behavior of masonry walls in terms of strength degradation, stiffness deterioration and energy dissipation capacity.

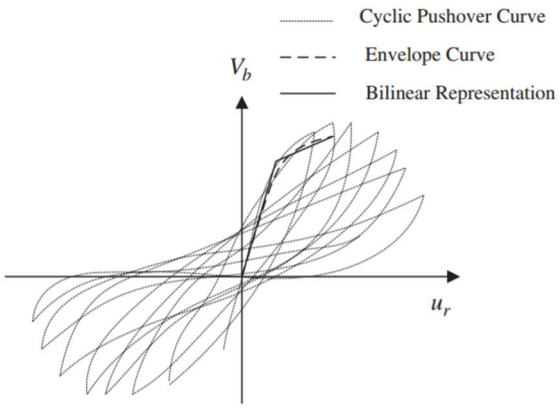

Figure 4.3 Cyclic pushover and envelope curve (Panyakapo, 2014)

When compared to an elastic static or dynamic analysis, it can be observed that a pushover analysis can also provide additional information on other characteristics of a structural system (Krawinkler & Seneviratna, 1998). These additional characteristics include:

- Identification of the critical regions where the deformations are expected to exceed the required limits.
- Identification of strength discontinuities in the structure that are likely to affect the dynamic behavior of the structural system.
- The effect of strength deterioration of individual structural elements on the global behavior of the structure.
- Confirmation of the accuracy of load paths in the structure, after considering all the structural elements, as well as the connection between the elements the influence of the stiff non-structural elements.

The pushover analysis considers that a single mode controls the structural response of a building and that the response of a structure can be described by the response of an equivalent single degree of freedom system. However, literature studies show that while this analysis can provide an accurate global structural response for the structures that vibrate mainly in the fundamental mode, the same accuracy is not valid for structures where higher mode effects become significant. For these types of structures, the pushover analysis should be combined with other evaluation methods (Krawinkler & Seneviratna, 1998).

4.3 Assessment of seismic behavior

The criteria used for the assessment of the global behavior of masonry structures are related to the monitoring of the global and local failure. The structural failure can be assessed by referring to the ductility of the structure, drift limits or the capacity of individual structural elements.

4.3.1 Ductility

Ductility represents one of the most important parameters used in the assessment of the seismic performance of a building and refers to " the ability of a structure to sustain its load-carrying capacity and dissipate energy when it is subjected to cyclic inelastic displacements during an earthquake" (NZSEE, 2015).
The ductility factor can be determined based on the following formula proposed by the Eurocode 8 (EN1998-3, 2005):

$$\mu = \frac{d \cdot m}{d \cdot y} \tag{4.3}$$

Where:

$d \cdot m$ displacement at the formation of the plastic mechanism
$d \cdot y$ yield displacement of the idealized SDOF system

Since the pushover analysis only evaluates the capacity of the building, the assessment of the structure is performed according to the Eurocode guidelines. The capacity of the structure is compared in a seismic check with the "demand" requested by the seismic event defined by the user: ultimate displacement capacity of the structure (d_u) is compared against the target displacement (d_t) (S.T.A.DATA, n.d.-a).

4.3.2 Drift limits

Failure is associated with the exceedance of the drift limit defined for the governing failure mechanism. Different values for drift limits can be found in international standards. For masonry structures, Eurocode 8 (EN1998-3, 2005) refers to element storey drifts and proposes the following formulas depending on the type of failure and the specific limit state:

For significant damage:

Bending: $0.008 \cdot H_0 / D$ (4.4)

Shear: $0.004 \cdot H_0 / D$ (4.5)

Near collapse:

Bending: $4/3 \cdot 0.008 \cdot H_0 / D = 0.0107 \cdot H_0 / D$ (4.6)

Shear: $4/3 \cdot 0.004 \cdot H_0 / D = 0.0053 \cdot H_0 / D$ (4.7)

4.3.3 Analytical approaches for estimating the capacity of URM walls

Different analytical approaches for estimating the capacity of URM walls are included in international standards (NZSEE 2006, EN 1998-3:2005).

As it was mentioned before, the main in-plane failure modes of masonry walls include the shear failure and the rocking (flexural) failure mode. Magenes & Calvi (1997) describe the typical force-displacement curve for diagonal shear and flexural failure mode. The shear response curve is initially characterized by a low strength and stiffness degradation. After the post-peak phase is achieved, the curve is characterized by a higher energy dissipation and quick stiffness degradation. The curve corresponding to the flexural response is identified by low energy dissipation, together with large displacement and no significant loss in strength.

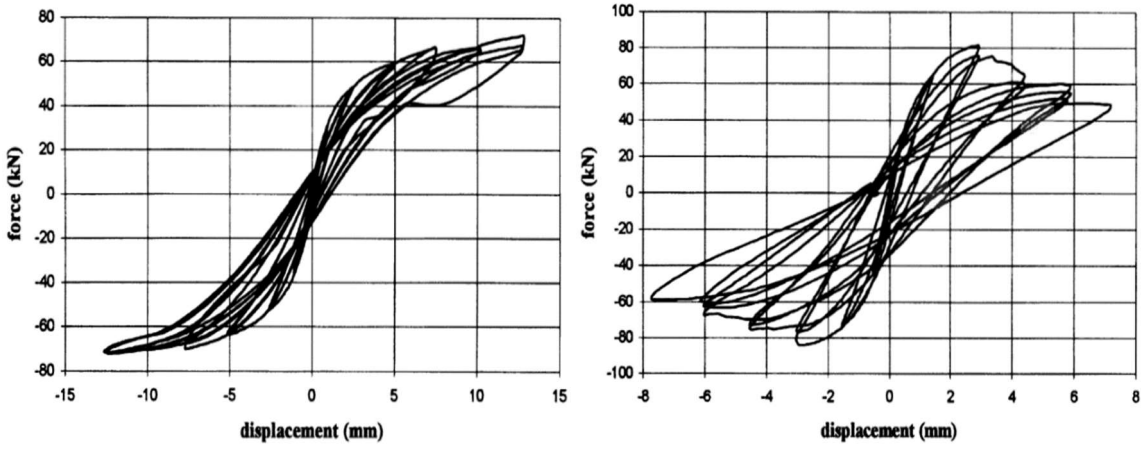

(a) (b)

Figure 4.4 Experimental behavior of double clamped piers: flexural response (a) and diagonal shear cracking (b) (Magenes & Calvi, 1997)

The strength associated with the main failure modes of in-plane loaded masonry piers (rocking failure, shear failure and sliding failure) can also be described by simplified formulations. These expressions, that will be presented in the following section, only include the most relevant parameters for the response of the piers and thus they are characterized by a reduced level of accuracy (Magenes & Calvi, 1997).

Rocking failure

The maximum shear that can be withstood by a pier subjected to rocking failure mode can be determined if the tensile strength in the joints is neglected and if a proper stress distribution is considered for the masonry pier in compression, as illustrated in Figure 4.5 (Magenes & Calvi, 1997):

$$V_t = \frac{D^2}{H_0} \cdot \frac{p}{2} \cdot \left(1 - \frac{p}{kf_u}\right) = \frac{Dt}{\alpha_v} \cdot \frac{p}{2} \cdot \left(1 - \frac{p}{kf_u}\right) \tag{4.8}$$

$$\alpha_v = \frac{M}{VD} = \frac{H_0}{D} = \frac{\psi' H}{D} \tag{4.9}$$

Where:

D	pier length
H_0	effective pier height
t	thickness
p=P/(Dt)	mean vertical stress on the pier due to axial load P
f_u	compressive strength of masonry
k=0.85	coefficient that considers the stress distribution at the compressed toe
α_v	shear ratio
ψ'	has a value of 1 when the pier is fixed at one end, and a value of 0.5 when the pier is fixed at both ends;

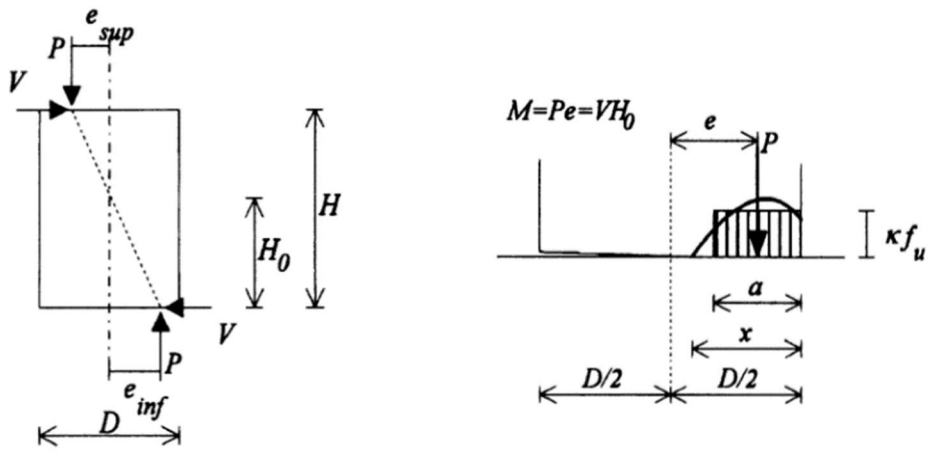

Figure 4.5 Assumptions for rocking strength evaluation (Magenes & Calvi, 1997)

NZSEE guidelines (NZSEE, 2015) propose a different formula for the calculation of rocking capacity:

$$V_r = 0.9 \cdot (\alpha \cdot P + 0.5 \cdot Pw) \cdot \frac{L_w}{h_{eff}} \tag{4.10}$$

Where:

V_r	strength of the pier based on rocking
α	factor equal to 0.5 for fixed-free cantilever and 1.0 for fixed-fixed wall pier
P	superimposed and dead load at the top of the pier
P_w	self-weight of the pier
L_w	length of the pier
h_{eff}	height to resultant of seismic forces

According to the same guidelines, the capacity of a rocking pier should be limited to the value that corresponds to a lateral drift of the pier of 0.011 or $0.003h_{eff}/L_{eff}$.

Shear failure

As mentioned before, the shear failure of unreinforced masonry piers depends on the mechanical properties of masonry units and mortar. Because of this, the description of the behavior using simplified formulations becomes more complicated. According to Magenes and Calvi (1997), there are two approaches used for the prediction of maximum shear strength associated with the shear failure mode.

The first approach considers that diagonal shear failure occurs when the principal stress in the center of the pier reaches a critical value:

$$V_d = \frac{f_{tu} Dt}{b} \sqrt{1 + \frac{p}{f_{tu}}} \tag{4.11}$$

where f_{tu} is the tensile strength of masonry and b accounts for the shear stress distribution at the center of the pier and depends on the pier aspect ratio H/D.

The second approach is based on a Mohr-Coulomb formulation and considers that diagonal cracking is associated with the failure of mortar joints. The ultimate shear force can be determined by the following formula:

$$V_d = Dt\tau_u = Dt(c + \mu p) = Dt\left(c + \mu \frac{P}{Dt}\right) \tag{4.12}$$

$$\tau_u = c + \mu\sigma_v \tag{4.13}$$

Where:

τ_u	the average ultimate stress in the horizontal section of the wall; and
σ_v	the main vertical stress in the pier.

The maximum diagonal tensile strength can also be calculated using the formula proposed by the NZSEE guidelines (NZSEE, 2015):

$$V_{dt} = f_{dt} A_n \beta \sqrt{1 + \frac{f_a}{f_{dt}}} \tag{4.14}$$

Where:

B	factor to correct nonlinear stress distribution
A_n	area of net mortared section of the pier
f_{dt}	masonry diagonal tension
f_a	axial compression stress due to gravity loads calculated at the base of the wall/pier

Section 6.2 of Eurocode 6 (EN1996-1-1, 2005) supplies general rules for designing unreinforced masonry structures subjected to shear loading. At the ultimate limit state, the following rule applies:

$$V_{Ed} \leq V_{Rd} \tag{4.15}$$

$$V_{Rd} = f_{vd} t l_c \tag{4.16}$$

Where:

V_{Ed}	design value of the shear load
V_{Rd}	design value of the shear resistance of the wall
f_{vd}	design value of the shear strength of masonry

t thickness of the wall resisting the shear loading

l_c length of the compressed part of the wall

The design value of the shear strength of masonry is based on the average of the vertical stresses over the compressed part of the wall subjected to shear loading and can be determined according to the following formula:

$$f_{vd} = \frac{f_{vk}}{\gamma_m} \tag{4.17}$$

Where:

f_{vk} characteristic value of the shear strength of masonry

Υ_m partial factor for materials

Sliding failure

The shear strength for a pier that is subjected to sliding failure can be determined by the following expression:

$$V_d = \mu P \tag{4.18}$$

Where μ is the sliding friction coefficient of the masonry joint and P is the axial load.

The maximum sliding shear strength proposed by the NZSEE (2015) is equal to:

$$V_s = 0.7 \cdot (t_{nom} L_w c + \mu_f (P + P_w) \tag{4.19}$$

Where:

μ_f masonry friction coefficient

P superimposed and dead load at the top of the pier

P_w self-weight of the pier

t_{nom} wall thickness

NZSEE (2015) further recommends that the bed joint sliding capacity of a rocking pier be limited to a lateral drift of 0.003. When drifts exceed this value, the lateral performance of a pier becomes unreliable.

5 TU Delft testing campaign on CS masonry walls and masonry assemblage

An accurate prediction of the behavior of structural components and the full-scale assembled unreinforced masonry structure can be obtained if the numerical models are validated and calibrated against experimental results.

The numerical models that make the subject of this thesis are constructed based on the quasi-static cyclic pushover tests performed at TU Delft on full-scale masonry walls and on full-scale masonry assemblage. Additionally, material test results are used to determine material parameters that are further used as input parameters for the equivalent frame models that make the subject of this thesis.

The test performed within the large-scale testing campaign at Delft University of Technology are summarized in Table 5.1.

Table 5.1: Overview of test performed at TU Delft (Damiola & Pagani, 2016; Esposito, Jafari, Ravenshorst, Schipper, & Rots, 2018; Esposito & Ravenshorst, 2017; Esposito, Schipper, & Ravenshorst, 2017; Esposito, Terwel, et al., 2017)

Specimen	Test performed
Calcium silicate brick masonry	Bending and compression test on mortar
	Compression tests on units
	Compression tests on masonry wallets
	Unit-mortar interface properties: triplet tests
	Unit-mortar interface properties: bond-wrench tests
Calcium silicate element masonry	Compression tests on masonry wallets
	Unit-mortar interface properties: couplets tests
Full scale masonry walls	In-plane test: Calcium silicate brick masonry wall
	In-plane test: Calcium silicate element masonry wall
Full scale masonry assemblage	Quasi-static cyclic pushover test

5.1 Material properties

The parameters that describe the masonry composite properties are determined through a series of tests on calcium silicate element specimens.

The following sections provide an overview of the results of the tests performed on calcium silicate element masonry walls at TU Delft until January 2017 (Damiola & Pagani, 2016; Jafari & Esposito, 2017). The tests consider the masonry constituents (CS elements and mortar) and masonry composite. These values are compared with the preliminary values, determined based on preliminary tests on masonry wallets. For the following analyses, the final values obtained in the tests are used. When experimental data is not available, the preliminary values are used instead.

Table 5.2: Overview of mechanical properties for calcium silicate element masonry

Symbol	Material properties	Units	Final Values (TU Delft)	Preliminary values
E_1	Elastic modulus of masonry in the direction perpendicular to bed joints evaluated at 1/3 of the maximum compressive stress	MPa	8557	9000 (1)*
E_2	Elastic modulus of masonry in the direction perpendicular to bed joints evaluated at 1/10 of the maximum compressive stress	MPa	9256	
E_3	Elastic modulus of masonry in the direction perpendicular to bed joints evaluated between 1/10 and 1/3 of the maximum compressive stress	MPa	8313	
G	CS Masonry shear modulus	MPa	3423	3600 (2)*
f'_m	CS Masonry Compressive strength	MPa	13.39	10-13 (1)*
f'_{el}	CS Element Compressive strength	MPa	19.45	18-21 (1)*
f_m	Compressive strength of mortar	MPa	15.66	10 (2)*
f_{mt}	Flexural strength of mortar	MPa	4.72	-
v	Poisson Ratio of masonry in the direction perpendicular to bed joints	-	0.17	0.17
E_c	Concrete C53/65 Young's modulus	MPa	38000	38000 (1)*
f'_{el-c}	Concrete C53/65 compressive strength	MPa	53	53 (1)
f_{vo}	Initial Joint shear strength	MPa	0.83	0.6-0.9 (1)*
μ	Masonry (bed joint) shear friction coefficient	-	1.49	0.43 (2)*
ρ	Density	KN/m^3	18.24	20

(1)* values obtained from preliminary tests (Schipper et al., 2017)

(2)* Eurocode recommendations

As already mentioned, the main purpose of the thesis is to understand and analyze the structural response of the calcium silicate element masonry walls and the calcium silicate element masonry assemblage. Since the analysis aims to simulate the test setup and the experimental results are further used in the report, special attention will be given to the tests performed on these elements. A detailed description of these tests is provided in the next sections.

5.2 In-plane tests on full-scale CS element masonry walls

Testing masonry components can provide valuable information on material properties and structural behavior. As a starting point for the assessment of the global behavior of the building, this research project focuses on the in-plane tests performed at TU Delft on full-scale masonry walls.

The in-plane tests discussed in this section refer to the quasi-static cyclic tests performed on two slender calcium silicate (CS) element masonry walls subjected to in-plane loading. The boundary conditions varied such that one wall was tested under double clamped configuration (TUD_COMP-24) and one wall was tested in cantilever configuration (TUD_COMP-25). The overall geometry of the walls and the boundary conditions are summarized in the following table:

Table 5.3: Overview of the in-plane tests (Esposito & Ravenshorst, 2017)

Test	Units type	L(mm)	H(mm)	t(mm)	Overburden (Mpa)	Boundary conditions
TUD_COMP-24	CS elements	979	2715	100	0.6	Fix-Fix
TUD_COMP-25	CS elements	979	2715	100	0.6	Cantilever

Material properties are determined through compressive, bending and bond-wrench tests performed on small specimens. These tests provide values for the mechanical parameters that can be further used in the numerical analysis.

Quasi-static cyclic tests performed on full-scale masonry walls also offer valuable information regarding the failure mode, shear strength and deformation capacity of the wall.

5.2.1 Double fixed wall (TUD-COMP-24)

This test illustrates the structural behavior of a double fixed calcium silicate element wall under in-plane lateral loading (Esposito & Ravenshorst, 2017).

The specimen tested showed a flexural failure mode. This failure mode is also suggested by the capacity curve, characterized by a symmetrical “S shape” with low energy dissipation and large drifts (Figure 5.1). The maximum attained shear force was 21.69KN in the positive loading direction and -21.45KN in the negative loading direction, while the drift had a value of 1.05% in positive direction and 1.17% in negative loading direction.

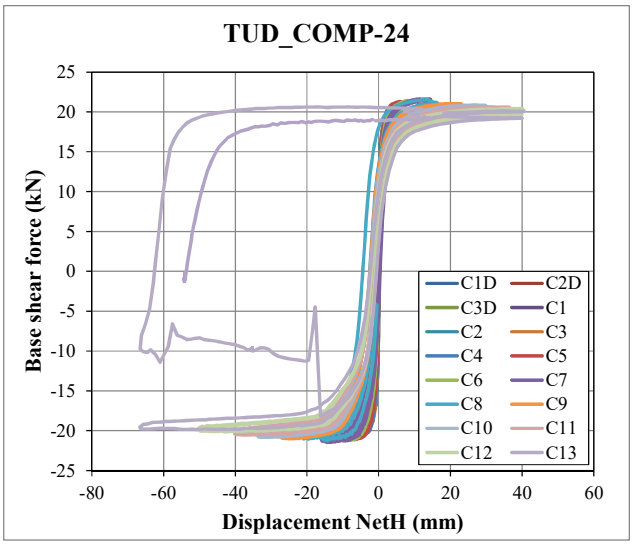

Figure 5.1 Capacity curve for TU-COMP-24 (Esposito & Ravenshorst, 2017)

The first cracks started developing in cycle 3 in both corners of the first bed joint and in the corner of the top bed joint. The cracks gradually increased their dimension, until rocking began, as it can be observed in Figure 5.2.

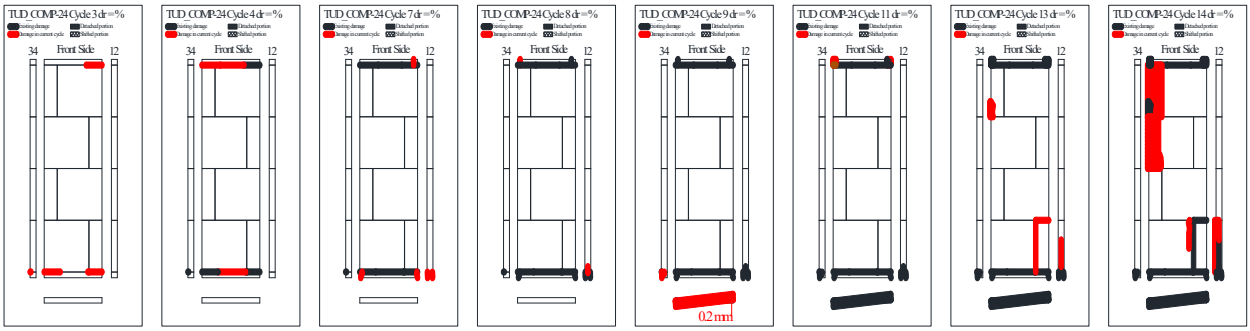

Figure 5.2 Crack evolution for TUD-COMP-24 (Esposito & Ravenshorst, 2017)

5.2.2 Cantilever wall (TUD-COMP-25)

This section focuses on the results obtained from the in-plane test performed on the cantilever calcium silicate element wall.

According to Esposito and Ravenshorst (Esposito & Ravenshorst, 2017), the experiment showed a pure rocking behavior for the calcium silicate element wall, with a maximum attained drift and shear force of 3.12% and 10.28KN, respectively, in the positive loading direction and a drift of 3.07% and total base shear force of -10.10KN in the negative direction (Figure 5.3).

The first cracks developed in both corners of the first bed joint, and gradually increased their dimension along the wall length until rocking began (Figure 5.4, Figure 5.5).

Additionally, the test showed that the initial stiffness of the masonry wall calculated accordingly to the linear elasticity theory was highly overestimated. The initial stiffness obtained from the performed test had a value of K_{in}=5.97KN/mm, compared to the predicted stiffness

$K_{in,\ pred}$=9.18KN/mm.

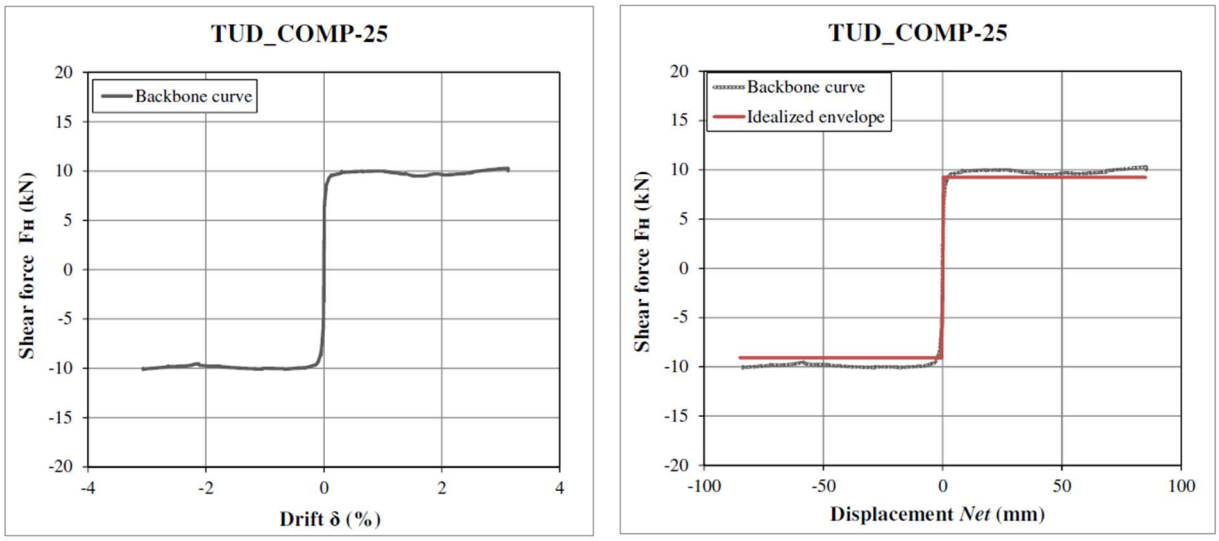

Figure 5.3 Force-drift curve: backbone curve (left) and idealized bilinear envelope (right); (Damiola & Pagani, 2016)

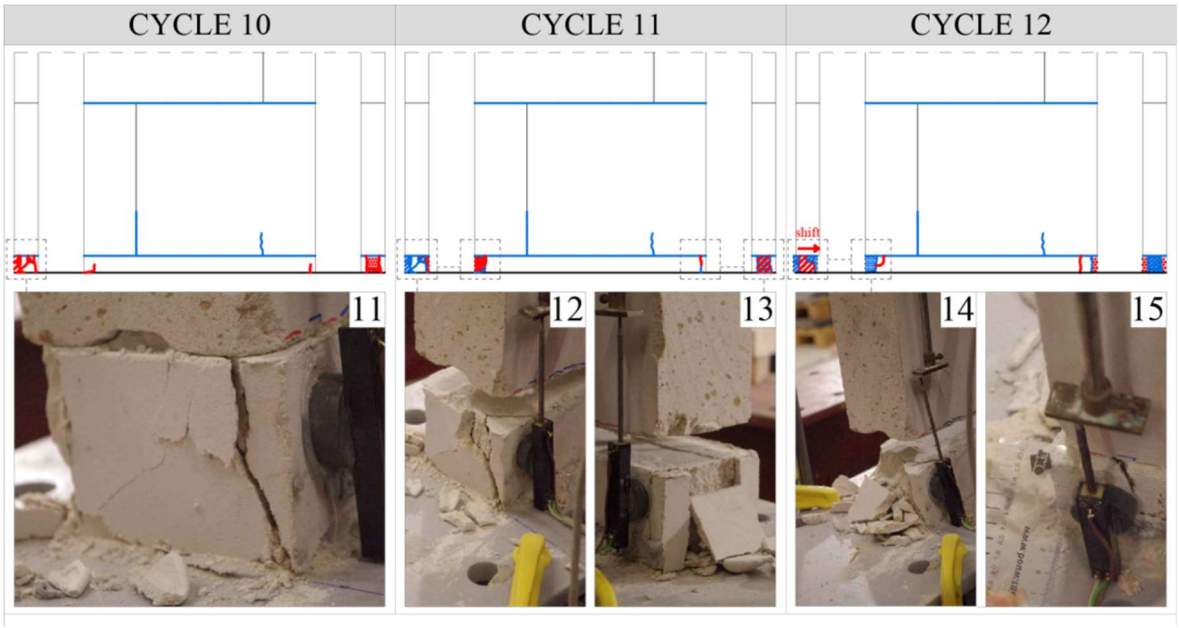

Figure 5.4 Crack evolution for TUD-COMP-25 (Damiola & Pagani, 2016)

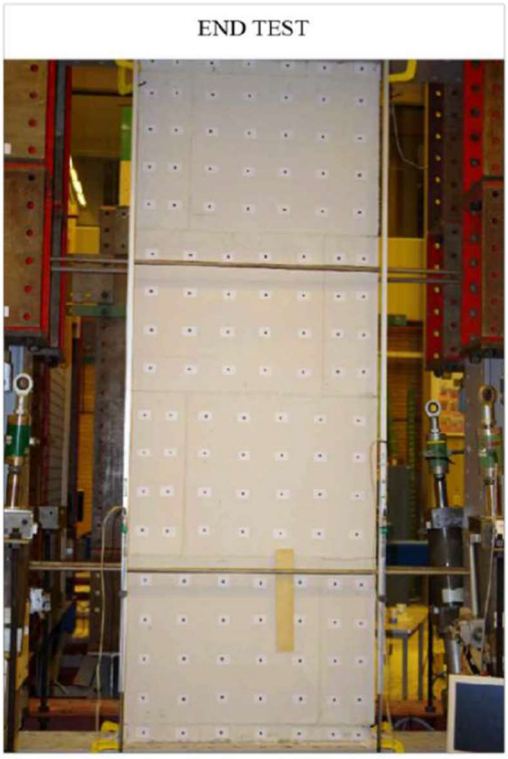

Figure 5.5 In-plane test on calcium silicate element masonry wall (Damiola & Pagani, 2016; Esposito & Ravenshorst, 2017)

5.3 Pushover test on full-scale CS element masonry assemblage (Esposito et al., 2018)

The selected case study for this test represents only the loadbearing parts of a typical Dutch house, that has been frequently built starting with 1980's. This type of construction is characterized by the presence of large daylight openings in the façades and loadbearing transversal walls that carry the floors. Calcium-silicate elements, as well as prefabricated concrete floors are used for the assembled structure. The long walls and piers are connected by metal ties. A kicker layer (in Dutch "kimlaag") is used as a layer under each wall in order to smoothen possible level differences in the building (Figure 5.6 and Figure 5.7).

The CS elements used for piers and transversal walls have the following dimensions: 897x643x100, while for the mortar joints, a 3mm bed and head joints with a "Silicafix lijmmortel" is used (Schipper et al., 2017).

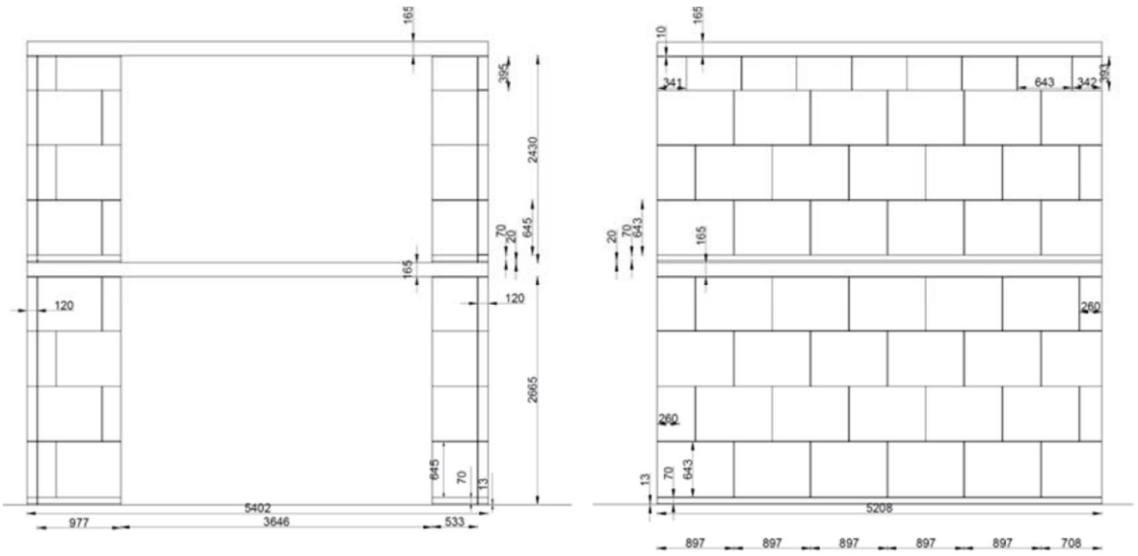

Figure 5.6 Side view of the overall geometry of the experiment (Schipper et al., 2017)

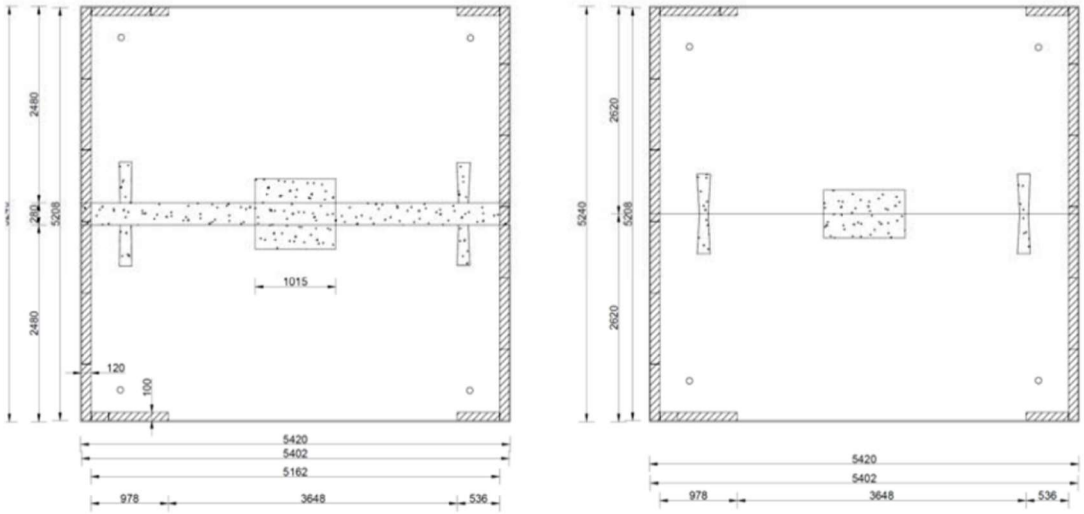

Figure 5.7 Top view of the overall geometry of the experiment (Schipper et al., 2017)

The loads are introduced into the structure by four horizontal actuators, two actuators located at the first floor (F3, F4) and two others located at the second floor (F1, F2), as it can be seen in Figure 5.8.

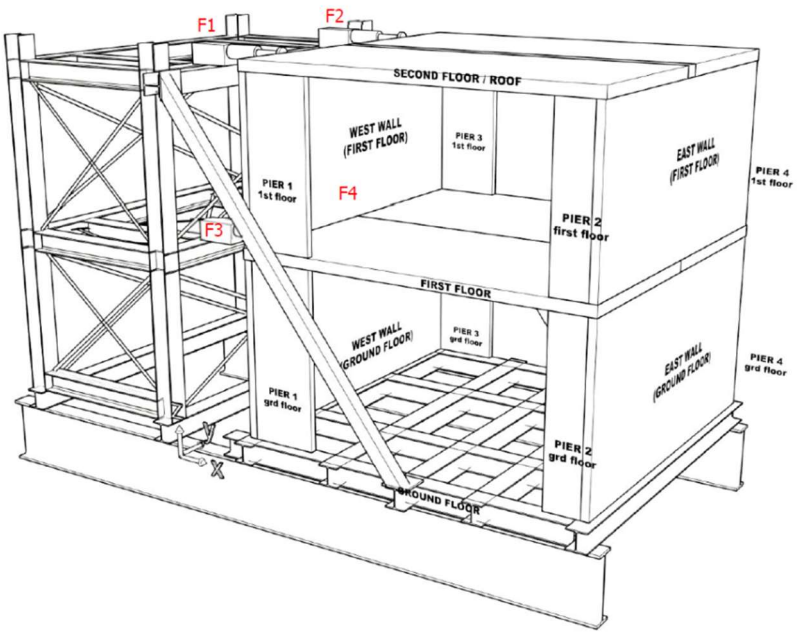

Figure 5.8 Test set-up (Schipper et al., 2017)

The global structural behavior of the calcium silicate masonry assemblage can be described and explained by evaluating the capacity curve (Figure 5.9) and the crack pattern evolution (Figure 5.10). The structure showed a maximum capacity of 65.7 KN in positive loading direction and a maximum capacity of 68.5 KN in negative loading direction. These values correspond to a displacement at the second floor of 14.9mm in positive direction and -8.6mm in negative direction (Esposito, Schipper, et al., 2017)

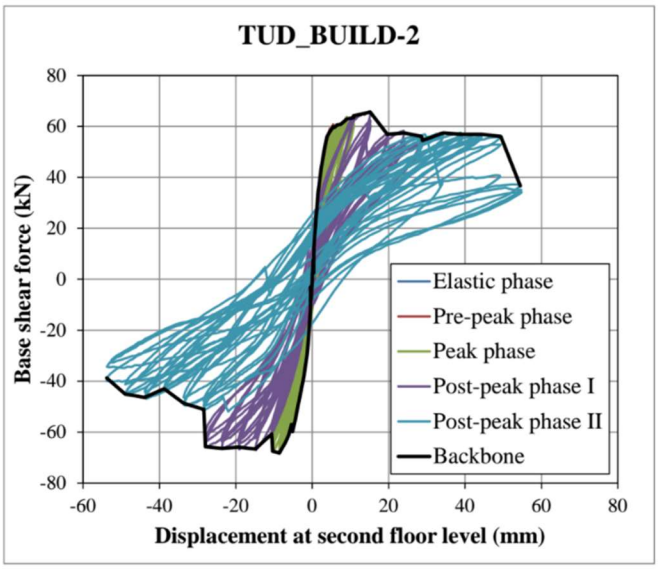

Figure 5.9 Capacity curve for the entire test (Esposito, Schipper, et al., 2017)

The first cracks started developing in the pre-peak phase at the floor and wall connections (Figure 5.10). These cracks gradually increased their dimension, while new cracks formed in both piers and transversal walls, following the pattern of the bed joints. Significant damage occurred in pier P3 in cycle 15 and in pier P1 in cycle 17b, while in cycle 19, out-of-plane deformation has been observed in the top part of pier P3. Extensive damage occurred until cycle 22, when pier P3 collapsed and pier P1 induced a rotation of the transversal wall (Figure 5.11).

The crack pattern evolution presented in Figure 5.10 is based on the visual inspection performed after each cycle of loading.

The maximum drift was attained at the first floor in cycle 22 and had a value of -1.8% in negative loading direction and +1.7% in positive loading direction. The first floor showed lower values of the drifts: -0.4% in C17 in negative loading direction and +0.8% in C22 in positive loading direction. (Esposito, Schipper, et al., 2017).

While the initial stiffness has been approximated to 27KN/mm, after the pre-peak phase and peak-phase a degradation of 27% and 57%, respectively, was recorded. The degradation corresponds to the formation of cracks and extensive damage in the piers (Esposito, Schipper, et al., 2017).

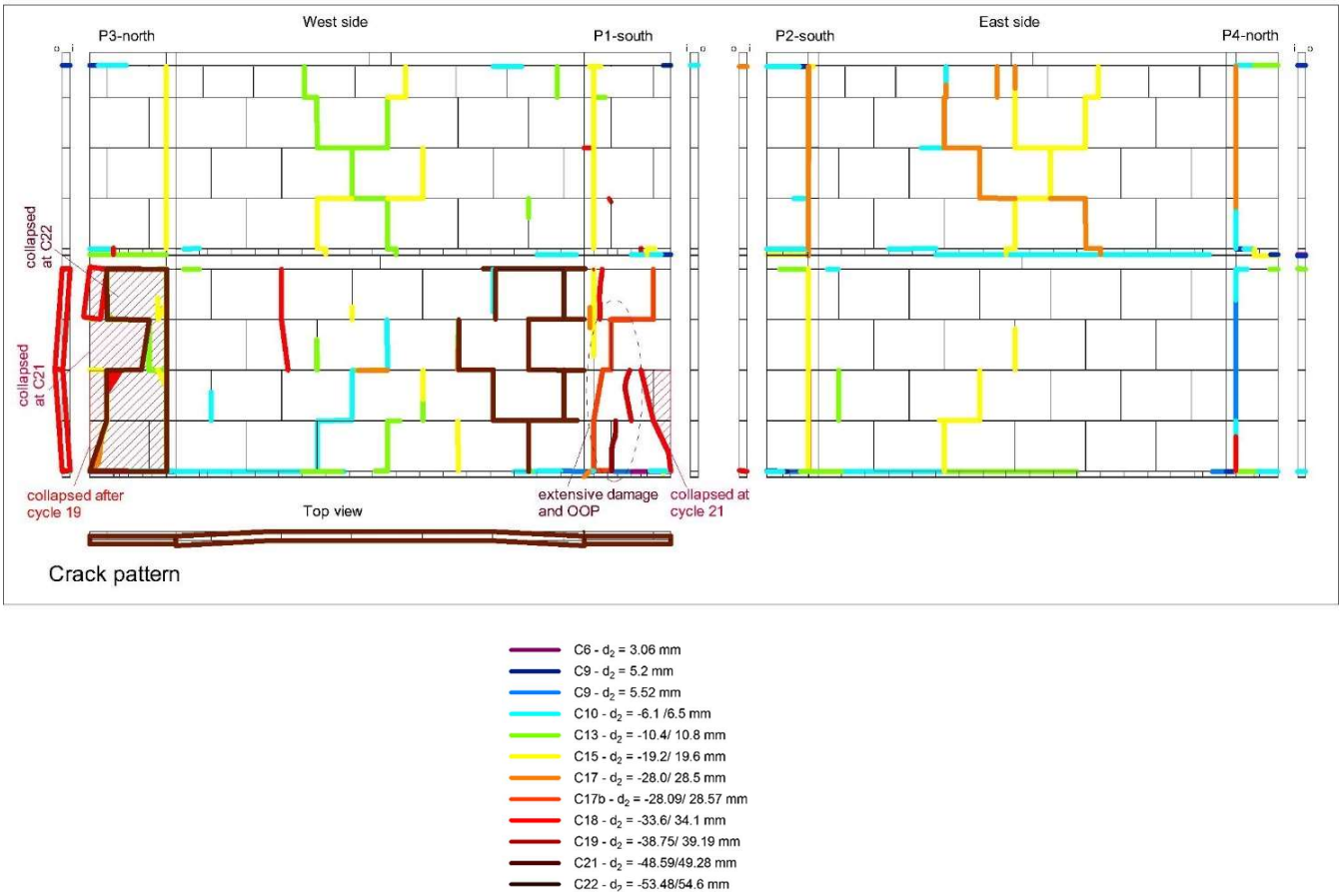

Figure 5.10 Crack pattern evolution

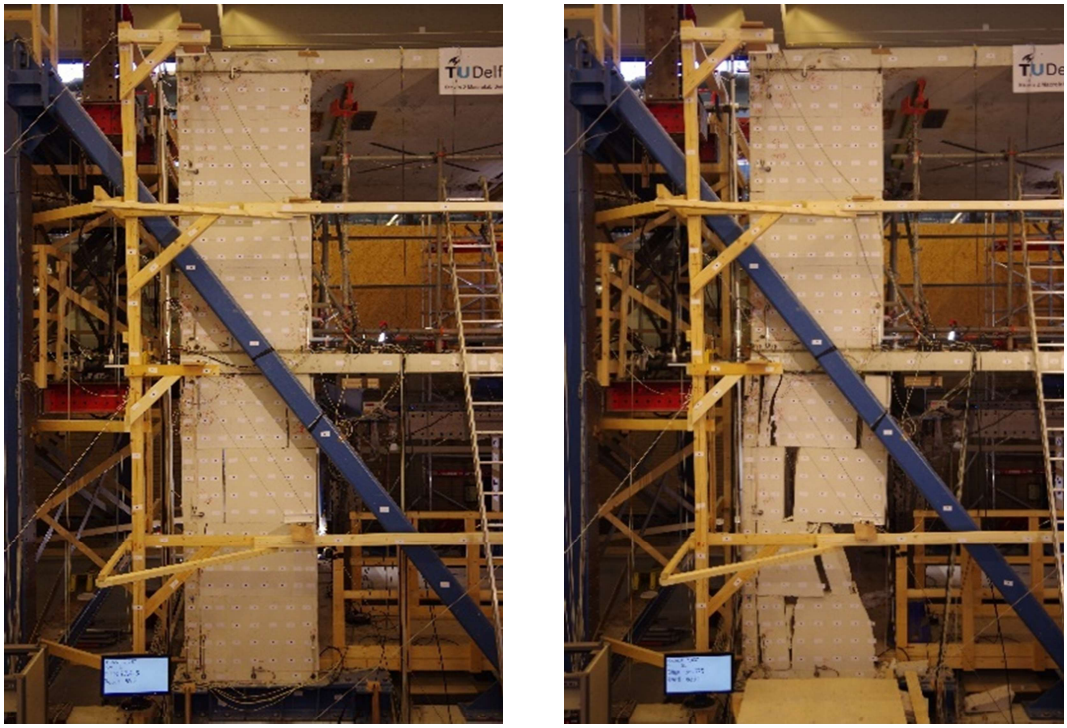

Figure 5.11 Cracks in pier P1 in C17b (left); Partial collapse of pier P1 in C21 (right);

6 In plane walls

6.1 Validation of the analytical model

The analytical calculation follows the simplified formulation recommended by the international standards, as presented in the section 4.3.3. In order to verify the results, several calculations are performed for different values of the mechanical properties of the masonry walls. These values are based on the experimental results obtained in the previous tests performed on masonry components at TU Delft.

When evaluating the analytical results, it can be observed that both specimens show a rocking failure mode, similar to the experiment (Table 6.1 and 6.2).

Table 6.1: Analytical results for the double-fixed walls

	f'm(MPa)	fvo(MPa)	ψ'	Vr(KN)	Vd(KN)
Predicted values	9.96	0.4	0.5	19.68	22.26
Experimentally obtained values	13.39	0.83	0.5	20.06	31.00

Table 6.2: Analytical results for the cantilever walls

	f'm(MPa)	fvo(MPa)	ψ'	Vr(KN)	Vd(KN)
Predicted values	9.96	0.4	1	9.840	12.83
Experimentally obtained values	13.39	0.83	1	10.03	16.74

Figures 6.1 and 6.2 show the influence of the pre-compression level over the shear strength of the piers under different boundary conditions. The graphs also show the influence of the mechanical properties of the masonry piers over the maximum shear strength of the pier.

The results are plotted first by considering the predicted values of the mechanical properties, calculated based on Eurocode recommendations. These values are underestimated when compared to the experimentally obtained values and thus a more conservative result is obtained. A different analysis is then performed for values of the mechanical properties obtained from previous tests performed on masonry components (Table 5.2). The latter results show a much better agreement between the analytically obtained shear strength and the shear strength determined experimentally.

The underestimation of the mechanical parameters leads to an underestimation of the masonry panel strength. The capacity underestimation is more substantial for the masonry panels subjected to shear failure, while the capacity of the piers subjected to rocking failure mode is not influenced to a great extent by the values of the mechanical parameters. This is explained by the fact that the predicted shear strength of masonry is almost half of the shear strength determined in the experiments.

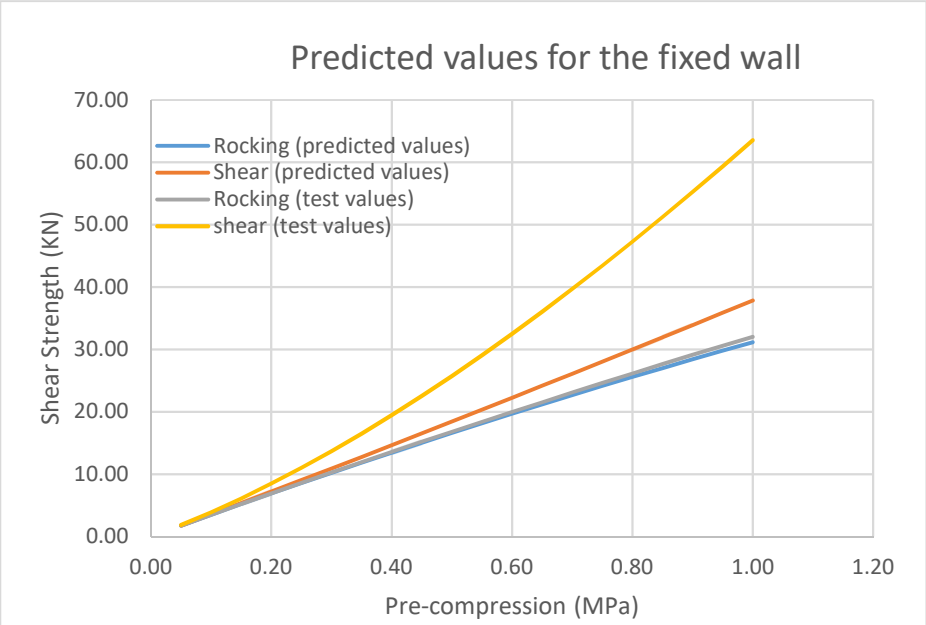

Figure 6.1 Predicted shear strength for the double-fixed wall

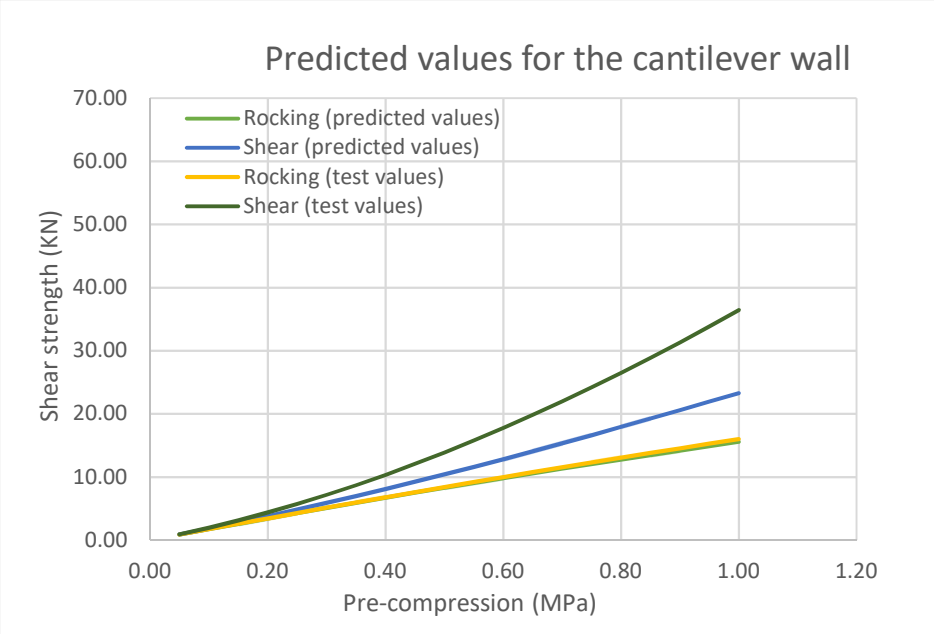

Figure 6.2 Predicted shear strength for the cantilever wall

6.2 Numerical analysis using the equivalent frame approach

A nonlinear static analysis can be conducted in 3Muri to verify the correctness of the values determined with the analytical approaches. The geometry, boundary conditions and the predetermined load need to be defined accordingly. The input parameters and the results obtained are presented in the next sections.

6.2.1 Properties of the EF model

Masonry panel properties

Similar results to the analytical and experimental ones can be obtained if the equivalent frame method adopted by 3Muri is used. Since the software does not allow for the modelling of individual piers, the structural model is built by defining two parallel piers with a length of 0.978m, height of 2.715m and thickness of 10cm, connected at the top by a rigid floor. Orthogonally, the piers are connected by two fictitious transversal walls with insignificant thickness and stiffness (Figure 6.3).

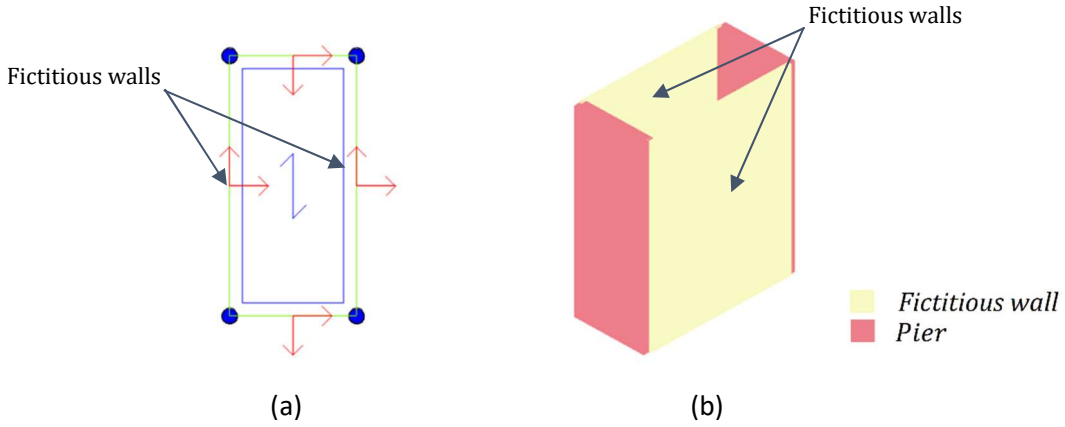

Figure 6.3 Model geometry: (a) top view and (b) 3D view

Material properties of the masonry panels are illustrated in Table 6.3:

Table 6.3: Material properties of the masonry wall

Symbol	Material property	Units	Value	
			Pier	Fictitious wall
E	Modulus of elasticity	N/mm^2	9256	0.0001
G	Shear modulus	N/mm^2	3710	0.0001
w	Density	kg/m^3	2000	0.0001
fm	Mean compressive strength	N/mm^2	13.39	0.0001
fv_0	Shear strength	N/mm^2	0.83	0.0001
Ym	Partial factor	-	1	1

For the cantilever wall, the free extremities must be able to rotate (Figure 6.4, a), while for the double fixed wall, a rotation constraint must be imposed at the top node of the panel (Figure 6.4, b). Constraint nodes are indicated by the orange nodes, while free nodes are represented by the pink nodes.

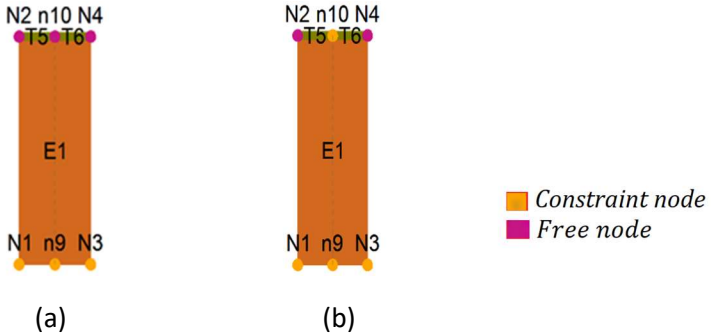

Figure 6.4 Boundary conditions: (a) cantilever pier and (b) double fixed pier

Control parameters

The control parameters correspond to the limit state near collapse and are expressed in terms of drifts, in accordance with the Eurocode 8 recommendations (EN1998-3, 2005):

Drift bending moment: $$\frac{4}{3} \cdot 0.008 \cdot \frac{H_0}{D} = 0.0107 \cdot \frac{H_0}{D} \quad (6.1)$$

Drift Shear: $$\frac{4}{3} \cdot 0.004 \cdot \frac{H_0}{D} = 0.0053 \cdot \frac{H_0}{D} \quad (6.2)$$

The drift for each element is being calculated with the following formula:

$$\delta = \frac{(u_j - u_i)}{h} + \frac{(\varphi_j - \varphi_i)}{2} \quad (6.3)$$

Where:

$u_{i/j}$ nodal horizontal displacement

$\varphi_{i/j}$ nodal rotation

Loading conditions

The loads are applied on the floors in such way that they are transferred to the piers and simulate the test setup. The surface load G_k=117.5KN/m^2 corresponds to the initial loading of the wall (0.6MPa).

For these EF models, the load is a applied as a displacement, in a monotonic way. The load per step is calculated based on the total displacement and the number of substeps chosen in the analysis. The following computational parameters, pre-defined by the software, have been proved to work for most of the structures (Table 6.4).

Table 6.4: Computational parameters

	Units	Test 1
Control Node	-	2
Displacement	mm	100
Substeps	-	200
No. of Iterations	-	400

Constitutive laws

Failure of the piers can be described by shear or rocking failure mechanisms when the drift limit and the structural capacity of the element is exceeded. The shear failure mechanism occurs when diagonal cracking or bed joint sliding develops, while the rocking mechanism appears due to wide flexural cracks in the corner of the masonry wall. The shear force corresponding to the shear failure mechanism can be determined based on a Mohr/Coulomb or a Turnsek/Cacovic constitutive law. The occurrence of any of the failure mechanism depends on the level of the axial force acting on the pier (Figure 6.5)

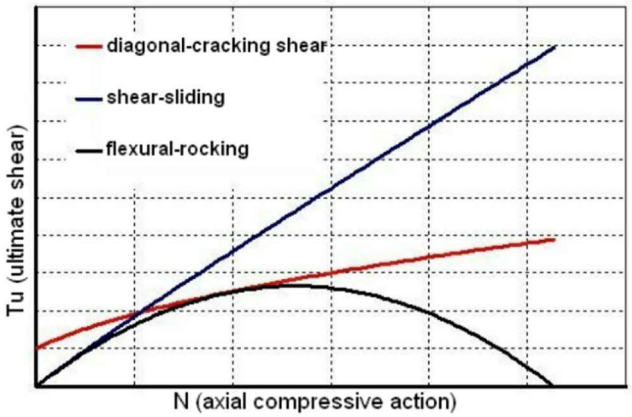

Figure 6.5 Strength criteria comparison (S.T.A.DATA, n.d.-b)

The maximum bending and shear strength of the in-plane loaded walls are computed in 3Muri based on simplified formulations, similar with the ones recommended in the codes and literature (EN1998-1, 2004; Magenes & Calvi, 1997; NZSEE, 2015). The strength criteria for the unreinforced masonry

piers implemented in 3Muri software (Lagomarsino et al., 2013; S.T.A.DATA, n.d.-b) are summarized in the following section:

Rocking behavior

The ultimate bending moment for the rocking failure is defined according to the following formula (S.T.A.DATA, n.d.-b):

$$M_u = \frac{Nl}{2}\left(1-\frac{N}{N_u}\right)=\frac{Nl}{2}\left(1-\frac{N}{0.8 f_u lt}\right) \tag{6.4}$$

Where:

N	axial compressive action
f_u	masonry compressive strength
l	length of the section
t	thickness

Shear failure

The ultimate shear according to Mohr-Coulomb criterion is associated with the sliding of the mortar joint and it is defined as:

$$V_u = l' t f_v = l' t \cdot (f_{v0} + \mu \sigma_n) = l' t f_{vo} + \mu N \tag{6.5}$$

Where:

N	axial compressive action
f_{v0}	shear strength of the masonry without compression
f_v	shear strength of the masonry
l'	length of the compressed section of the panel
t	thickness
σ_n	normal average compressive stress

The ultimate shear can also be computed based on the Turnsek and Cacovic criterion (S.T.A.DATA, n.d.-b). In this case, diagonal shear failure occurs when the principal stress in the masonry panel attains the critical value.

$$V_{u,dc1} = lt\frac{1.5 f_{v0}}{b}\sqrt{1+\frac{N}{1.5 f_{v0} lt}} \tag{6.7}$$

Where:

N	axial compressive action
f_{v0}	shear strength of masonry
b	strength distribution factor, defined according to the ratio of height and length of the wall

A summary of all the input parameters used for the development of the EF model are illustrated in Table 6.5:

Table 6.5: Input parameters

Parameter	Symbol	Units	Value
Length	l	m	0.979
Thickness	t	m	0.1
Height	h	m	2.715
Axial load	N	KN	58.7
Compressive strength	fu	KN/m^2	1339
Shear resistance	fv0	KN/m^2	830
Friction coefficient	μ	-	1.49
Cohesion of mortar	c	N/mm^2	0.3
Stress distribution factor	b		1.5

6.2.2 Numerical results

TUD-COMP-24

To understand the failure of the piers, the forces versus the horizontal displacements are plotted (Figure 6.6). The capacity curve shows a perfect symmetry of the structural behavior in both loading directions. This can be explained by the geometrical symmetry of the model.

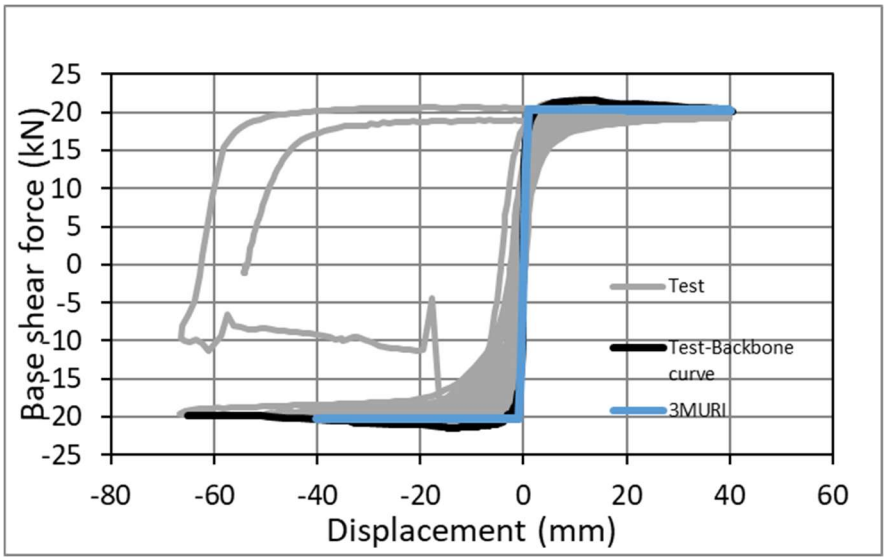

Figure 6.6 Capacity curve of the double-fixed wall

The non-linear static analysis results in a bilinear curve, in which the transition from the elastic branch to the plastic branch can be observed. Once the maximum strength of the masonry panel is reached, the pier cannot be subjected to any load increase, but it can still deform until it reaches the maximum displacement (dm).

In this case, the failure of the EF model is related to the exceedance of the drift limit set corresponding to the governing failure mechanism, when the maximum displacement attains a value of 40.25mm. The ultimate displacement does not depend on the material properties of the panel, but depends on the geometry and boundary conditions.

The drift limits set by standards are similar to the values observed in the experiments. When the drift limit for bending is almost reached (Table 6.6), the wall becomes characterized by rocking failure. The maximum base shear force attained is equal to 20.22KN.

Table 6.6 Drift values

Step	*H(mm)*	*ui(mm)*	*ui(mm)*	*φi*	*φj*	*Drift(%)*
92	2720	0	39.75	0	0	1.46
93	2720	0	40.25	0	0	1.47

Table 6.7 presents the values of the displacements and rotations of the element. As mentioned before, the pier is considered for bending failure at step 93, when the drift limit set the governing failure mechanism is almost reached.

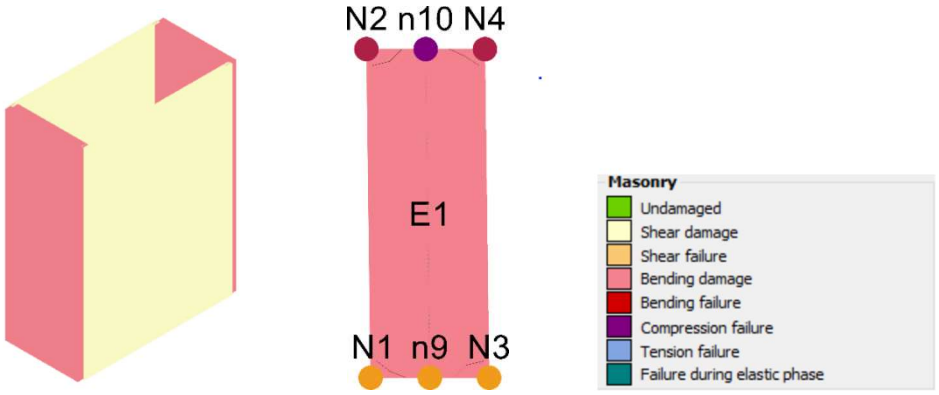

Figure 6.7: Failure mode of the EF model: double fixed pier

The accuracy of the numerical results provided by the program can be verified by analyzing the individual masonry panel. Considering the same value of the axial force and the masonry properties presented before, the ultimate shear can be calculated for different failure mechanisms, according to the strength criteria described in the previous sections (Table 6.7).

The results are in agreement with the software output. The ultimate shear strength corresponds to the compression-bending mechanim (20.06KN) and can be explained by the rather low value of the axial force that acts on the panel.

Table 6.7 Maximum capacity of the double-fixed wall

Strength Criteria	Failure mode	Symbol	Units	μ=1.49
				Value
-	Rocking	M_u	KNm	27.19
-	Rocking	V_u	KN	20.06
Mohr-Coulomb	Sliding failure	V_u	KN	58.312
Turnsek-Cacovic	Diagonal cracking	$V_{u, dc1}$	KN	98.906

TUD-COMP-25

For the analysis of the pier with free top extremities, the same computational parameters and loading conditions are applied.

After the maximum strength is achieved, the element cannot undergo any load increases, but it deforms until it reaches the ultimate displacement. The failure of the pier is considered when the drift limit is reached.

The cantilever pier is assigned to rocking failure related to the exceedance of the bending drift limit in step 163 of the non-linear analysis, at a top displacement of 81mm. This maximum displacement corresponds to the value determined according to the Eurocode (Table 6.8). The maximum shear force attained is equal to 9.66KN.

Table 6.8 Drift values

Step	*H(mm)*	*ui(mm)*	*ui(mm)*	*φi*	*φj*	*Drift(%)*
162	2720	0	80.5	0	0	2.95%
163	2720	0	81	0	0	2.97%

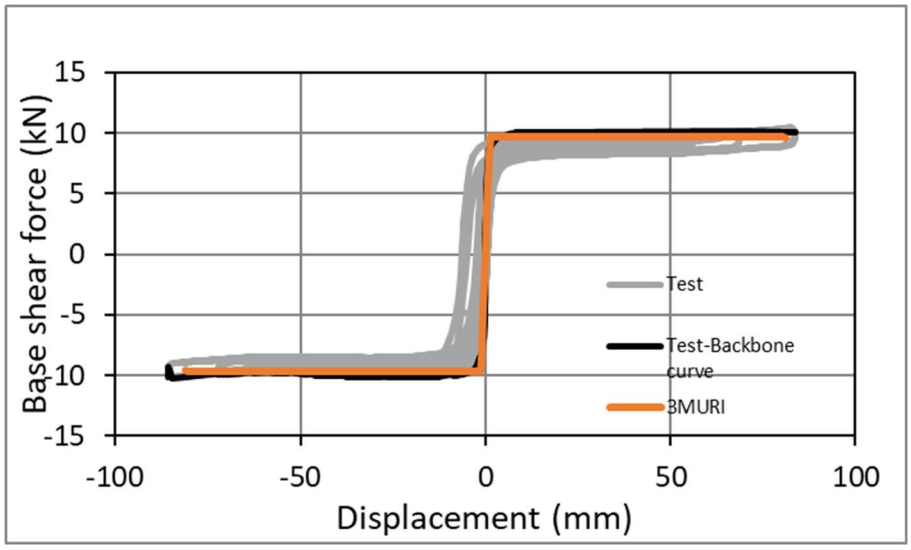

Figure 6.8 Capacity curve of the cantilever wall

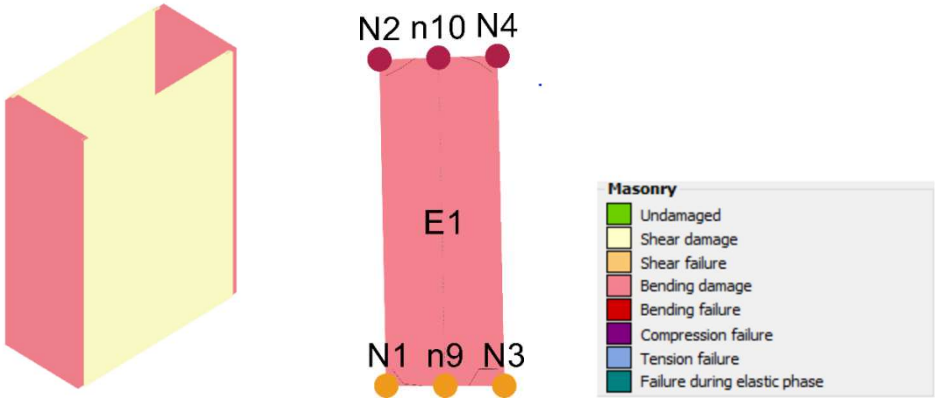

Figure 6.9: Failure mode of the EF model: cantilever pier

Similar to the double fixed wall, the analytical calculation also identifies rocking as the governing failure mechanism and the results are in agreement with the software output (Table 6.9).

Table 6.9 Maximum capacity of cantilever wall

Strength Criteria	Failure mode	Symbol	Units	Value
-	Rocking	M_u	KNm	27.20
-	Rocking	V_u	KN	10.03
Turnsek-Cacovic	Diagonal cracking	$V_{u,dc1}$	KN	78.85

It is worth noticing that a major influence on the results is given by the selected criterion adapted to define the shear-type failure. Usually, the mechanism that gives the lowest shear force is the mechanism that controls the failure. When a Turnsek/Cacovic strength criterion is selected, the ultimate shear corresponding to the rocking mechanism is lower than the shear force corresponding to the shear failure mechanism. As a consequence, rocking failure is identified as the governing failure mode for the double fixed wall (Figure 6.10). Choosing the Mohr-Coulomb strength criterion for the definition of the shear type failure identifies (incorrectly) the shear failure as the governing failure mechanism of the structure due to the fact that the shear corresponding to the shear-type failure mode has the lower value. (Table 6.10):

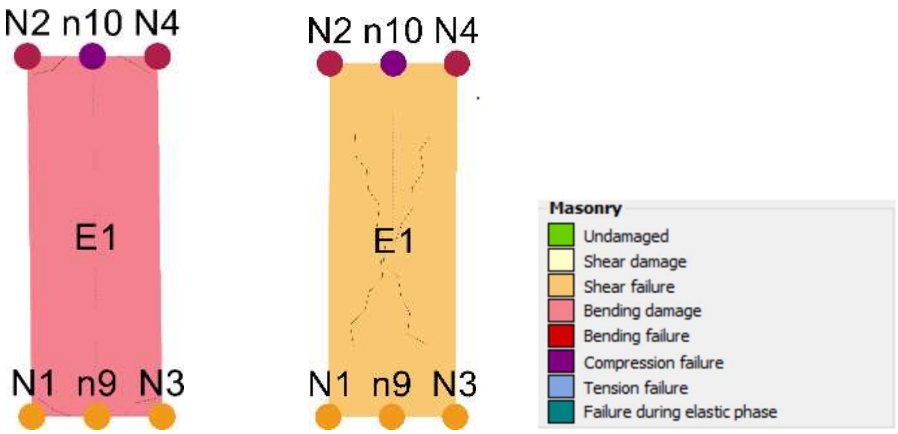

Figure 6.10 Failure mode predicted for the double clamped wall (TUD_COMP-24) assuming the: Turnsek/Cacovic criteria (left); Mohr-Coulomb criteria (right)

These results can be explained by the definition of the friction coefficient in the software. As mentioned in the previous section, the maximum capacity for the sliding failure in a Mohr-Coulomb constitutive law depends on the value of the friction coefficient, μ. A value of μ=1.49 was found during the experiments performed at TU Delft. However, 3Muri does not allow for the definition of this parameter and the Eurocode (EN1996-1-1, 2005) assumes that the friction coefficient is equal to 0.4 in this situation. The maximum shear capacity becomes:

$$V_u = l' t f_v = l' t \cdot (f_{v0} + 0.4\sigma_0) = l' t f_{vo} + 0.4N \tag{6.8}$$

Computing the maximum shear value for different strength criteria and for different values of the friction coefficient shows the importance of this parameter in the evaluation of the failure mechanism. The software underestimates the friction coefficient and this leads to an underestimation of the shear sliding capacity of the wall, while a higher value of the same parameter shows an increase in the maximum shear capacity associated with the failure of the mortar joint and consequently rocking is identified as the critical failure mode (Table 6.10):

Table 6.10 Maximum capacity of the double fixed wall

Strength Criteria	Failure mode	Symbol	Units	Friction coefficient	
				1.49	0.4
-	Rocking	M_u	KNm	27.22	27.22
-	Rocking	V_u	KN	20.06	20.05
Mohr-Coulomb	Sliding failure	V_u	KN	58.32	15.66
Turnsek-Cacovic	Diagonal cracking	$V_{u,dc1}$	KN	98.91	98.91

The previous results show some limitations of the program regarding the definition of material parameters. In the case the friction coefficient is higher than 0.4, the Mohr-Coulomb criterion as defined in the program does not provide reliable results.

However, a Turnsek/Cacovic strength criterion seems to lead to more accurate results and a correct identification of the failure mechanism because the shear force is computed based on a diagonal shear failure mode and the value of the force ($V_{u,dc1}$) depends only on the axial compressive action and the masonry shear strength, as presented in the beginning of the section.

$$V_{u,dc1} = lt\frac{1.5fv_0}{b}\sqrt{1+\frac{N}{1.5fv_0 lt}} = 0.978\cdot 0.1\cdot\frac{1.5\cdot 0.83}{1.5}\cdot\sqrt{1+\frac{58.7}{1.5\cdot 0.83\cdot 0.978\cdot 0.1}} = 98.91KN \quad (6.9)$$

Apart from the correct determination of the material parameters values, the choice of the constitutive law also plays an important role in the outcome of the analysis.

6.2.3 Verification with the experimental results

The capacity of the piers is also assessed by comparing the outcome of the EF modelling approach with the experimental results. The similarity of the results in terms of lateral capacity was already observed in the previous section, when it was shown that the capacity curve obtained from the numerical analysis matches the capacity curve obtained the experiment. (Figure 6.6 and Figure 6.8).

The efficiency of the EF model in predicting the structural response is now evaluated and the results of the experiments, the EF models and the analytical approach are summarized and discussed (Table 6.11 and Table 6.12). Because of the simplicity of the geometry and the simplified approaches used in the evaluation of the structural behavior of the piers, good correlation between the experimental results and the analytical and numerical results is obtained. This outcome, however, is expected since the formulation of the EFM is based on the behavior of the masonry wall.

Table 6.11 Maximum base shear force and failure mode for the double fixed wall

Approach	Direction	Base shear(KN)	Drift	Failure mode
Experiment	pos	21.62	2.45	Rocking
	neg	21.46	2.43	Rocking
Analytical calculation	pos	20.06	1.40	Rocking
	neg	20.06	1.40	Rocking
EF model	pos	20.22	1.40	Rocking
	neg	20.22	1.40	Rocking

Table 6.12 Maximum base shear force and failure mode for the cantilever wall

Approach	Direction	Base shear(KN)	Drift	Failure mode
Experiment	pos	10.28	3.12	Rocking
	neg	10.10	3.06	Rocking
Analytical calculation	pos	10.03	2.97	Rocking
	neg	10.03	2.97	Rocking
EF model	pos	9.66	2.97	Rocking
	neg	9.66	2.97	Rocking

As mentioned before, the masonry walls are characterized by the elastic-perfectly plastic bilinear not hardening model. This means that once the maximum resistance defined by the resistance criterion is reached, the elements cannot be subjected to any load increases, but it can still deform until it reaches the maximum displacement (S.T.A.DATA, n.d.-a).

The capacity curve obtained in 3Muri is characterized by a horizontal plateau after the maximum strength is reached (Figure 6.11), due to the elastic-perfectly plastic constitutive curved adopted. Since no lateral strength decay is registered during the analysis, the software considers that the pier

has reached its limit when the bending drift limit is achieved. Following the nonlinear analysis, the ultimate displacement for actions in the plane of each panel is assumed to be equal to 0.53% of the height of the panel for the shear failure mode and 1.07% of the height of the panel for the bending failure mode.

For the EF models, the drifts corresponding to the governing failure mechanism are similar to the drift limits observed in the tests. The cantilever wall shows almost an identical behavior with the behavior observed in the experiment, while for the double fixed pier, the drift limits predicted by the Eurocode and consequently by the EF model are underestimated with almost 40% in negative direction when compared with the test results.

As mentioned before, the analytical calculation gives a good estimation of the expected capacity of the pier (20.06 KN in the analytical calculation, compared with 21.46KN obtained in the experiment for the double fixed pier). The analytical formulas also show a good correlation in terms of the main failure mode. Both approaches identify rocking as the critical failure mechanism. The calcium silicate masonry walls tested showed a flexural failure mode characterized by pure rocking along the first bed joint, while the analytical formulation indicated a lower value for the bending-compression strength corresponding to the rocking behavior and thus rocking was identified as the governing failure mode.

The analytical approach and the EF analysis also give similar results. This result is expected since both approaches are based on the same formulations. The rocking failure is identified as the critical failure mode for both piers, while the maximum base shear attained is limited to 20.22 KN for the double-fixed pier and 9.66 KN for the pier with free top extremities (Figure 6.11).

The results presented above show that the EF model can be used as an effective tool for predicting the structural response of simple masonry walls.

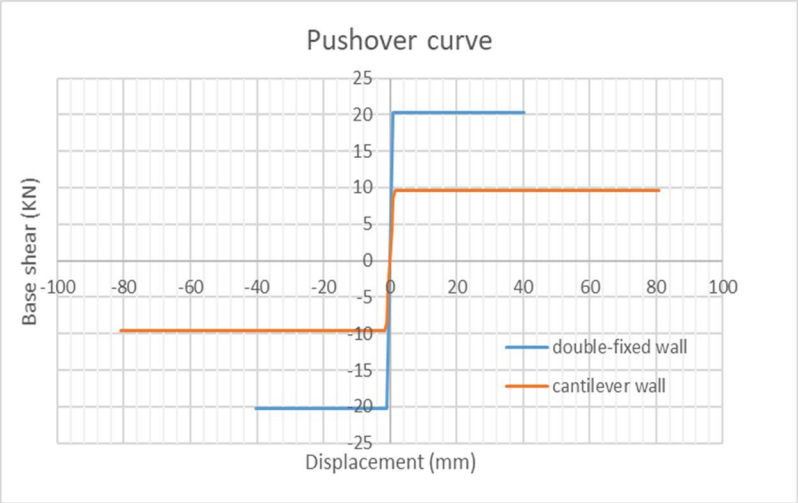

Figure 6.11 Pushover curve comparison

7 Masonry assemblage

To evaluate the applicability of the EF modelling approach, a model sensitivity analysis will be performed. The scope is to find which modelling approach is the most suitable for the assessment of the masonry assemblage. A Simplified Lateral Mechanism Analysis (SLaMA) will also be performed on the 2D wall structure to check the results of the software based analysis. The capacity of the SLaMA method to predict the capacity curve of the structural system will also be evaluated.

An overview of the analyses performed can be visualized in Table 7.1.

Table 7.1 : Analyses overview

Model	Method	Variable	Choice
3D	Numerical	Pier coupling	No coupling
			Weakly coupled
			Strongly coupled
		Load distribution on piers	25%
			50%
			75%
			95%
2D	Numerical	Pier coupling	Strongly coupled
		Load distribution on piers	25%
			50%
			75%
			95%
		Flange effect	No flange effect
			Flange effect included
	Analytical	Pier coupling	Strongly coupled
		Load distribution on piers	50%
		Flange effect	No flange effect
			Flange effect included

7.1 Modelling choices

This section focuses on the numerical study using the software 3Muri. The results discussed here are based on a model with the same loading, mechanical and boundary conditions as the specimen in the experimental tests and the emphasis is given to the failure mechanisms and capacity of the structure in terms of total base shear and maximum displacements.

The input parameters required by the program are limited and refer mainly to the geometry of the structural elements, material and mechanical properties, loading conditions, the elastic spectrum definition and control parameters. Since the model aims to simulate the testing conditions, no partial factors or material factors are considered. A more detailed description of the input parameters is presented in the following sections.

Geometry

The structural model consists of: calcium silicate element masonry walls with a thickness of 100mm in piers, transversal walls with a thickness of 120mm and prefabricated concrete floors with a thickness of 165mm. The floors are supported by both piers and transversal walls. A fixed base is assumed for the model.

The URM structure consists of masonry walls and reinforced concrete slabs with considerable in-plane stiffness and strength. Due to their stiffness, the reinforced concrete slabs can impose an equal displacement on the piers of each story. This kind of coupling can also transfer shear forces and bending moments. Three levels of coupling can be identified in literature (Petry, 2015): (a) weak coupling, where the horizontal elements only enforce equal displacement at each story level, (b) strong coupling, characterized by a strong framing action where horizontal element impose equal horizontal displacement at each story level and transfer shear forces and bending moments and (c) intermediate coupling. The difference between intermediate and strong coupling can be visualized in Figure 7.1. Usually, the URM building with reinforced concrete slabs are characterized by an intermediate coupling, where the reinforced concrete slabs impose an equal displacement on all the piers of one story level and some shear forces and bending moments are being transferred between the piers. The software does not consider the coupling effect of the piers in the façade due to the reinforced concrete slabs and thus additional beams must be inserted to allow for this effect. As a starting point, these beams are fictitious and their material parameters are set to 0 (the software does not allow for material parameters to be set to 0, but instead these values must be set to very low values-0.001). This accounts for the case with no coupling between the piers, in which the forces are not transferred through the connecting elements. Afterward, stiffness is added to these fictitious beams in order to allow the transfer of shear forces and bending moments. Depending on the stiffness of the connecting beam, a weak coupling or strong coupling is obtained between the piers.

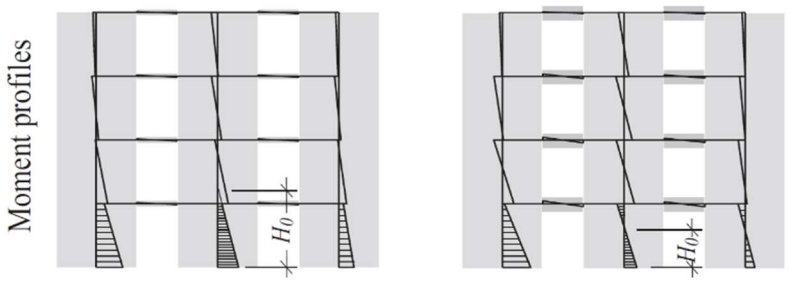

(a) (b)

Figure 7.1 Moment distribution: (a) intermediate coupling and (b) strong coupling (Petry, 2015)

The connecting beams in the models with weak and strong coupling between the piers have the same characteristics as the floor. A constant height of 165 mm is considered, while the width of the beam varies between 100 mm-for the model with weak coupling and 400 mm-for the model with strong coupling between piers. The previous values are based on engineering judgement. The beams are connected to the structure by free rotational nodes.

For the model sensitivity analysis, the following stiffness of the coupling beams is considered:

Table 7.2 Coupling beams stiffness and dimensions

Coupling	Model	Beam dimension (mm x mm)	Stiffness ($x10^6$ Nmm^2)
No coupling	EI0	10x10	0
Weak coupling	EI1	100x165	350
Strong coupling	EI2	400x165	1407

The definition of the structure geometry can be visualized in the Figure 7.2, a and 7.3:

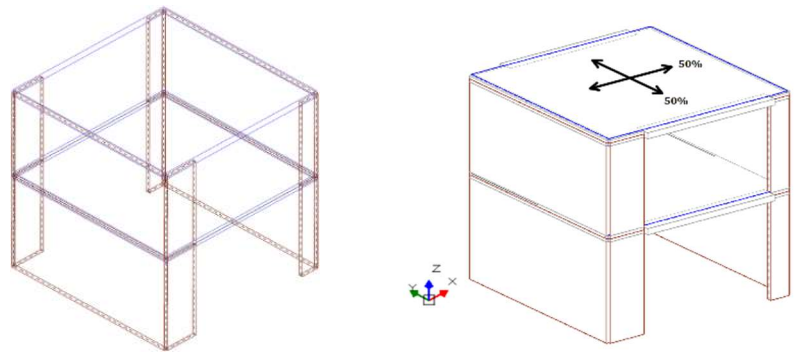

(a) (b)

Figure 7.2 3D Model geometry (a) and load distribution (b)

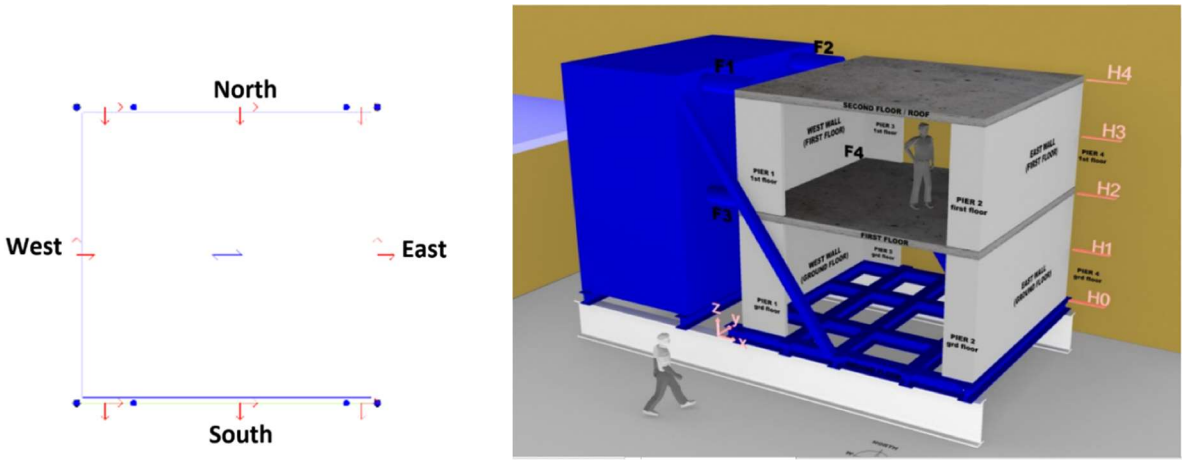

(a) (b)

Figure 7.3 Piers and transversal walls location: 3Muri (a) and test set-up(b) (Esposito, Schipper, et al., 2017)

In order to study the influence of the transversal walls on the overall structural behavior, the results of a three-dimensional model are compared against the results of a two-dimensional model.

In the 3D model, all structural elements are modelled according to their real dimensions and properties, while in the 2D model, only the south and north façade are modelled, while the transversal walls are neglected. Similar to the analysis of the in-plane loaded wall, the piers in the facades are connected in Y direction by two fictitious transversal walls with insignificant thickness and stiffness (Figure 7.4).

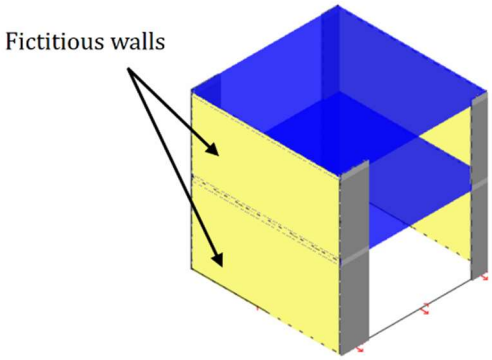

Figure 7.4 2D Model

Model discretization

As it was mentioned before, the equivalent frame method considers the walls as an assemblage of macro-elements (pier, spandrel and nodes). The location of the nodes is illustrated in Figure 7.5. The ideal frame configuration for this structure is straightforward and the structural components can be easily identified. Due to the special configuration of the structure, with large daylight openings in the facades, no spandrel elements or node panels can be identified. The macro-elements identified consist only of the piers and their dimensions and properties are illustrated in Table 7.3. Since the software does not take into account the coupling effect between the piers in the façade and does not consider the floor to be part of the frame that is created with the meshing, additional beam elements are necessary to include the effect of coupling between piers (elements indicated in grey in Figure 7.6).

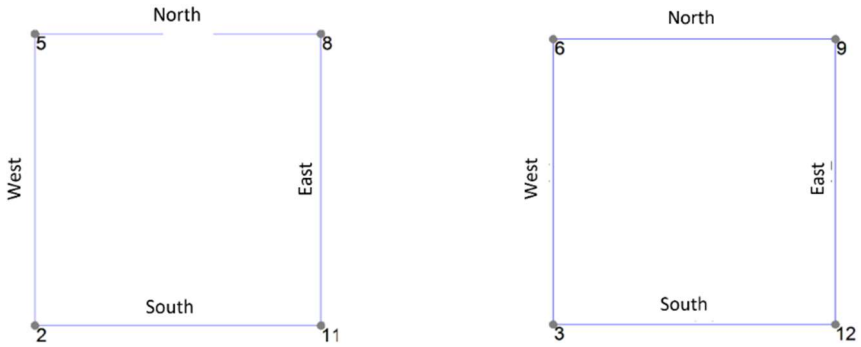

(a) (b)

Figure 7.5 Nodes and walls: (a) level 1 and (b) level 2

Table 7.3 Input parameters for masonry panels

Parameter	Symbol	Units	WP-GF	NP-GF	WP-FF	NP-FF
			Value	Value	Value	Value
Length	l	m	0.979	0.536	0.979	0.536
Thickness	t	m	0.1	0.1	0.1	0.1
Height	h	m	2.83	2.83	2.6	2.6
Axial load	N	KN	90	43.2	45.31	21.6
Compressive strength	fu	KN/m^2	1339	1339	1339	1339
Shear resistance	fv0	KN/m^2	830	830	830	830
Friction coefficient	μ	-	1.49	1.49	1.49	1.49
Cohesion of mortar	c	N/mm^2	0.3	0.3	0.3	0.3
Stress distribution factor	b		1	1	1	1

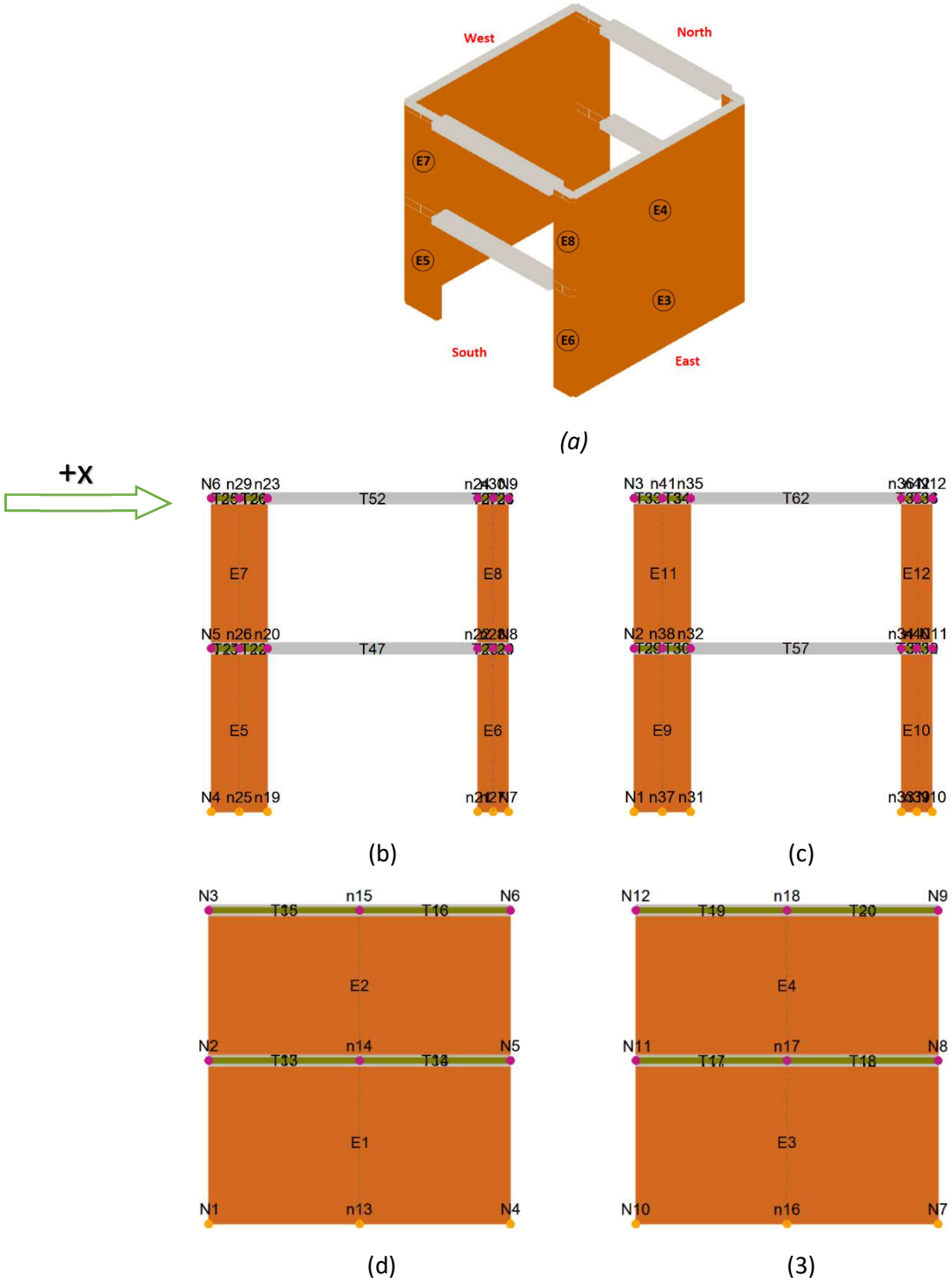

Figure 7.6 Model discretization: (a) 3D model, (b) south façade, (c) north façade, (d) west facade and (e) east façade

The following notations are used interchangeably:

Experiment	3Muri	Notation	Explanation
P1/P3-GF	E5/E9	WP-GF	wide pier-ground floor
P2/P4-FF	E6/E10	NP-GF	narrow pier-ground floor
P1/P3-GF	E7/E11	WP-FF	wide pier-first floor
P2/P4-FF	E8/E12	NP-FF	narrow pier-first floor
West Wall-GF	E1	WW-GF	West wall-ground floor
West Wall-FF	E2	WW-FF	West wall-first floor
East Wall-GF	E3	EW-GF	East wall-ground floor
East Wall-FF	E4	EW-FF	East wall-first floor

Materials

The mechanical properties of the model are derived from the previous tests performed on components. The values are the same with the values used for the in-plane loaded wall analyzed in the previous section. The material properties of the masonry used in the EF model are summarized in Table 7.4. For the prefabricated concrete floors, the same values for the mechanical properties from Section 6 are applied.

The shear failure can be computed based on a Turnsek/Cacovic or a Mohr/Coulomb criterion. The Turnsek/Cacovic criterion represents a type of diagonal failure, while the Mohr/Coulomb criterion represents a type of shear sliding failure. Based on the previous findings from Section 6, a Turnsek/Cacovic strength criteria is chosen as a constitutive law. Apart from the shear failure, a rocking failure mechanism can also occur. The mechanism with the lowest shear force becomes the governing mechanism.

Table 7.4: Material properties of the masonry

Symbol	Material property	Units	Value
			Model
E	Modulus of elasticity	N/mm^2	9256
G	Shear modulus	N/mm^2	3710
w	Density	kg/m^3	2000
fm	Mean compressive strength	N/mm^2	13.39
fv_0	Shear strength	N/mm^2	0.83
Ym	Partial factor	-	1

Loads

The loads applied on the floors are presented in Table 7.5. The gravitational loads acting on the floor slabs are divided between the walls depending on their area of influence and the warping direction. In this case study, the loads are first equally distributed in X and Y direction, between piers and

transversal walls (Figure 7.2, b). For the model sensitivity analysis, the influence of the axial force acting on the piers is studied by varying the load percentage distributed in each direction.

No loading factors are considered, since the numerical model aims to simulate the exact loading condition in the experiment.

Table 7.5: Applied loads

Symbol	Parameter	Unit	Value
G_k	Dead load	KN/m^2	4.5
Q_k	Variable load	KN/m^2	0

Similar to the previous analysis, the lateral load is applied as a displacement load and the same control parameters are used in the analysis (Table 7.6). The load per step represents a critical parameter that defines the failure progression of the structure and is determined as the ration between the total displacement and the number of sub steps. The displacement is applied as a monotonic load and two separate analyses are performed for each direction of loading (+X and -X).

Table 7.6: Computational parameters

Parameter	Units	Analysis 1
Displacement	mm	200
Substeps	-	200
Iterations	-	500
Control node	-	3

Control parameters

The control parameters refer to the capacity of the unreinforced masonry wall controlled by shear and rocking failure and are expressed in terms of drifts. In this case, the parameters correspond to the limit state at near collapse and follow the recommendation of the Eurocode 8 (EN1998-3, 2005). The drift limits for each masonry panel predicted by the Eurocode can be visualized in Figure 7.7.

Drift bending moment: $$\tfrac{4}{3} \cdot 0.008 \cdot H_0/D = 0.0107 \cdot H_0/D \quad (7.1)$$

Drift Shear: $$\tfrac{4}{3} \cdot 0.004 \cdot H_0/D = 0.0053 \cdot H_0/D \quad (7.2)$$

Table 7.7 Drift limits per elements according to Eurocode

Wall	Pier	Height (mm)	Width (mm)	Drift Bending(%)- cantilever wall	Drift Bending(%)- fixed-fixed wall
South façade	E5	2830	978	3.09%	1.55%
	E6	2830	536	5.63%	2.81%
	E7	2600	978	2.84%	1.42%
	E8	2600	536	5.17%	2.58%
North façade	E9	2830	978	3.09%	1.55%
	E10	2830	536	5.63%	2.81%
	E11	2600	978	2.84%	1.42%
	E12	2600	536	5.17%	2.58%

Limit state

Global failure occurs when the capacity of the structure reaches 80% of the peak value of the base shear force or when the first element fails. If the structural capacity does not reach the 80% decay during the non-linear analysis, the global failure is associated with the failure of the first structural element and therefore the Ultimate Limit State (ULS) value occurs with the failure of the first element. The element fails when the drift limit for the governing failure mechanism ("shear" or "bending") is reached.

7.2 Sensitivity study of the EF model

This section focuses on the influence of different parameters on the overall response of the structure. First, the impact of the coupling between the piers is analyzed, followed by the different levels of loading applied on the piers. Additionally, the influence of the transversal walls on the 3D model response is studied in order to provide a better explanation for the global structural behavior.

7.2.1 Coupling between piers

The coupling between the piers has a crucial role in the global response of the structure because it introduces significant in-plane stiffness and lateral strength in the model and allows for equal displacement on the piers of each story. If the coupling is strong enough, it can also transfer bending moments and shear forces between the piers.

An overview of the pier coupling variation and the corresponding results can be visualized in Table 7.8, followed by a more detailed description of the results. Due to the symmetry of the structure, only the results for the piers located in the south façade are illustrated.

Table 7.8 Pier coupling results overview

Approach	Direction	Base shear(KN)	Ultimate displacement(mm)	Drift (%)	Failure mode
No coupling	positive	37.43	202.71	2.90	Rocking-narrow pier (top floor)
	negative	30.63	134.02	1.60	Rocking-wide pier (top floor)
Weak coupling	positive	65.39	83.34	2.35	Rocking-wide pier (top floor)
	negative	48.34	59.59	1.53	Rocking-wide pier (ground floor)
Strong coupling (EI3)	positive	63.95	51.82	1.72	Rocking-wide pier (top floor)
	negative	47.61	49.17	1.53	Rocking-wide pier (ground floor)

- *No coupling between piers*

First, a model with no coupling between piers is analyzed. As mentioned before, fictitious beams with no stiffness are introduced in the model to impose equal displacement on the piers of each story. No shear force or bending moment transfer occurs between the piers in this case. The dead load is equally distributed between piers and transversal walls.

The pushover curve resulted from the EF model analysis is presented in Figure 7.7. The failure is associated with the exceedance of the structural capacity of one of the piers in the façade.

As mentioned before, the software considers the failure of the structure and stops the analysis when the first element reaches the drift limit. This corresponds to a maximum displacement at the top of 134mm and a total shear force of 37.4KN in the positive direction of loading. In negative direction, a maximum displacement at the top of 74.18mm and a total shear force of 30.63KN is observed.

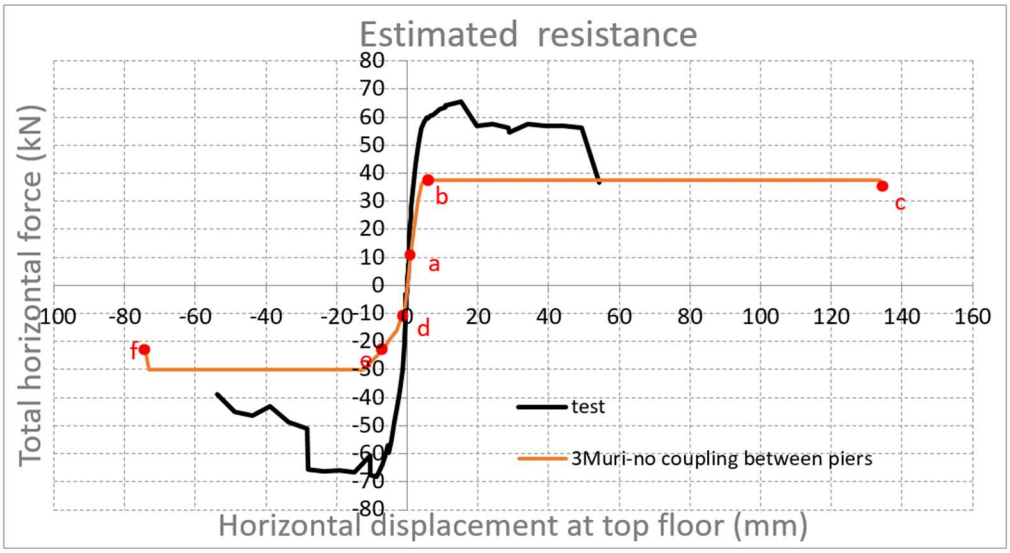

Figure 7.7 Pushover curve of the masonry assemblage (no coupling between piers)

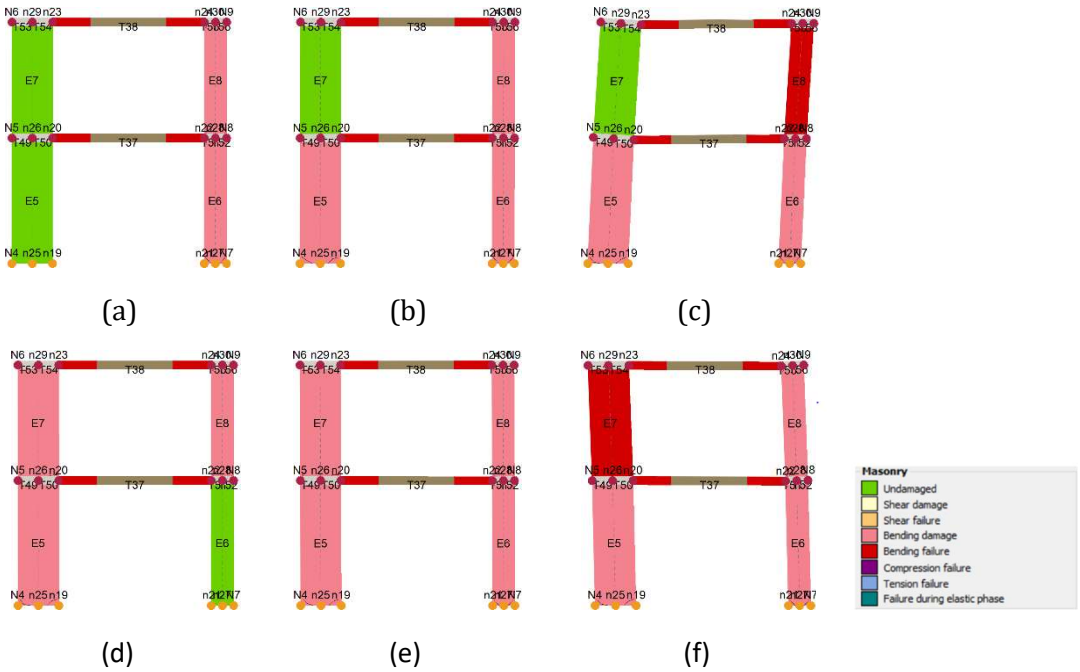

Figure 7.8 Failure progression for the model with uncoupled piers

The failure progression can be observed in Figure 7.8 for both directions of loading. When the structure is loaded in positive direction, the first elements to exceed their bending capacity are the narrow piers, followed by the wide pier located at the ground floor. The wide pier located at the first floor (E7) remains undamaged, since its bending capacity is never reached. When the narrow pier at the first floor reaches the drift limit of 2.90% (Table 7.9), the failure of the entire structure is considered. This is a conservative approach, since the real structure does not fail when the first structural element fails. Due to the redistribution of forces, the structure can be further loaded and the capacity is higher than the one predicted by the pushover analysis.

The drift limit in this case is similar with the drift limit predicted by the Eurocode for a double fixed wall: 2.58% (Table 7.7). The difference of almost 10% between the two drift limits can be explained by the pier boundary conditions considered by the software. During the pushover analysis, the floor is uplifted and thus the connection between the pier and the floor is weakened, which releases the moment resisting connection. In this way, the top of the pier is not fully fixed.

The same behavior can be observed when the structure is loaded in negative direction. The analysis stops at a top displacement of 74.18mm, which corresponds to the failure of the wide pier at the top floor due to the exceedance of the drift limit corresponding to rocking failure. A drift value of 1.60% is observed (Table 7.10), similar to the value predicted by the Eurocode (Table 7.7).

The bending capacity is first reached by the wide piers at both floors, followed by the narrow pier located at the first floor. The last pier subjected to bending damage is the narrow pier at the ground floor (Figure 7.8, e).

Table 7.9 Drift values in positive direction

Step	Element	H(mm)	u_i	u_j	φ_i	φ_i	Drift (%)
135	E8/E12	2600	58.62	134.17	0	0	2.90%

Table 7.10 Drift values in negative direction

Step	Element	H(mm)	ui	uj	φi	φi	Drift (%)
173	E7/E11	2600	31.04	72.68	0	0	1.60

In the end, global failure is associated with the rocking failure of the piers in the façades (Figure 7.9, b) when they reach their maximum drift values, even though, the order in which the piers fail is different from the failure progression observed in the experiment.

The failure mechanism of the model does not correspond to the real failure mechanism observed in the experiment (Figure 5.10), where the cracks started forming in the pre-peak phase between floors and walls connections and the first significant damage occurred in the wide pier at the ground floor located on the north façade (E9). The first collapse occurred at the same location, followed by the collapse of the wide pier at the ground floor located on the south façade (E5). No significant damage was observed in the piers located at the first floor.

The differences related to the base shear force and maximum displacements are also substantial. The underestimation of the results is related to the limitations of the software used for the nonlinear analysis. Since the piers in the facades are not coupled, their behavior is similar to the behavior of a cantilever pier and thus the capacity of the entire structure is also underestimated.

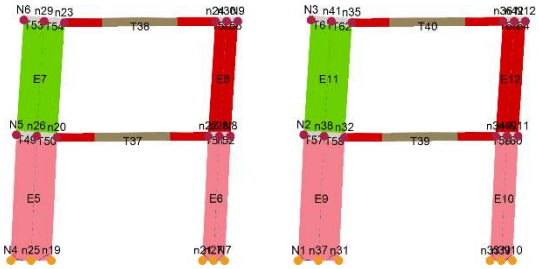

(a)

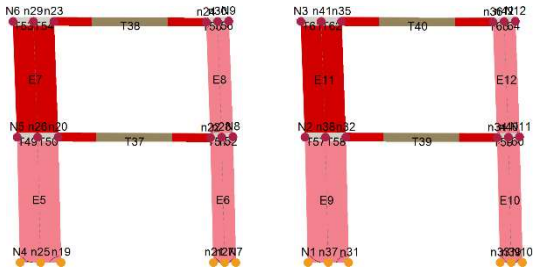

(b)

Figure 7.9 Failure mechanisms in: (a) positive direction and (b) negative direction when the piers are uncoupled

- *Coupled piers*

Usually, the piers are coupled by additional horizontal structural elements (spandrels), but in this case, due to the presence of large daylight openings in the façade, the coupling of the piers is ensured by the structural floors. This, however, is not possible in 3Muri, as the floor system is not capable of providing the frame action necessary for the analysis and no bending moments or shear force transfer occurs between the piers. When the connection between the piers is realized by fictitious beams with no stiffness, it can be observed that the maximum capacity of the structure is highly underestimated, while the ultimate displacement reached by the structure is overestimated with more than 130%. When stiffness is added to the beams that establish the connection between the piers, the maximum capacity of the masonry assemblage increases, as it can be observed when analyzing the capacity curve of the structure (Figure 7.10). A stronger connection between the piers also leads to a different failure mechanism (Figure 7.11) and a lower lateral displacement. The accuracy of the model depends on the correct identification of the level of interaction between the piers and the equivalent stiffness of the coupling beams.

The results of the analysis are illustrated in the Figure 7.10. As mentioned before, the Ultimate Limit State value is defined by the point at which the first element fails. This corresponds to the exceedance of the drift limit set. For the model with weak coupling between piers, the maximum shear force registered is 65.39 KN in positive direction and 48.34 KN in negative direction. These values correspond to a maximum top displacement of 82.34mm in positive direction and 59.59mm in negative direction.

It can be observed that the model with the strong coupling between the piers gives the most accurate results. Nevertheless, by studying the differences between the model with weakly coupled piers and strongly coupled piers a more comprehensive description of the interaction between structural elements and of the global behavior of the structure can be provided.

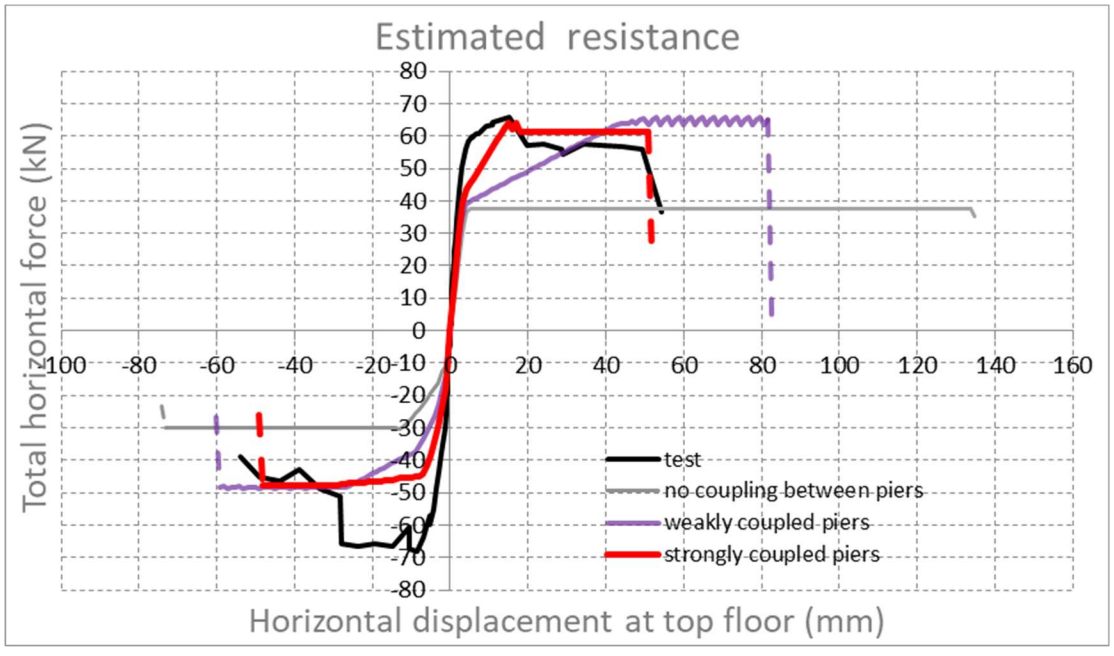

Figure 7.10 Capacity curves for different levels of pier coupling

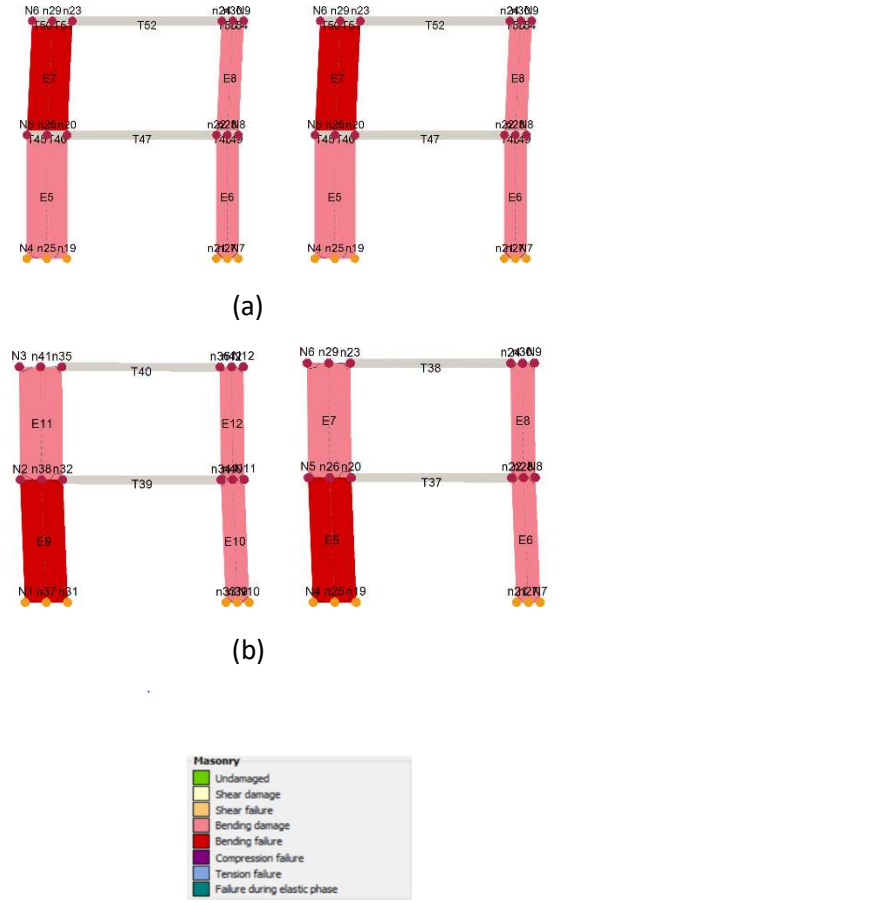

Figure 7.11 Failure mechanisms for weakly coupled piers in: (a) +X and (b) -X direction

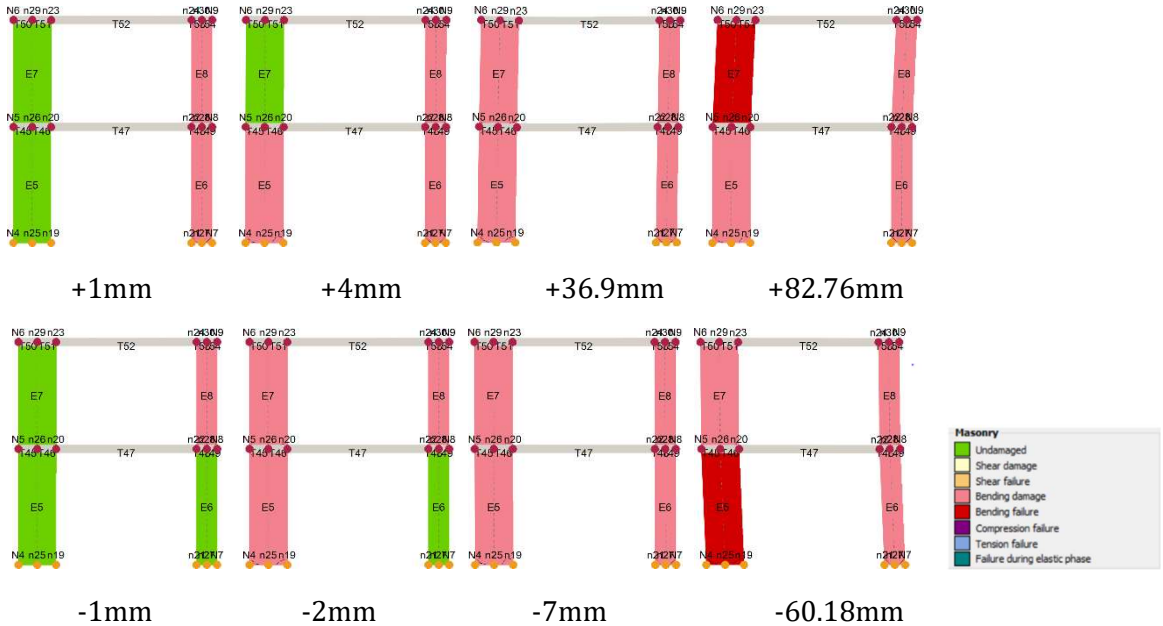

Figure 7.12 Failure progression for the model with weakly coupled piers

The failure progression of the elements is illustrated in Figure 7.12. When the structure is loaded in positive direction, the failure occurs due to the rocking failure of the wide piers at the first floor. The failure is associated in positive direction with the exceedance of the drift limits for both wide piers located at the top floor (E7 and E11). These elements fail when they reach a drift limit of 2.35% (Table 7.11), which is similar to the drift limit of a cantilever wall defined by the Eurocode (Table 7.7). The failure of this element can be explained by the fact that at the end of the analysis, the top pier stops acting as a fixed wall at both ends. The slab located at the first floor only carries loads at the end of the slab due to its self-weight and the interaction with the top narrow pier. At the location of the top wide pier, the floor is uplifted, the rotation at the top of the pier is released and consequently the drift limit of the wide pier at the top floor (E7) can be determined in reference to the cantilever boundary conditions (Table 7.7). The floor uplifting that leads to the releasing of the top end of the piers is illustrated by the relative displacement between the wide top pier and the floor located at the top floor (Figure 7.13):

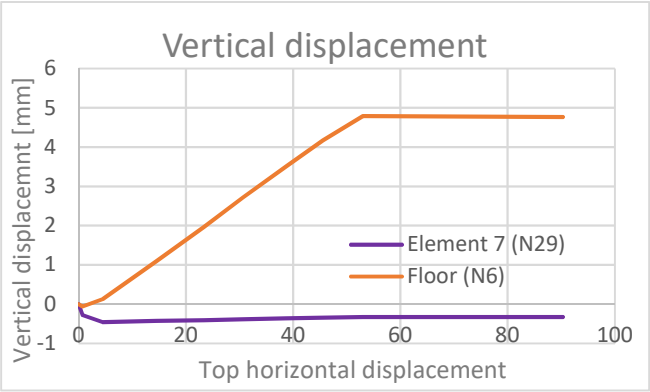

Figure 7.13 Vertical displacement of structural elements

If the structure is loaded in negative direction, the failure is associated with the failure of the wide pier at the ground floor (E9), which is also the element that attains the maximum drift value. The failure progression (Figure 7.12, second row) is similar and the collapse occurs when both wide piers located at the ground floor reach a drift limit of 1.53% (Table 7.12), similar to the limit predicted by the Eurocode for a double fixed wall (1.55%). The piers in question do not behave as a cantilever wall, as it was the case with the piers located at the first floor. In this case, the floor is not uplifted, but it has an out-of-plane stiffness that restraints the rotations of the piers and thus the drift limit can be defined as the drift limit for a double fixed wall.

Table 7.11 Drift values per elements in +X direction before the failure of E7 (weak coupling)

Element	H(mm)	u_i	u_j	φ_i	φ_i	Drift	Drift %
E5/E9	2830	0	21.28	0	0	0.0075	0.75
E6/E10	2830	0	21.28	0	0	0.0075	0.75
E7/E11	2600	21.28	82.35	0	0	0.0235	2.35
E8/E12	2600	21.28	82.25	0	0	0.0235	2.35

Table 7.12 Drift values per elements in -X direction after the failure of E5 (weak coupling)

Element	H(mm)	u_i	u_j	φ_i	φ_i	Drift	Drift %
E5/E9	2830	0	43.17	0	0	0.0153	1.53
E6/E10	2830	0	43.17	0	0	0.0153	1.53
E7/E11	2600	43.17	58.59	0	0	0.0059	0.59
E8/E12	2600	43.52	58.59	0	0	0.0058	0.58

A similar behavior can be found for the model with strong coupling between piers, even though some differences are worth mentioning.

The failure of the building is related in this case to the failure of the first structural element and occurs in the same elements as in the previous model (wide pier at the first floor for the positive direction and wide pier at the ground floor for negative direction of loading). The order in which the elements are first subjected to bending damage is also similar(Figure 7.14). Due to a stronger link between the piers, the ultimate displacement of the structure is reduced, while the difference in the total base shear force for the two models is insignificant.

If for the negative direction the failure occurs when the wide pier reaches the same value of the drift limit (1.53%), for the positive direction of loading, the model with strong coupling between piers gives a lower value of the drift limit than the model with weak coupling (1.72% compared with 2.35%). This value is closer to the value predicted by the Eurocode for a double fixed wall (Table 7.7), which indicates that the increased stiffness of the connecting beams also restricts the rotation at the top for the piers located at the first floor, and thus the walls behave more as double fixed walls than cantilever walls, as it was the case in the previous situation. The drift limits recorded are illustrated in the Tables 7.13 for positive direction and Table 7.14 for negative direction:

Table 7.13 Drift values per elements in +X direction before the failure of E7 (strong coupling)

Element	H(mm)	u_i	u_j	φ_i	φ_i	Drift	Drift %
E5/E9	2830	0	6.86	0	0	0.0024	0.24
E6/E10	2830	0	6.86	0	0	0.0024	0.24
E7/E11	2600	6.86	51.52	0	0	0.0172	1.72
E8/E12	2600	6.86	51.52	0	0	0.0172	1.72

Table 7.14 Drift values per elements -X direction before the failure of E5 (strong coupling)

Element	H(mm)	u_i	u_j	φ_i	φ_i	Drift	Drift %
E5/E9	2830	0	43.22	0	0	0.0153	1.53
E6/E10	2830	0	43.22	0	0	0.0153	1.53
E7/E11	2600	43.22	47.47	0	0	0.0016	0.16
E8/E12	2600	43.52	47.47	0	0	0.0015	0.15

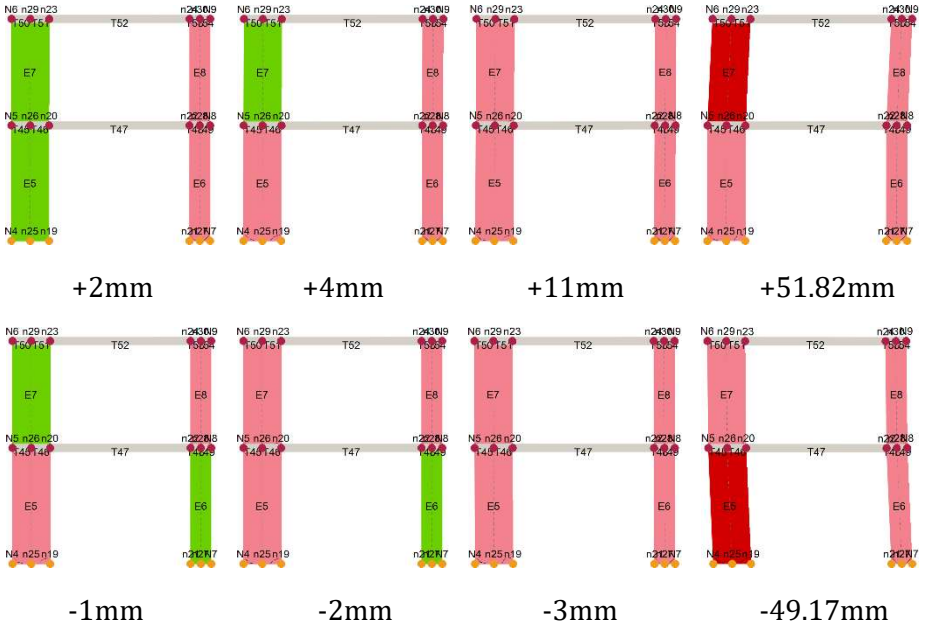

Figure 7.14 Failure progression for the model with strongly coupled piers

Figure 7.15 illustrates the influence of the coupling between piers in terms of floor displacement. For both models, the initial stages of the analysis show similar ratios between the floor's displacements for both direction of loading. As the analysis progresses, it can be observed that for the positive direction, the first floor shows higher displacements, while for the negative direction of loading, the ground floor is the one that shows the larger displacements. However, the maximum displacement is significantly reduced in positive direction when the piers in the façade are strongly coupled. This behavior corresponds with the failure mechanism due to the exceedance of the drift limits reported for the two loading directions (Figure 7.14).

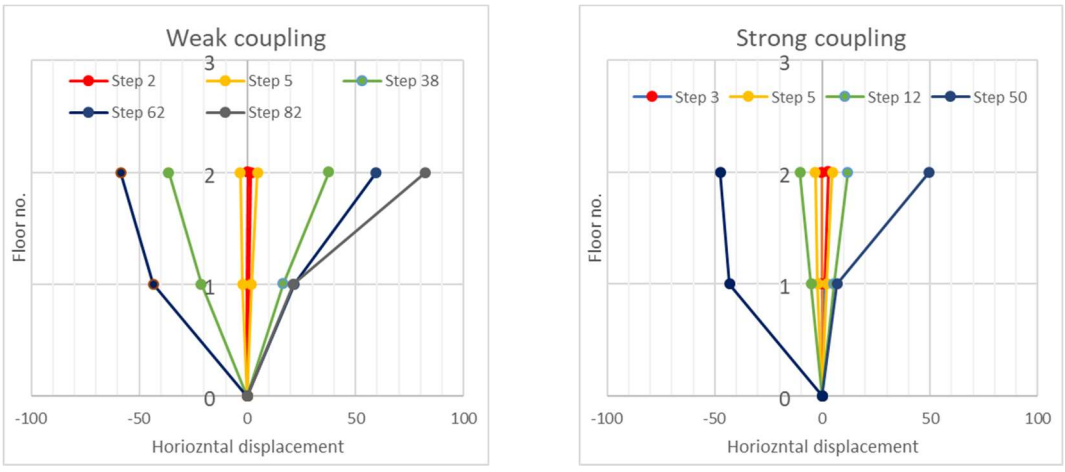

(a) (b)

Figure 7.15 Horizontal displacement per step: (a) weak coupling and (b) strong coupling

- *Internal force distribution*

The internal force distribution is similar for the models with weak and strong coupling, even though some difference can still be observed.

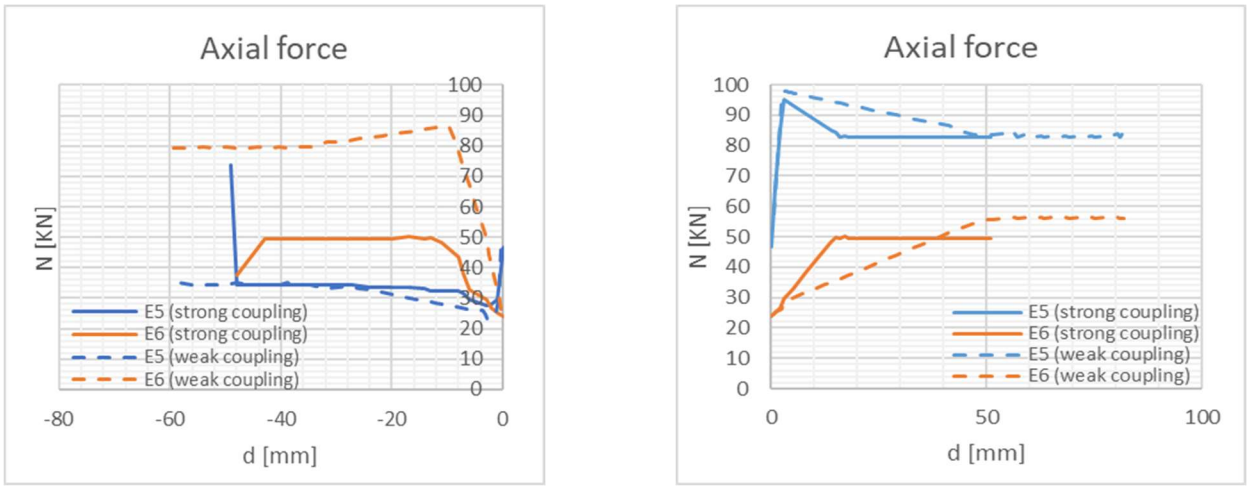

(a) (b)

Figure 7.16 Axial force in the ground floor piers: (a) negative direction; (b) positive direction

A stronger connection between piers leads to a more active interaction and force transfer between the piers and transversal walls. If for the positive direction of loading, the internal force distribution is similar for both models, for the negative direction of loading, a significant difference in the peak value of the axial force in the wide pier at the ground floor (E5) is observed between the model with weak and strong coupling. This behavior suggests that when coupling between piers is strengthened, the axial load corresponding to the transversal walls located at the ground floor is not redistributed only to the adjacent pier, but also to the other elements in the structure. A more detailed description of this behavior is illustrated in Annex A.

In order to explain the mechanism of force redistribution between the structural elements, attention will be given only to the model with strongly coupled piers.

When loaded in positive direction, the wide pier at the ground floor (E5) is subjected to an increase in axial load, together with the narrow pier at the ground floor (E6) and the narrow pier at the first floor (E8). The wide pier at the top floor is subjected to a decrease in axial load (Figure 7.17, b). This variation follows the distribution of the axial load in the transversal walls.

It can be observed that during the analysis, the axial load is transferred between transversal walls and piers. The bottom west wall (E1) is subjected to a decrease in axial load due to the rotation and lifting of the wall. By the end of the analysis the axial load is only carried by the bottom east wall (E3) and top west wall (E2), which suffer a substantial increase in axial load. This distribution alters the variation of axial load in the piers in the façades and affects their rocking and toe crushing capacity. The increase in axial load in E5 follows the decrease in axial load of the transversal wall located at the ground floor (E1), as it can be observed in Figure 7.18, b. It can also be noticed that the maximum axial force registered in E5 is reached when the structure attains a top displacement of 3mm. This

point also corresponds to the point where the floor and walls located on the west side are lifted and the west wall located at the ground floor (E1) stops carrying any loads. Pushing the structure in one direction may lead to the lifting and rotation of the walls and consequently to cracking in the transversal wall. While some force redistribution is expected between structural components, the large variation in the axial force observed in the piers and transversal walls in the EF model is not fully understood. It is possible that in this case the software considers the transversal walls to be completely dislocated from the structure and thus the forces corresponding to these walls are redistributed to other structural elements. Nevertheless, this structural behavior did not occur in the real masonry house, suggesting that the numerical results obtained are not reliable. In the experiment, cracking occurred at the bottom of the transversal walls when the structure was loaded in positive or negative direction, but the walls were never completely dislocated and thus they were able to preserve their load bearing capacity.

In a similar way, the top wall located on the east side (E4) gradually transfers the axial force to the adjacent narrow pier at the first floor (E8), until the structure attains a top displacement of 16 mm and the axial force in the transversal walls and reaches the maximum value in the E8 (Figure 7.17, b).

Because the structure is not perfectly symmetrical (the wide piers are almost twice as large as the narrow pier) a difference in the internal force pattern is also observed for the two directions of loading. The difference is even more noticeable when the piers are strongly connected. This behavior can also be explained by the force transfer that occurs between transversal walls and adjacent piers.

In the negative direction of loading, a different progression of the failure mechanism is also observed (Figure 7.14), which enforces the idea that the piers are sensitive to the loading direction and that a variation of the axial load occurs that influences the bending capacity of the pier and the maximum drift limit. The total base shear force and ultimate displacements have lower values in negative direction as well.

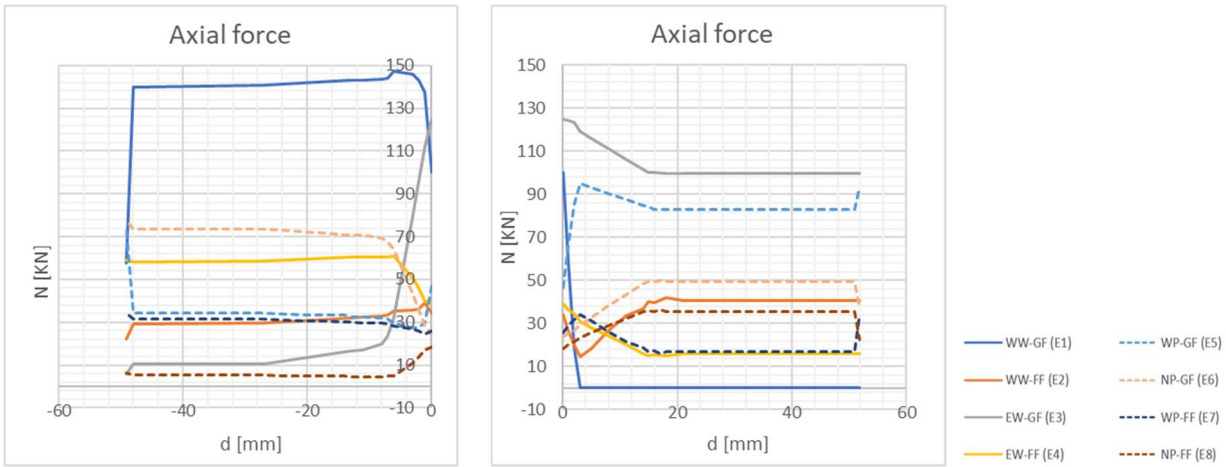

(a) (b)

Figure 7.17 Axial force distribution for the model with strong coupling: (a) negative; (b) positive direction

The axial load redistribution is also different when the structure is loaded in negative direction (Figure 7.17, a). In this case, the transversal wall located on the east side at the ground floor is subjected to a decrease in axial load (E3) and only a small part of its axial force is transferred to the

adjoining pier, the narrow pier from the ground floor (E6), while the rest of the load resolves on the transversal wall at the ground floor located on the opposite side (E1). As mentioned before, this behavior becomes more important when the piers are strongly coupled, since it allows for an easier transfer of the load from the eastern part of the structure to the western part through both the connecting beams and floor slabs. This behavior can also explain the different failure mechanisms that occur in the negative direction of loading. In this case, the wide pier located at the ground floor has a lower axial force and thus it can reach its bending capacity before any other structural elements.

The difference in structural response between the two directions of loading is related to the difference in the piers dimension located on the left and right side of the opening, which leads to an asymmetrical distribution of the axial loads in the structure. The depth of the compression zone of the piers located on the east side is also small in comparison to when it is loaded in negative direction. When the structure is loaded in positive direction, most of the load resolves on the western wide pier and the piers located on the east side, while the axial load on the walls located on the west side is substantially reduced. A similar behavior is observed in the negative direction of loading, even though in this case a larger amount of the load is distributed to the transversal walls located on the opposite side, than to the adjacent piers.

As it can be observed in Figure 7.14 and Figure 7.18, a, in the negative direction of loading, the first element subjected to bending damage is the narrow pier located at the first floor (E8), in the early stages of the analysis, followed by the wide pier at the ground floor (E5) at a top displacement of 1 mm. The narrow pier at the ground floor (E6) exceeds its bending capacity at top displacement of 3 mm. In the end, failure is concentrated at the ground floor and it is associated with the exceedance of the drift capacity of the wide pier located at the ground floor.

For the positive loading direction, for the model with strong coupling, the bending damage progression (Figure 7.14) corresponds to the exceedance of the bending moments capacities. The first elements subjected to bending damage are the narrow piers (E8 and E6), followed by the wide pier at the ground floor, at a top displacement of 3.99 mm, and element E7 at a top displacement of 10.96 mm (Figure 7.18, b).

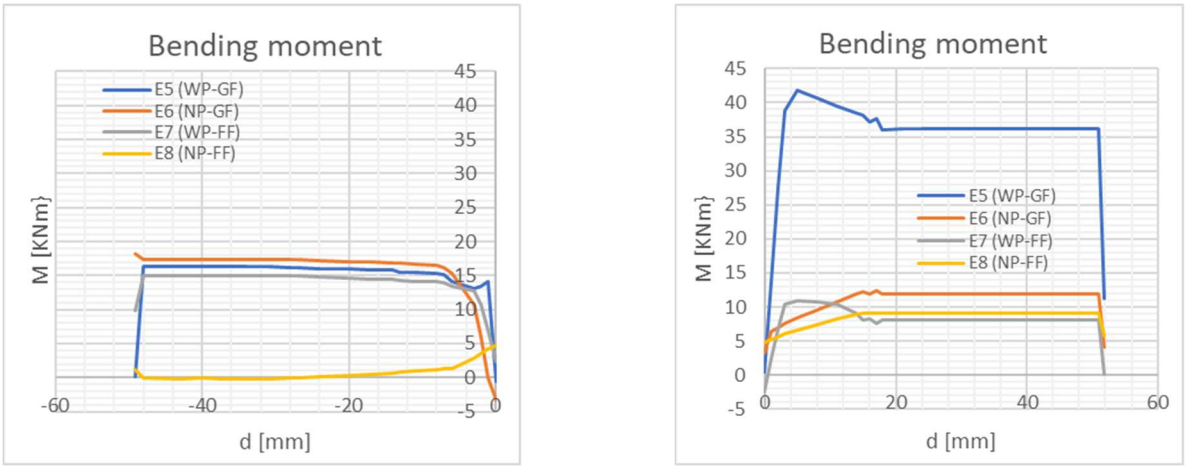

(a) *(b)*

Figure 7.18 Bending moment distribution when the piers are strongly coupled: (a) negative and (b) positive direction

Table 7.15 and Table 7.16 illustrate the bending capacity of each element before the damage occurs in these elements. The values are in accordance with the internal force distribution presented in Figure 7.18.

Table 7.15 Bending capacity exceedance per element for the model with weak coupling

Element	Global Displacement (mm)	Axial force (KN)	Bending capacity (KNm)
E8	0.8	22.00	4.37
E6	0.8	23.00	4.19
E5	4.18	103.00	32.34
E7	39.96	19	7.03

Table 7.16 Bending capacity exceedance per element for the model with strong coupling

Element	Global Displacement (mm)	Axial force (N)	Bending capacity (KNm)
E8	1	20.08	3.65
E6	1	25.18	4.57
E5	3.99	94.08	29.80
E7	10.96	22.92	8.45

In Table 7.17 the initial bending capacities of each elements have been determined based on the analytical formulation presented in Section 4.3.3. These bending capacities are calculated considering a value of the axial load that corresponds to an evenly distributed dead load between X and Y direction (between piers and transversal walls) and thus they only offer an indication of the most vulnerable elements in the structures.

In this case, the capacity is expected to be first exceeded for element 8 (narrow pier located at the first floor), followed by the rest of the elements. However, these results differ from the previous findings. During the analysis, the piers are susceptible to the loading direction which leads to a variation of the axial load for every element (Figure 7.18) and thus the bending capacity of each element differs from the estimated bending capacity.

Table 7.17 Strength criteria for masonry panels

Strength criteria	Symbol	Units	Pier			
			E5 (WP-GF)	E6 (NP-GF)	E7 (WP-FF)	E8 (NP-FF)
Rocking	M_u	KNm	22.93	6.67	11.96	3.56
Diagonal cracking	$V_{u,dc1}$	KN	114.42	62.31	104.27	57.05
Sliding failure	V_u	KN	73.04	38.76	37.28	20.28
Compression-bending	V_u	KN	16.21	4.71	9.20	2.74

The previous results show the importance of the coupling and interaction between the piers on the overall structural response. A strong coupling between piers allows for force redistribution between transversal walls and piers and limits the lateral displacement of the structure by imposing rotational restraints at the top of the piers.

However, when studying the internal force distribution in the three-dimensional model, it is observed that the behavior of the transversal walls is not in accordance with the behavior observed in the tests. The numerical results show that the entire axial load corresponding to transversal wall is redistributed between other structural elements. This response cannot be controlled in the software used for the EF analysis, suggesting some limitations of the software. Consequently, caution is necessary when interpreting the results and evaluating the structural response.

7.2.2 Load distribution on the piers

The overburden on the piers also has an influence on the overall capacity of the structure and the maximum drifts attained. The load that has to be distributed on the piers includes the dead load from the floor slabs. The following load distributions are considered for the analysis:

Table 7.18 Load distribution variation

Model	Total Load	Load in X direction (Transversal walls)	Load in Y direction (Piers)
25%	100%	75%	25%
50%	100%	50%	50%
75%	100%	25%	75%
95%	100%	5%	95%

The influence of the applied vertical load on piers on the overall capacity of the structure is investigated for the 3D model in which the transversal walls are modelled according to their real dimensions and stiffness. A strong coupling between the piers is considered, based on the previous findings. The results can be visualized in Figure 7.19 and Table 7.19.

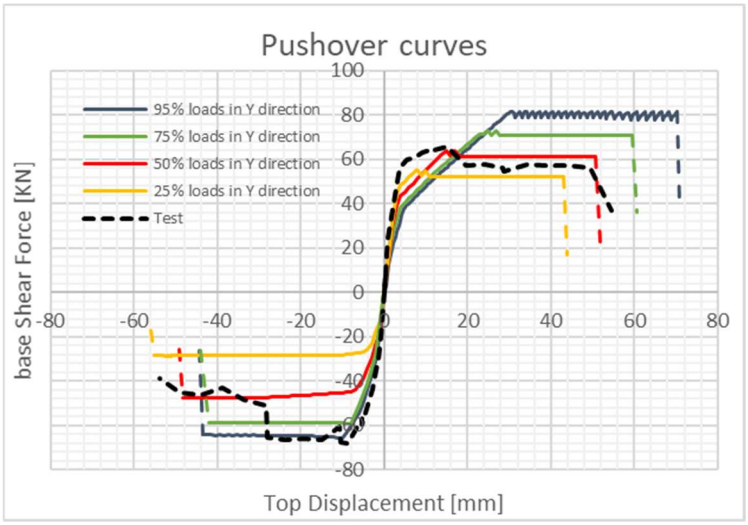

Figure 7.19 Pushover curve comparison

As it can be observed in Figure 7.19, the applied vertical load has an influence on the structural capacity and the maximum top displacement attained. When the structure is loaded in positive direction, it can be observed that maximum base shear force increases as the applied load level on the pier increases (from 53.84KN, for the model with 25% of the loads distributed on the piers to almost 81 KN for the model with 95% of the load applied to the piers). These results are to be

expected, since the bending capacity of a masonry wall depends on the axial force level. The ultimate displacement is also susceptible to the variation of the load in the piers.

In negative direction, the same variation of the total base shear force with the level of pier loading can be observed, even though the maximum base shear force is lower, suggesting that the overall behavior is sensitive to the direction of loading. The base shear force varies from 26.82 KN for the model with 25% pier loading to 64.28 for the model with 95% of the loads distributed to the pier.

The results of the analysis are summarized in Table 7.19.

Table 7.19 Model overview for different load distribution on the piers

Model	Direction	Base shear(KN)	Ultimate displacement(mm)	Drift (%)	Failure mode
25% loads in Y direction	positive	53.84	43.96	1.57	Rocking-wide pier (top floor)
	negative	28.34	56.05	1.54	Rocking-wide pier (ground floor)
50% loads in Y direction	positive	63.95	51.82	1.72	Rocking-wide pier (top floor)
	negative	47.71	49.17	1.53	Rocking-wide pier (ground floor)
75% loads in Y direction	positive	70.93	60.61	1.91	Rocking-wide pier (top floor)
	negative	59.05	44.14	1.5	Rocking-wide pier (ground floor)
95% loads in Y direction	positive	81	71	1.93	Rocking-wide pier (top floor)
	negative	64.28	44.10	1.5	Rocking-wide pier (ground floor)

As mentioned before, the presence of transversal walls in the three-dimensional model alters the internal force distribution in the structure, which leads to a different failure mechanism in the two directions of loading. When the structure is subjected to lateral loading, for a certain value of lateral displacement, the software considers that the entire load corresponding to these walls is redistributed between other structural elements.

If looking at the failure progression in the different models, several similarities can be found between the models. When the structure is loaded in a positive direction, the failure is concentrated at the first floor (Figure 7.20, first row), while for the negative direction of loading, the global failure is concentrated at the ground floor (Figure 7.20, second row). The failure of the structure occurs when the first element exceeds the drift limit defined for the governing failure mechanism.

In positive direction, the first damage occurs in the narrow piers, followed by the wide pier at the ground floor (E5). A slightly different failure progression can be observed for the models with a lower level of pier loading for which the last pier subjected to bending damage is the narrow pier located at the ground floor, instead of the wide pier. Failure occurs in the wide pier located at the first floor of the structure (E7). The failure progression is also similar for the negative direction of loading, with the first pier subjected to bending damage being the short piers (E6 and E8), followed by the wide piers located at the ground floor (E5) and the wide piers located at the first floor (E7). A more detailed description of the structural behavior for different levels of axial load applied to the piers is presented in Appendix B.

The top displacements where damage occurs are similar for all the models (Figure 7.20).

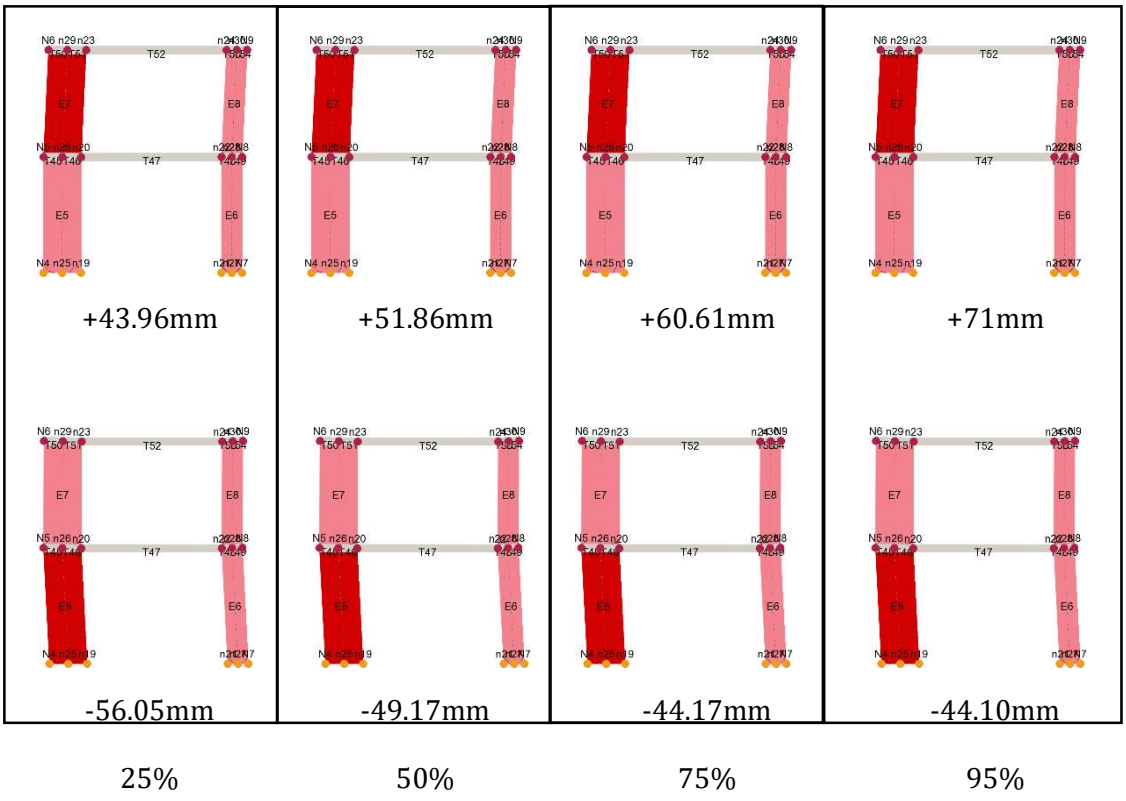

Figure 7.20 Failure pattern for the 3D models with different load distributed on piers

The model with an equal load distribution in X and Y direction offers the most accurate results in terms of lateral strength and ultimate displacement, even though the total base shear force is underestimated in negative direction with almost 30%. Since the structure is also symmetrical in these two directions, an equal load distribution between piers and transversal walls can be used a reasonable assumption for the real load distribution. Therefore, this load distribution is used for the following analyses.

7.2.3 Flange effect

The influence of the transversal walls on the overall capacity of the structures can be also justified by comparing the pushover curves between a three-dimensional model and a two-dimensional model.

First, a simple 2D model in which the transversal walls are considered completely decoupled from the structure (2D model with no flange effect) is analyzed. By comparing the results of the two models, it can be observed that the capacity of the 2D Model is highly underestimated, especially in positive direction (Figure 7.21). The difference in the capacity curves of the 2D and 3D model is substantial and can explained by the influence that the transversal walls have on the axial force distribution in the piers in the 3D model.

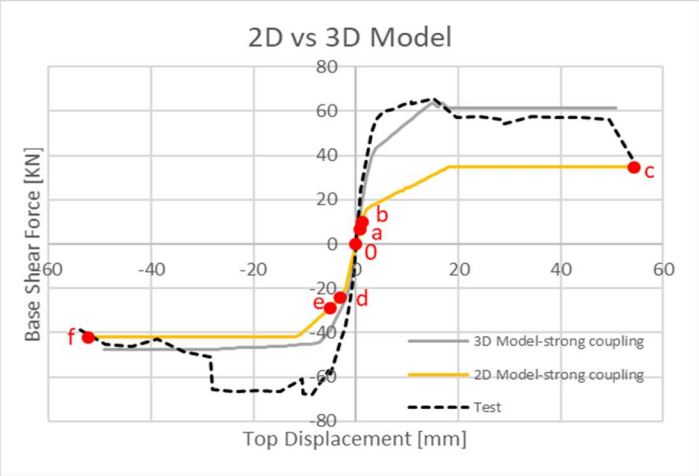

Figure 7.21 Pushover curve comparison between the 2D and 3D models

As mentioned before, the transversal walls are carrying a substantial load which is redistributed to the piers during the pushover analysis. The redistribution of forces affects the bending and toe crushing capacity of the piers and thus the global capacity of the structure is influenced. When these walls are not modelled, the force redistribution only happens between the piers in the façade and no significant increase in the axial force is observed in the piers.

The force redistribution and the impact that the transversal walls have on the axial force in the piers are illustrated in Figure 7.22. It can be observed, that apart from the peak value of the axial force that occurs in the 3D model due to the redistribution of forces from the transversal walls to the adjacent piers, the axial force distribution follows the same pattern for both models. For the positive direction of loading, the piers located on the east side are subjected to an increase in axial load (E6 and E8), while the piers located on the west side (E5 and E7) are subjected to a decrease in axial loads (Figure 7.22, b). This change occurs due to the overturning moment, when the piers located on the compression side of the structure experience an increase in axial load, while the piers from the tension side of the structure have lower axial loads. The same thing happens when the structure is loaded in negative direction (Figure 7.22, a). The piers located on the compression side of the structure (E5 and E7) are subjected to an increase in axial load, while the piers located on the tension side of the structure are subjected to a decrease in axial load.

In the 3D model, the influence of the transversal walls is taken into account and thus the variation of the axial load is not as straightforward as it is in a 2D model, but depends on the force transfers

between the transversal walls and the piers. The internal force distribution in the structure is also affected by the link between the piers in the façade in X direction.

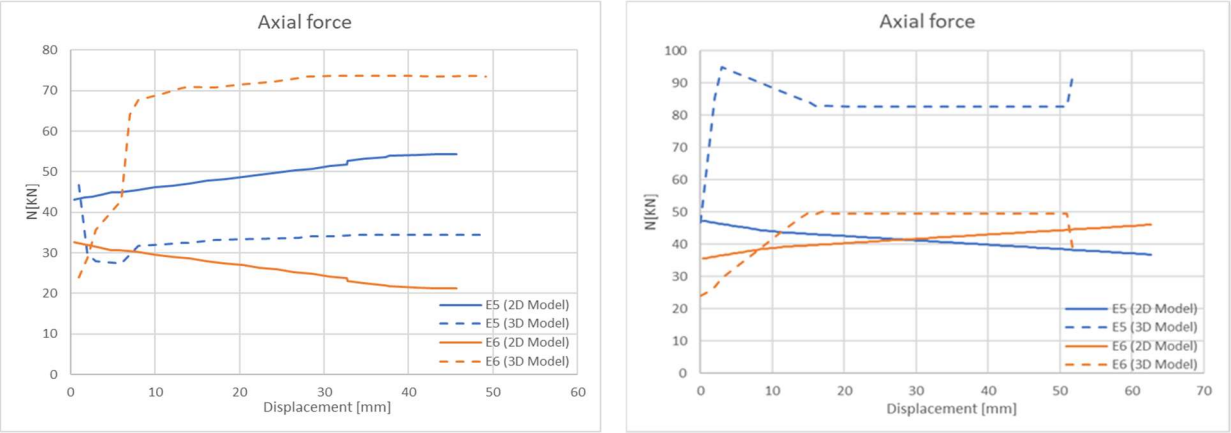

Figure 7.22 Axial force distribution in the ground floor piers: (a) negative direction and (b) positive direction;

The failure progression is also different for the 2D model. The top piers are first subjected to bending damage, followed by the wide pier at the ground floor (E5) and the short pier at the ground floor-E6 (Figure 7.23).

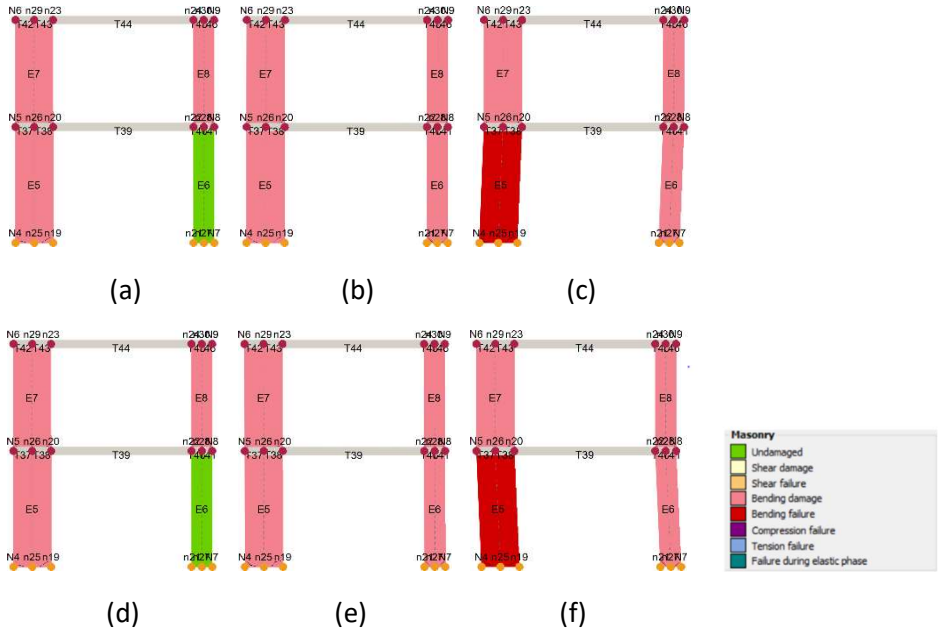

Figure 7.23 Failure progression of the 2D model

The bending damage occurs when the bending moment in the element exceeds the bending moment capacity of the element. Table 7.20 illustrates the value of the bending capacity of the top piers before failure.

Table 7.20 Bending capacity of top piers before failure

Element	Global Displacement (mm)	Axial force (N)	Bending capacity (KNm)
E8	0.77	21.00	3.02
E7	0.77	15	7.76

However, even though the piers located at the first floor are subjected to bending damage, the structure does not reach failure until the maximum drifts limits are exceeded. The bending capacity of the piers located at the first floor are exceeded at very low values of the global displacement, but due to redistribution of the axial force during the analysis, the bending capacity of the piers changes and slightly increases at later stages of the analysis (Figure 7.24).

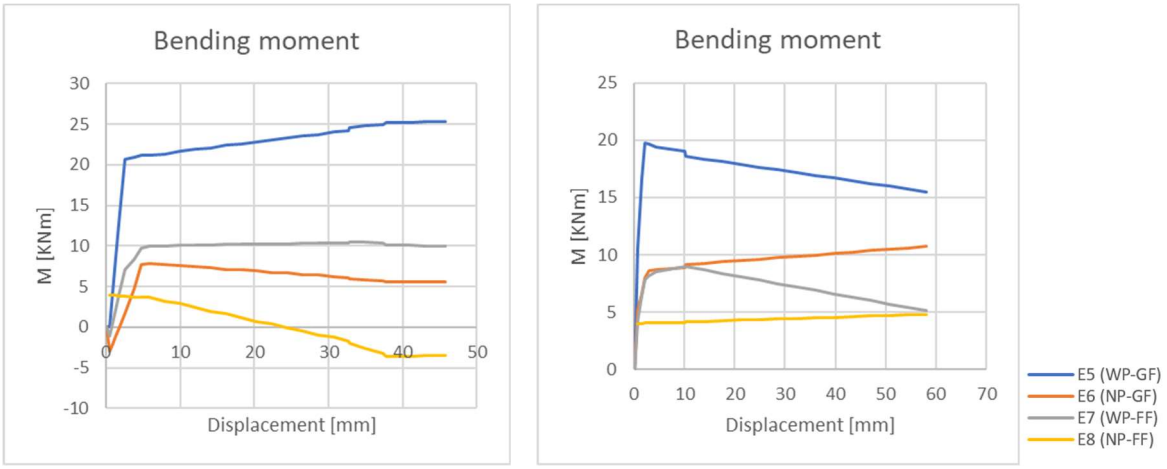

(a) *(b)*

Figure 7.24 Bending moment distribution for the 2D model: (a) -X and (b) +X

In this simple 2D model analysis in 3Muri, a conservative assumption was considered and the behavior of the piers in the façade and the transversal walls was modelled as completely decoupled.

Nevertheless, the experimental results show that transversal walls have a certain influence on the overall behavior of the structure and thus the flange effect must be taken into account in these analyses. When the structure is subjected to lateral loading, diagonal cracks occur in the out-of-plane walls, due to the deformation compatibility with the adjoining piers. If the cracks become large enough, it can be assumed that the dislocated part of the wall is not able to withstand any more loads and the corresponding loads are transferred to the adjoining piers (Figure 7.25, a). According to the recommendations provided by the NZSEE guidelines (NZSEE, 2016), the length of the transversal

wall that participates in the flange effect equals six times the width of the piers (600mm). In this study, the flange effect is quantified by additional gravity loads added to the piers, corresponding to the part of the transversal wall that takes part together with the in-plane piers in the lateral resisting system. These loads are expected to have an impact on the rocking and toe crushing capacity of the masonry panels. The flange effect results in an additional gravity load on the piers (Figure 7.25, b) ranging from 3.7KN for the narrow piers to 4.1KN for the wide piers.

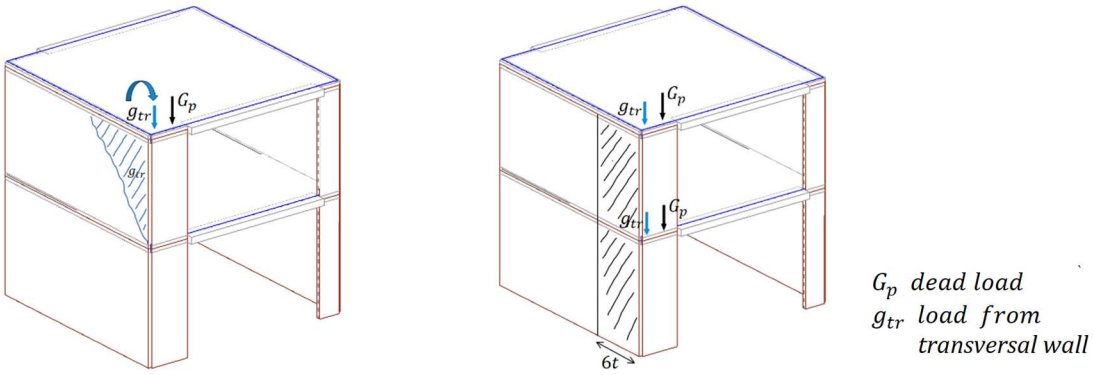

(a) (b)

Figure 7.25 *Flange dimension (a) and superimposed loads due to flange effect (b)*

For the 2D model with flange effect included, a similar model with the one considered in the previous sections is used. The model assumes an equal distribution of the gravitational load in X and Y direction. Only the piers in the façade are modelled according to their real dimensions and properties, while the transversal walls act as fictitious walls. These walls do not carry any gravity or lateral loads and their only role is to connect the piers located in the north and south façade.

The analysis of the 2D model when the flange effect is considered leads to an increase in the total base shear force, while for the ultimate displacement, no significant change occurs (Figure 7.26).

In the positive direction of loading, the maximum shear force reaches 48.59KN, which represents an increase of almost 24% when compared to the previous situation. In negative direction, the maximum shear force attains a value of 58.5KN, with almost 23% more than the model without the additional gravity loads due to the flange effect.

These results show an improvement from the previous 2D model with no flange included, when the piers and the transversal walls were considered completely decoupled. The lateral strength is still underestimated when compared to the test results, even though the displacement capacity is similar to the capacity observed in the test. The failure mechanism is, however, correctly identified, with the wide piers at the ground floor being the elements that dictate the failure of the entire structure (Figure 7.27).

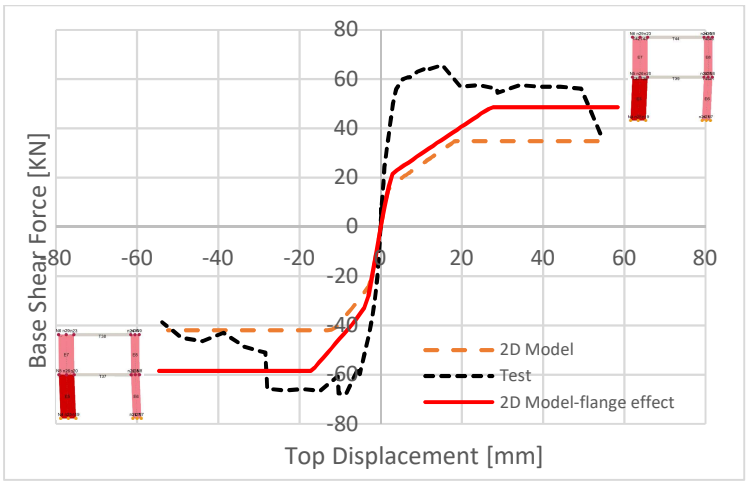

Figure 7.26 3Muri results for the 2D model (with flange effect)

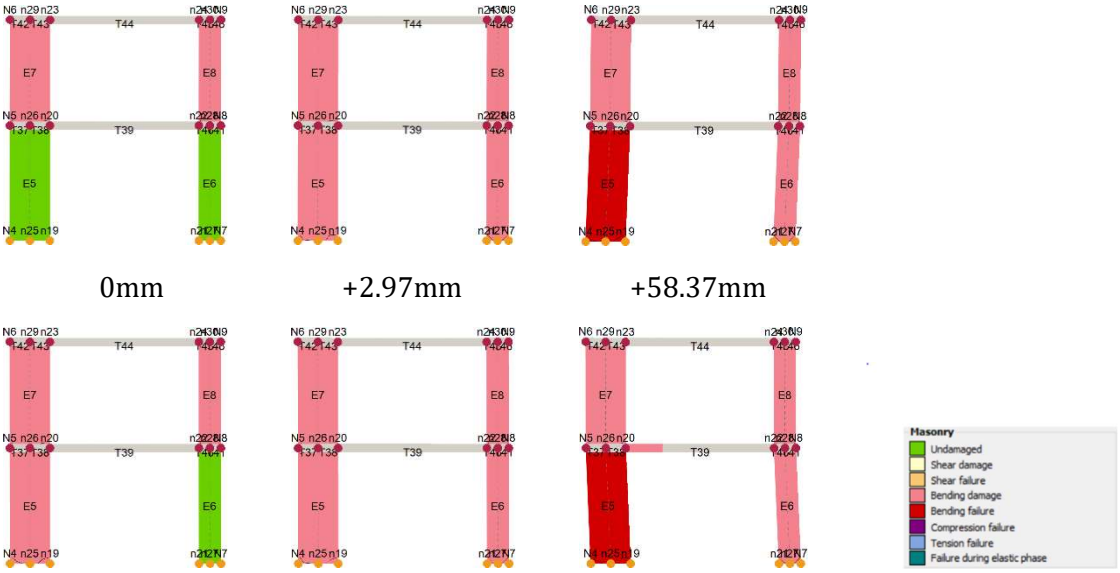

Figure 7.27 Failure progression of the 2D model with active flange

The flange effect and its consequence on the global structural behavior can be further analyzed by studying the influence of the length of the transversal wall active in the flange effect. So far, it was assumed, based on the NZSEE guidelines, that the portion of the wall that participates in the flange effect was equal to six times the width of the pier. By varying this length, a more comprehensive description of the structural behavior can be obtained.

Analyzing the capacity curves obtained of the models with different flange lengths (Figure 7.28), it can be concluded that there is a strong connection between the level of pier loading and the lateral capacity.

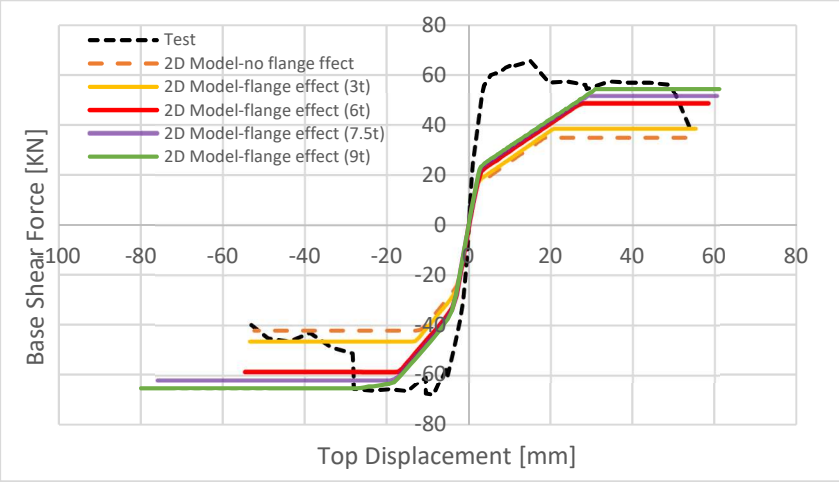

Figure 7.28 Capacity curves for different flange lengths

For limited dimensions of the flange length (from 300 to 750mm), the same failure mechanism occurs: in both direction of loading the wide pier located at the ground floor fails due to the exceedance of the drift limit (Figure 7.29, b). However, when the level of axial loads on the piers exceeds a certain level, in this case, due to the flange dimension increase, the failure mechanism changes in the negative direction, from the failure of the wide pier at the ground floor (E5), to the failure of the wide pier located at the first floor-E7 (Figure 7.29, a). Due to the increased axial force on the ground floor piers that also limit the lateral top displacement of the pier, the drift limit is first exceeded by the pier located at the first floor (7.29, a). This indicates that when the axial force in the piers reaches a certain value, the bending capacity changes and a different failure mechanism occurs in the structure.

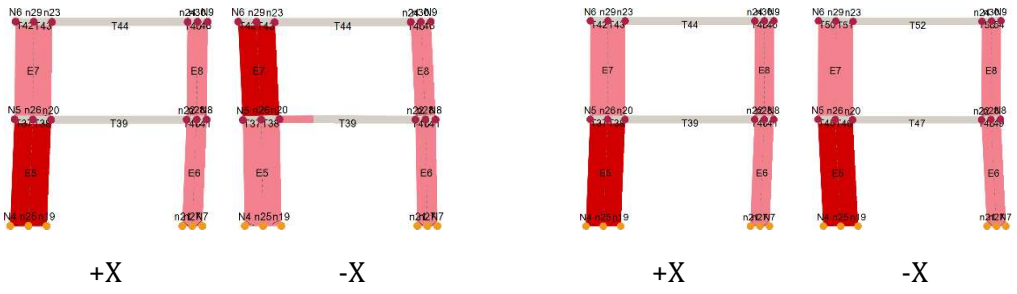

Figure 7.29 Failure mechanism in +X and -X: (a) 900mm flange; (b) 300/600/750mm flange

Table 7.21 Drift limits (flange length=900mm)

Direction	Element	H(mm)	u_i	u_j	φ_i	φ_i	Drift(%)	Drift limit EN(%)
positive	E5	2830	0	41.84	0	0	1.48	1.55
negative	E7	2600	41.84	78.51	0	0	1.41	1.42

An overview of the structural capacity and failure mechanism for each model with different flange dimension is presented in Table 7.22.

Table 7.22 Flange length variation

Model	Flange length[mm]	Direction	Base shear force [KN]	Top displacement [mm]	Failure mechanism
No flange effect	0	positive	36.68	54.42	Rocking-wide pier (ground floor)
		negative	41.97	52.35	Rocking-wide pier (ground floor)
Flange effect (3t)	300	positive	38.5	55.31	Rocking-wide pier (ground floor)
		negative	46.35	53.41	Rocking-wide pier (ground floor)
Flange effect (6t)	600	positive	48.59	58.37	Rocking-wide pier (ground floor)
		negative	58.5	56.6	Rocking-wide pier (ground floor)
Flange effect (7.5t)	750	positive	51.49	60.6	Rocking-wide pier (ground floor)
		negative	61.97	74.85	Rocking-wide pier (ground floor)
Flange effect (9t)	900	positive	54.38	61.23	Rocking-wide pier (ground floor)
		negative	65.42	78.97	Rocking-wide pier (top floor)

It can be observed that when the flange effect is included in the analysis, the model with a flange length of 600mm, as suggested by the NZSEE guidelines, is the model that provides the most accurate results. The failure mode is correctly identified in both direction of loading, while the ultimate displacement is comparable to the values observed in the test. In accordance with all the other result presented in the previous sections, the lateral strength is again slightly underestimated in both loading directions.

When the flange is smaller than 600mm, the results are similar to the results of the model with no flange effect included. If the flange has a length of more than 600mm, then the additional gravity loads acting on the piers are increased, which in turn leads to an increase of the structural capacity of the piers and consequently the global capacity of the structure is improved. However, for these models, even though the total base shear force is not significantly increased, the lateral displacement becomes highly overestimated, which places the results of these models on the unsafe side and thus making them unusable for the prediction of the structural capacity of the masonry building.

8 Simplified Lateral Mechanism Analysis ("SLaMA" method)

8.1 Method description

The lateral strength and displacement capacity can also be determined by using nonlinear assessment procedures with simple analysis techniques, as suggested by NZSEE guidelines (NZSEE, 2016). One of the recommended analysis technique is the Simplified Lateral Mechanism Analysis ("SLaMA") which can be completed before the 3D modelling and can be used as a first step of the structural assessment. This method can provide an insight in the evolution of the probable deformation mechanism and can be used to determine the global lateral strength and deformation capacity of the structure.

According to the NZSEE guideline (NZSEE, 2016), the SLaMA method is a " simple nonlinear analysis technique that provides an estimate of the global probable capacity of the primary lateral structure of the building as the summation of the probable capacities of the individual mechanisms systems" and "it enables assessors to investigate (and present in a simple form) the potential contribution and interaction of a number of structural elements and their likely effect on the building's global capacity".

The key steps of the analysis, according to the NZSEE guideline are summarized below and a scheme of the procedure is illustrated in Figure 8.1:

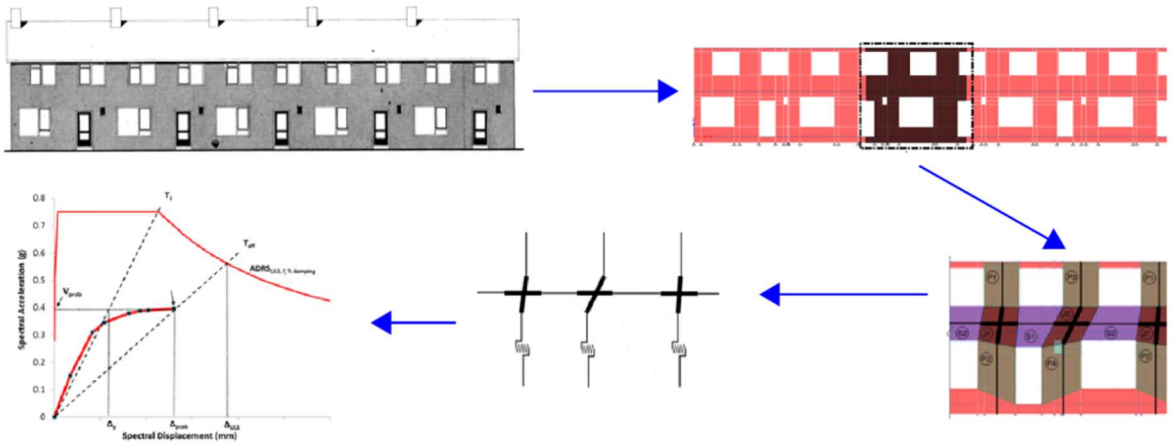

Figure 8.1 SLaMA Procedure (Muir et al., 2017)

Step 1 Identify the key structural elements and potential structural weaknesses.

Step 2 Based on an "equivalent frame analysis", the URM walls are subdivided into piers, spandrels and rigid nodes (Muir et al., 2017). The load path is identified, after which the probable strength and deformation capacities of the individual elements are calculated.

Step 3 Determine the probable failure mode by evaluating the hierarchy of strength of the structural elements.

Step 4 Compute the structural non-linear behavior of each critical structural element and extend local to global behavior.

Step 5 Study the potential global failure mechanism by combining various individual mechanisms and determine the lowest base shear force and displacement capacity.

Step 6 Determine the equivalent SDOF system and seismic demand.

This section presents the implementation of the SLaMA method on the calcium silicate element masonry assemblage. Further on, a comparison with the non-linear static pushover analysis will be performed.

Component capacity

The 3D model can be idealized by a 2D frame system (Figure 8.2) for which the capacity curve can be calculated following the step-by-step SLaMA method.

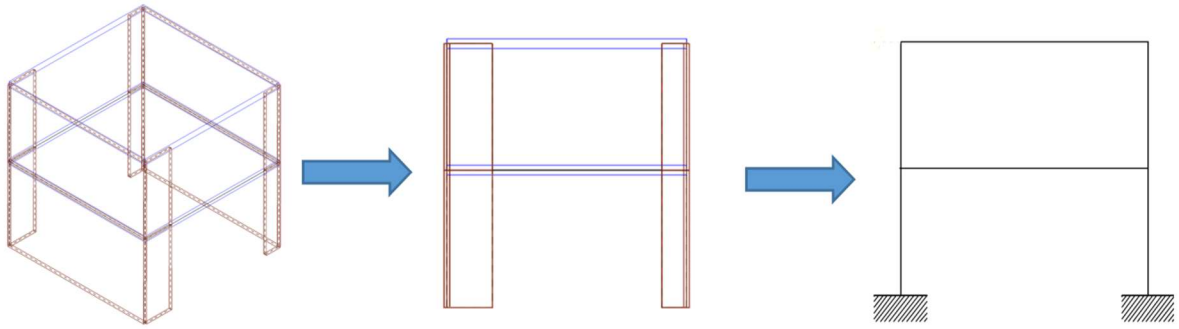

Figure 8.2 Frame idealization

The lateral capacity of URM piers can be calculated with reference to the analytical model proposed by Benedetti and Steli (Benedetti & Steli, 2008; Petry & Beyer, 2014). The model correlates the top displacement with the shear force and starts from the basic assumption of a no-tension material and the linear-elastic and non-linear domain.

Benedetti and Steli (Benedetti & Steli, 2008) propose the "yield" and "ultimate point" approach to estimate the displacement capacity. Based on this approach, the yield point is considered as the point in the non-linear elastic domain in which the stress in the base section equals the compression strength of the masonry (σ_{min}=-f_u). When the moment in the base section exceeds the yield moment, an elastic-ideal plastic material behavior is considered and some stress redistribution in the compressed zone is allowed. The deformation capacity is evaluated based on the yield and ultimate curvature of the structural elements. The yield moment M_y and ultimate moment M_u can be obtained with the following formulas (Petry & Beyer, 2014):

$$M_y = N\left(\frac{L}{2} - \frac{L_{c,y}}{3}\right) = \frac{L \cdot N}{2} - \frac{2N^2}{3T \cdot f_u} \tag{8.1}$$

$$M_u = N\left(\frac{L}{2} - 0.361 \cdot L_{c,u}\right) \tag{8.2}$$

$$L_{c,u} = \frac{1.5 \cdot N}{T \cdot f_u} \tag{8.3}$$

Where:

$L_{c,y}$ length of the compression zone at the yield point

$L_{c,u}$ length of the compression zone at the ultimate point

L length of the pier

T thickness of the pier

N Axial force

The yield curvature can be calculated with the following formula:

$$\chi_y = \frac{2N}{E \cdot T \cdot L_c^2} \tag{8.4}$$

$$\chi_y = \frac{2 \cdot \varepsilon_y}{L} \tag{8.5}$$

In an elastic-plastic model, the yield strain ε_y equals the ratio of the masonry strength to the elastic modulus (Benedetti & Steli, 2008):

$$\varepsilon_y = \frac{f_u}{E_m} \tag{8.6}$$

The curvature at ultimate point is given by the following formula:

$$\chi_u = \frac{\varepsilon_c}{L_{c,u}} \tag{8.7}$$

ε_c represents the maximum compression strain at the external fiber of masonry. Petry and Beyer (Petry & Beyer, 2014) propose an admissible compression strain of 0.4%. The plastic displacement becomes:

$$\Delta_p = \frac{1}{2}\left(\chi_u - \chi_y\right)\cdot h_p \cdot (H - h_p) \tag{8.8}$$

$$h_p = H\left(1 - \frac{M_y}{M_u}\right) \tag{8.9}$$

$$\Delta_u = \Delta_p + \Delta_y \tag{8.10}$$

Where:

h_p length of the plastic hinge

Δ_u ultimate displacement

These formulations are valid for a cantilever wall. For a fixed-fixed wall, the displacement at the top of the wall can be obtained by determining the displacement at half height of the pier and then doubling this value (Petry & Beyer, 2014).

According to the NZSEE guidelines (NZSEE, 2016), in order to assess pier capacities under lateral loading, the wall displacement at the yielding moment can be taken as the sum of the flexural and shear displacement. The displacement due to flexural and shear deformations can be computed as follows (Petry & Beyer, 2014):

$$\Delta_{fl} = V \cdot \frac{H^3}{2EI}\left(\alpha - \frac{1}{3}\right) \tag{8.11}$$

$$\Delta_{sh} = V \cdot \frac{5H}{6GA} \tag{8.12}$$

$$\Delta_y = \Delta_{fl} + \Delta_{sh} \tag{8.13}$$

H_o represents the shear span, and for a fixed-fixed wall H_0=0.5H and α=H0/H.

Petry and Beyer (2014) present another mechanical model proposed by Priestley et al. that estimates the displacement capacity. According to this model (Petry & Beyer, 2014; Priestley, Calvi, & Kowalsky, 2007), the plastic hinge corresponds to the remaining uncompressed length of the bottom section. The plastic hinge, ultimate moment and top displacement capacity are determined as follows:

$$\theta_p = \frac{\varepsilon_c}{L_{c,u}} \cdot \frac{L - L_{c,u}}{2} \tag{8.14}$$

$$M_u = N \cdot \left(\frac{L - C \cdot L_{c,u}}{2}\right) \tag{8.15}$$

$$L_{c,u} = \frac{N}{C^2 \cdot f_u \cdot T} \tag{8.16}$$

$$\Delta_u = \frac{\varepsilon_c}{L_{c,u}} \cdot \left(\frac{L - L_{c,u}}{2}\right) \cdot H \tag{8.17}$$

Lateral capacity

After the lateral strength and deformation of each component has been determined, the lateral capacity of the entire assembly can be assessed. According to the NZSEE (2016), the lateral capacity is calculated considering three possible failure mechanisms (Figure 8.3):

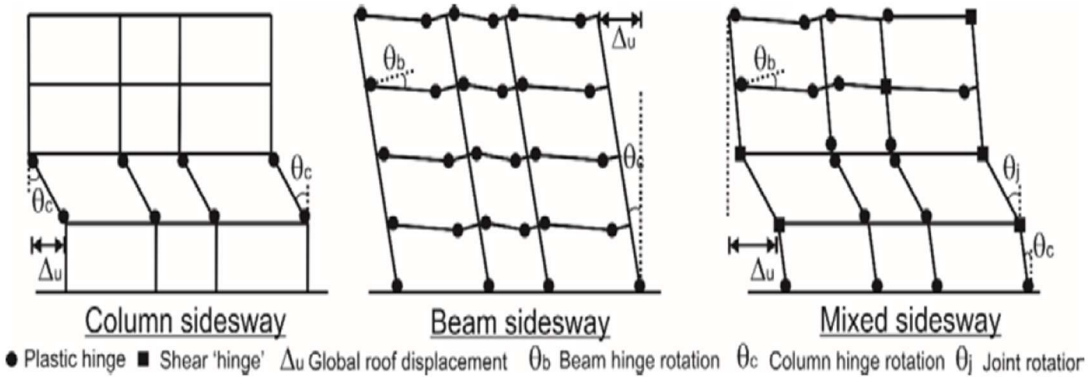

Figure 8.3 Possible plastic mechanisms of moment resisting frames (NZSEE, 2016)

However, since the geometry of the calcium silicate masonry assemblage does not include any additional horizontal structural elements, such as spandrels or beams, the failure mechanism of the structure in question can be reduced to a column sideways mechanism. In this case, the frame lateral capacity can be computed assuming a soft-storey mechanism at each level of the building. The weakest floor can be determined if the mechanism with the lowest base shear force is determined.

As presented by Del Vecchio et el. (Del Vecchio, Gentile, & Pampanin, 2017) the base shear force of the entire frame can be evaluated based on the following formulation:

$$V_{b,2} = \Sigma M_{col,base,i} / (0.5h) \tag{8.18}$$

Where:

$M_{col,base,i}$ represents the flexural capacity at the base and h represents the clear interstorey height of the floor.

The top displacement of the frame at the yield point and ultimate point of the nonlinear behavior of URM piers are computed based on the component drift calculated in the previous section.

Yielding displacement is computed based on the following formulation:

$$\Delta_y = \min(\theta_{y,col}) \cdot H_{eff} \tag{8.19}$$

Ultimate displacement is given by:

$$\Delta_u = \min(\theta_{u,col}) \cdot H_{eff} \tag{8.20}$$

For the column sideway mechanism, H_{eff} can be expressed as H_{eff}=0.5H, where H is the height of the frame.

The mechanism that involves the ground floor piers and the assumed displacement shape is illustrated in Figure 8.4. A similar procedure is adopted for the mechanism that involves the first-floor piers.

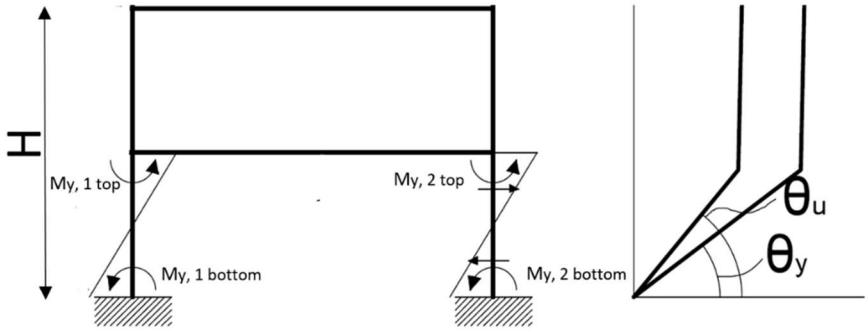

Figure 8.4 Sideway mechanism and assumed displacement shape

8.2 SLaMA approach for the in-plane loaded wall

When applying the previous formulation for the cantilever wall that was described in Section 6, a good agreement with the experimental test is obtained in terms of lateral strength capacity and ultimate displacement. Both the base shear force and the ultimate top displacement are correctly identified, as it can be observed in Figure 8.5.

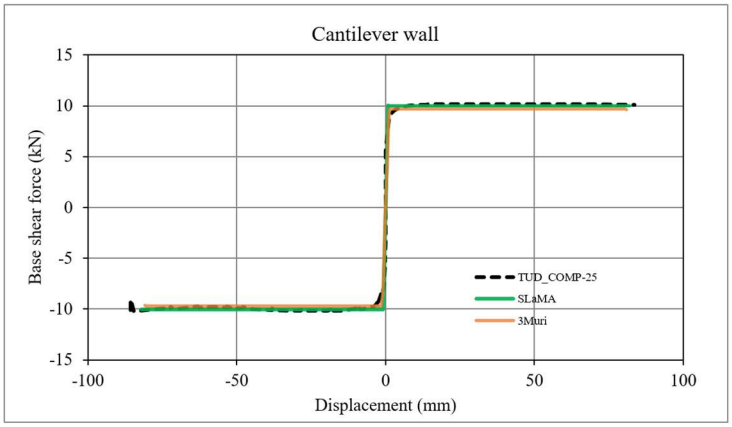

Figure 8.5 Capacity curve for a cantilever wall according to the simplified analytical method

However, the displacement capacity of the masonry panel depends on the model chosen for calculation. It can be observed in Table 8.2, that the ultimate displacement calculated based on the Benedetti and Steli formulation is highly underestimated, only 8mm, while the model developed by Priestley et al. (Petry & Beyer, 2014) offers a better estimate of the ultimate displacement, 82mm compared to the 83.67mm obtained in the test. The discrepancy occurs mainly due to the plastic hinge definition in the two models. However, even though the plastic hinge length is defined too simplistically by the Priestley et al. model, it seems to offer a more accurate estimation of the real value. A more detailed calculation of the pier capacity is included in Annex C.

Table 8.1: Predicted ultimate displacement for a cantilever wall

Parameter	Symbol	Units	Benedetti and Steli	Priestley et al
Compression length	$L_{c,u}$	m	0.066	0.061
Moment capacity	M_u	KNm	27.34	27.22
Ultimate curvature	χ_u	m^{-1}	0.061	0.066
Plastic hinge height	h_p	m	0.016	0.918
Plastic displacement	Δ_p	m	0.001	-
Ultimate displacement	Δ_u	m	0.008	0.082

8.3 SLaMA approach for the masonry assemblage

Based on the capacity calculation of the cantilever wall, the lateral strength and deformation capacity of the masonry panels of the URM house are computed in the following tables (Table 8.2, Table 8.3, Table 8.4). Since these masonry panels have a double fixed boundary condition, as mentioned before, the ultimate displacement of the piers is calculated at half height and the value obtained is doubled in order to obtain the displacement at the top of the pier (Petry & Beyer, 2014). For the following calculation, an equal load distribution in X and Y direction is assumed and the effect of the transversal walls is not taken into account, similar to the 2D numerical model with no flange effect included.

Table 8.2: Properties of URM piers

Parameter	Symbol	Units	Pier			
			WP-GF	NP-GF	WP-FF	NP-FF
Length	L	m	0.979	0.536	0.979	0.536
Thickness	T	m	0.1	0.1	0.1	0.1
Height	H	m	2.83	2.83	2.6	2.6
Axial load	N	KN	49	26	25	13.6
Compressive strength	fu	KN/m^2	13390	13390	13390	13390
Elasticity modulus	E	N/mm^2	9256	9256	9256	9256
Shear resistance	τ0	KN/m^2	830	830	830	830

Table 8.3: Flexural capacity of URM piers

Parameter	Symbol	Units	Pier			
			WP-GF	NP-GF	WP-FF	NP-FF
Yielding strain	ε_{cy}	-	0.0014	0.0014	0.0014	0.0014
Ultimate strain	ε_{cu}	-	0.0040	0.0040	0.0040	0.0040
Axial Load	N	KN	49	26	25	13.6
Yielding moment	M_y	KNm	22.79	6.63	11.93	3.55
Length of the compressed zone	$L_{c,u}$	m	0.055	0.029	0.028	0.015
Ultimate moment	M_u	KNm	23.01	6.69	11.98	3.57

Table 8.4: Drift capacity of URM piers

Parameter	Symbol	Units	Pier			
			WP-GF	NP-GF	WP-FF	NP-FF
Yielding curvature	χ_y	m^{-1}	0.00291	0.00532	0.00291	0.00532
Ultimate curvature	χ_u	m^{-1}	0.07287	0.13733	0.14283	0.26255
Shear span	H_0	m	1.42	1.42	1.30	1.30
Yielding displacement	Δ_y	m	0.0009	0.0015	0.0004	0.0007
Plastic length	h_p	m	0.014	0.013	0.006	0.006
Plastic displacement	Δ_p	m	0.0014	0.0025	0.0011	0.0021
Ultimate displacement [Benedetti and Steli]	Δ_u	m	0.0022	0.0040	0.0015	0.0028
Ultimate displacement [Priestley &all]	Δ_u	m	0.05205	0.05380	0.09590	0.09653
Yield drift	θ_y	rad	0.00062	0.00106	0.00030	0.00052
Ultimate drift [Benedetti and Steli]	θ_u	rad	0.00158	0.00281	0.00118	0.00213
Ultimate drift [Priestley &all]	θ_u	rad	0.01833	0.01894	0.03688	0.03713

It is worth noting that the bending capacity prediction of the individual piers in this case is similar to the bending capacity calculated according to the empirical formulations described in literature and international codes (Section 4).

The predicted ultimate displacement, however, is highly underestimated, especially for the model proposed by Benedetti and Steli (Table 8.4). The difference is mainly related to the definition of the yield point. Considering the yield point as the point where the stress reaches the compression strength of the masonry (σ_{min}=-f_u) can lead to an underestimation of the deformation capacity. Petry and Beyer (Petry & Beyer, 2014) were able to determine based on experimental findings that when the admissible stress is determined in such way that the yield point and the first crack in bricks occur at the same time, a more accurate prediction of the force-displacement relation of URM piers can be obtained.

The model proposed by Priestley et al. seems to yield a better estimation of the ultimate displacement. However, Petry and Beyer noticed that even though the model proposed by Priestley et al (Petry & Beyer, 2014; Priestley et al., 2007) offer a more accurate result, the approximation of the plastic length might be too simplistic.

The results of the SLaMA method for the URM house can be visualized in Figure 8.6 and 8.7. Figure 8.6 show the difference between the two models proposed by Benedetti and Steli and Priestley et. al in terms of ultimate displacement. As mentioned before, it can be observed that the latter model offers the better estimation for the ultimate top displacement.

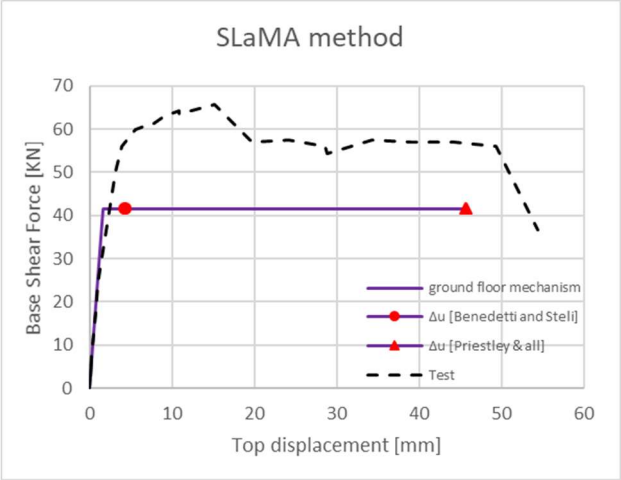

Figure 8.6 Capacity curve of the structure when the ground floor mechanism occurs

When analyzing the pushover curve, it can be observed that the lowest base shear force is given by the mechanism that involves the ground floor piers (Figure 8.7), which means that the weakest floor is the ground floor of the structure and failure will be concentrated at this level. The base shear force for the top floor mechanism is 69.17 KN, while the ground floor mechanism gives a base shear force of 41.59 KN. As a consequence, the ground floor mechanism becomes the governing failure mechanism and the base shear failure associated to this failure mode defines the lateral capacity of the structure.

The ground floor mechanism is also more similar to the real behavior of the house and offers a better estimate of the ultimate displacement, even though the lateral strength is underestimated. This result shows that the failure of the structure cannot be solely based on the exceedance of the bending capacity of a single structural element. Due to force redistribution that takes place between structural elements, a higher base shear force can be expected.

The top floor mechanism leads to an unrealistically high ultimate top displacement and a maximum drift of 3.84% for the top piers, that exceeds both the drift limit observed in the experiment and the drift limit defined by the Eurocode. The large top displacement in this case is also an indication that a failure mechanism at this location is unlikely.

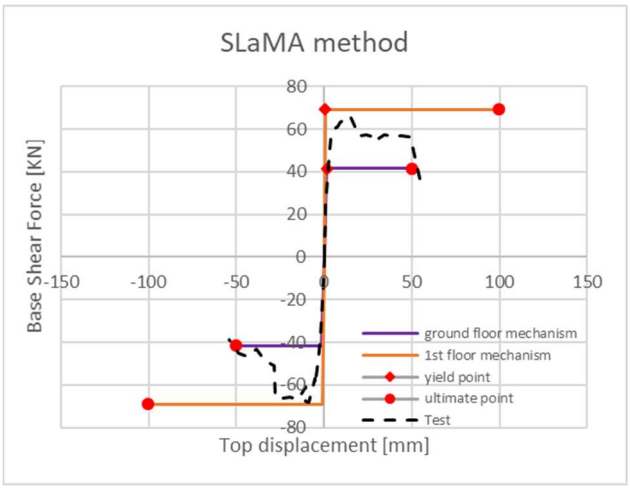

Figure 8.7 Capacity curve of the structure for different failure mechanisms

Similar with the analysis of the 2D model, the analytical calculation based on the SLaMA method also shows an improvement in the structural capacity of the building when the flange is taken into account.

As it can be observed in Figure 8.8, the analytical model that includes the flange effect leads to an increase in the total base shear force when compared with the first initial assumption. The base shear force increases with almost 30% for the ground floor mechanism, while the ultimate displacement is smaller than the displacement of the model that does not consider the flange to play an active part in the global behavior. Similar with the results of the numerical 2D model, the flange effect plays an important role in the overall capacity of the structure, due to the additional loads that it imposes on the piers.

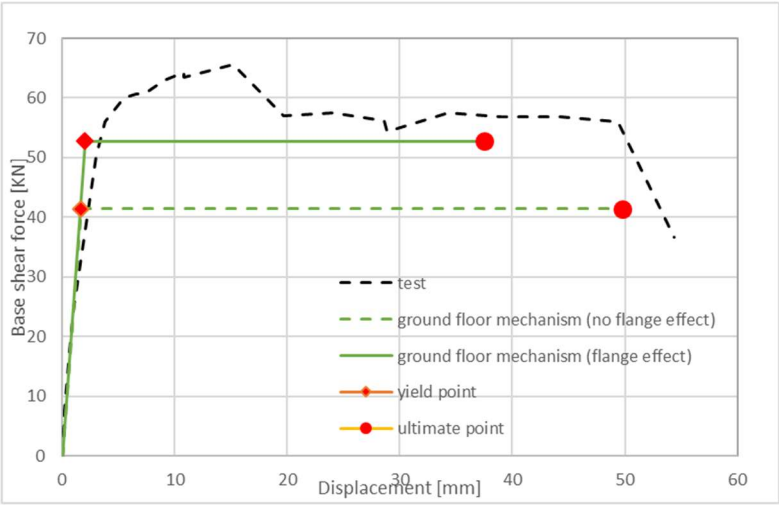

Figure 8.8 Capacity curve according to SLaMA method when the flange effect is considered

A higher level of axial force on the piers due to the superimposed loads from the flange reduces the top displacement of the structure. These additional loads also decrease the drift limit of the individual piers and the results obtained are more similar to the real values obtained in the test (Table 8.5).

Table 8.5 Maximum drift comparison

Model	Parameter	Units	Pier			
			WP-GF	NP-GF	WP-FF	NP-FF
No flange effect	Drift θ_u	rad	0.0183	0.0189	0.0368	0.0371
Flange effect included	Drift θ_u	rad	0.0140	0.0130	0.0283	0.0239

The SLaMA method offers a conservative prediction of the deformation capacity because it assumes that the failure of all piers of one floor occurs at the same value of the global displacement. No force redistribution between the structural elements is considered and thus the structural response is limited.

8.4 Comparison with numerical and experimental results

For the 2D model, in which only the structural elements in the façade are modelled, the analytical calculation based on the SLaMA method seems to offer a good indication of the most vulnerable elements in the structure that can limit the global lateral capacity.

In the numerical model, when the effect of the flange is not considered, the elements subjected to damage are correctly identified, the ultimate displacement has a similar value, but the lateral capacity is underestimated with almost 42%. When the flange effect is considered, better results are obtained, both in terms of lateral displacement and total base shear force, as it was demonstrated by the previous analyses (Figure 8.9).

Similar to the numerical model, when the flange effect is included in the analytical calculation of the 2D model ("SLaMA" method), the predicted pushover curve of the masonry assemblage matches to a certain degree the real capacity curve of the structure and the location of the failure mechanism is correctly identified. The lowest base shear force is obtained when the failure of the piers at the ground floor is considered and has a value of 52.70KN. This value of the base shear force is similar with the one determined by the EF model, when a value of 48.58KN was determined in positive direction and a value of 58.5KN was found in negative direction. These results represent an underestimation of the real base shear force, confirming the idea that the structure does not reach failure when the bending capacity of only one pier is exceeded. The lateral load can still be carried by the other piers located at the ground floor until the bending drift limit is again exceeded or when the piers collapse.

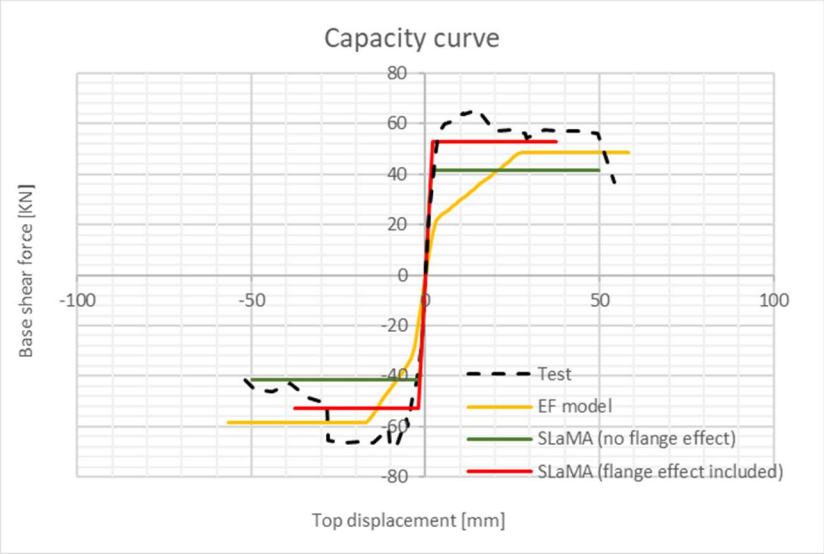

Figure 8.9 Capacity curves comparison between the 2D models

All the previous results further prove that the flange effect of the transversal walls on the overall lateral capacity of a two-dimensional model cannot be ignored, regardless the modelling technique and the analysis approach chosen. However, it is important that during the modelling process, the active part of the transversal wall in the flange effect is correctly identified.

9 Conclusions

In this thesis work the performance of the equivalent frame (EF) modelling approach in predicting the nonlinear response of unreinforced masonry structure was evaluated. The model was applied in the case of typical Dutch modern terraced houses made of calcium silicate element masonry. The model calibration and validation made use of the experimental results obtained during the large-scale tests on components and assembled structure performed at TU Delft in 2016/2017.

As a first step, the model was calibrated to simulate the in-plane response of single walls. This calibration is of importance because in the EF approach the response of a building is based on the single response of vertical and horizontal elements, which are idealized as beam elements. In the simulation of the in-plane walls, a good correlation between the numerical results and the experimental ones was obtained. The outcome of the non-linear analysis of the EF model agreed with the experimental results: rocking failure was identified as the critical failure mode, while the lateral strength and drift capacity had similar values. The results also revealed that one of the most important modelling parameters was the strength criterion used for the definition of the shear failure mechanism. The Turnsek/Cacovic criterion describes a type of diagonal shear failure that is recommended to be used for existing walls, while the Mohr-Coulomb criterion represents a type of sliding shear failure and it is recommended to be applied especially for new masonry walls. However, while the structure studied can be viewed as a new masonry structure, a Mohr-Coulomb strength criterion is not able to provide reliable results in this case, because it associates the shear failure with the sliding of the bed joint. Since the bed joint sliding depends on the value the friction coefficient and the software is not allowing the definition of this parameter, the results are computed based on the friction coefficient defined in the Eurocode and consequently assumed by the 3Muri software. This parameter is highly underestimated by the software and thus the ultimate shear force computed based on the Mohr-Coulomb criterion is underestimated, making the results of the analysis inaccurate. Therefore, a Turnsek/Cacovic strength criterion had be used instead, since this criterion is based on a diagonal shear failure mode and the results are not determined based on the friction coefficient, but depend only on the shear strength of the masonry. Furthermore, the use of the Turnsek/Cacovic criterion can also be justified by the actual failure mode that occurred in the real structure, where cracks started forming diagonally following the pattern of the bed joints.

The global structural behavior of the full-scale calcium silicate element masonry assemblage was determined based on the three-dimensional equivalent frame model. The EF model considers that the structural walls are represented by an idealized frame in which the walls are divided into main vertical structural elements (piers) and horizontal structural elements (spandrels); these elements are connected by rigid nodes. However, the studied structure does not have spandrels and for this reason, only vertical elements, namely piers, could be identified. The software did not consider the floor slab to be part of the frame action necessary for the analysis of the EF model, and thus additional horizontal elements that link the piers in the façade had to be included in the model.

A sensitivity study was performed to identify the influence of different modelling choices. The focus was on the level of coupling and interaction between the piers, on the load distribution between piers and on the contribution of the transversal walls to the in-plane capacity of piers. Both 3D models and 2D models were used. The input parameters as calibrated for the in-plane tests on walls were used.

For the structural assessment of the building, the capacity curves, the total base shear force, drift limits and failure mechanisms were determined and compared against the experimental results.

First, the coupling between the façade piers was studied with the use of a 3D model. Due to the absence of horizontal structural elements, the software was not able to automatically account for the coupling effect due to the presence of a stiff floor. In order to overcome this drawback, additional fictitious beam elements were included in the model. By varying the stiffness of the beam elements, different levels of coupling were studied. The coupling between the wide and narrow piers in the façade showed to have an influence on the global response of the building and the failure mechanism. The analysis proved that a weak coupling between the piers leads to an underestimation of the total base shear force and an overestimation of the displacement capacity. If a stronger coupling was considered, the structural behavior improved and a more realistic lateral force capacity was obtained, together with more accurate values for the ultimate displacement. However, even though the analysis of the model with strong coupling between piers offered quite satisfactory results in terms of lateral strength and maximum drifts, with only an underestimation of the total base shear force in the negative direction of loading, the failure mechanism was not correctly identified. In positive direction of loading, the failure occurred in the wide piers located at the first floor, as opposed to the failure of the wide pier located at the ground floor that occurred in the experiment.

The variation of the initial floor load distributed on the piers offered more indication regarding the structural behavior of the piers and of the three-dimensional structure. As expected, when the load distribution on the piers was increased, the lateral capacity of the structure increased, both in terms of total base shear force and ultimate displacement. This behavior was expected because the rocking behavior of the piers is influenced by the level of axial force acting on them. The best results were obtained considering a bidirectional floor slab.

The variation of normal force in the façade piers during the lateral loading highlighted an unrealistic uplifting of the floor in correspondence of the transversal walls, which was not observed in the experiment. In the 3D model, the entire load supported by the transversal walls was transferred to the piers once the transversal walls attained their maximum rotational capacity. When the structure was pushed in one direction, extensive cracking occurred in the transversal walls due to deformation compatibility with the adjacent piers and the software considered the transversal wall to be completely dislocated from the structure and thus the forces corresponding to these walls were redistributed to other structural elements.

In order to avoid the undesired uplifting of the floor, a 2D modelling approach was chosen. In this approach the transversal walls were replaced by fictitious walls with no stiffness. The results were underestimated in terms of lateral strength, while the ultimate displacement and failure mechanism were correctly identified. This prompted to the influence of transversal walls on both capacity and failure mode. In comparison to the 3D modelling approach, the 2D modelling approach showed similar ultimate displacement and a reduction in force capacity.

To account for the contribution of the transversal walls to the in-plane behavior of the piers in the façade (flange effect), a 2D modelling approach partially considering the weight of the transversal walls as vertical load was adopted. The results showed an improvement in terms of total base shear force and a correct estimation of the critical failure mechanism. This result was expected, since the influence of the transversal walls, as it was considered by the software in the 3D model, had been

excluded. Increasing the flange length, lead to a higher axial force applied the piers, which in turn, affected the rocking capacity of the piers and improved the lateral response of the structure. However, by increasing the flange length too much, the displacement capacity became highly overestimated and it was concluded that the best approximation of the experimental results was obtained by considering a flange length equal to 6 times the thickness of the adjacent pier.

Additional analytical calculations were performed to confirm the numerical results obtained from the simplified model. For the analytical calculation, the Simplified Lateral Mechanism Analysis ("SLaMA") approach was implemented. This method can determine the probable contribution of the main structural elements on the global structural response. If for the in-plane loaded walls the analytical calculations were able to provide the same results as the numerical analysis, given the fact that they are based on the same formulations, for the masonry house, the analytical calculation offered slightly different results, which represented an underestimation of the real capacity of the structure.

A summary of these results can be visualized in Figure 9.1 and Table 9.1.

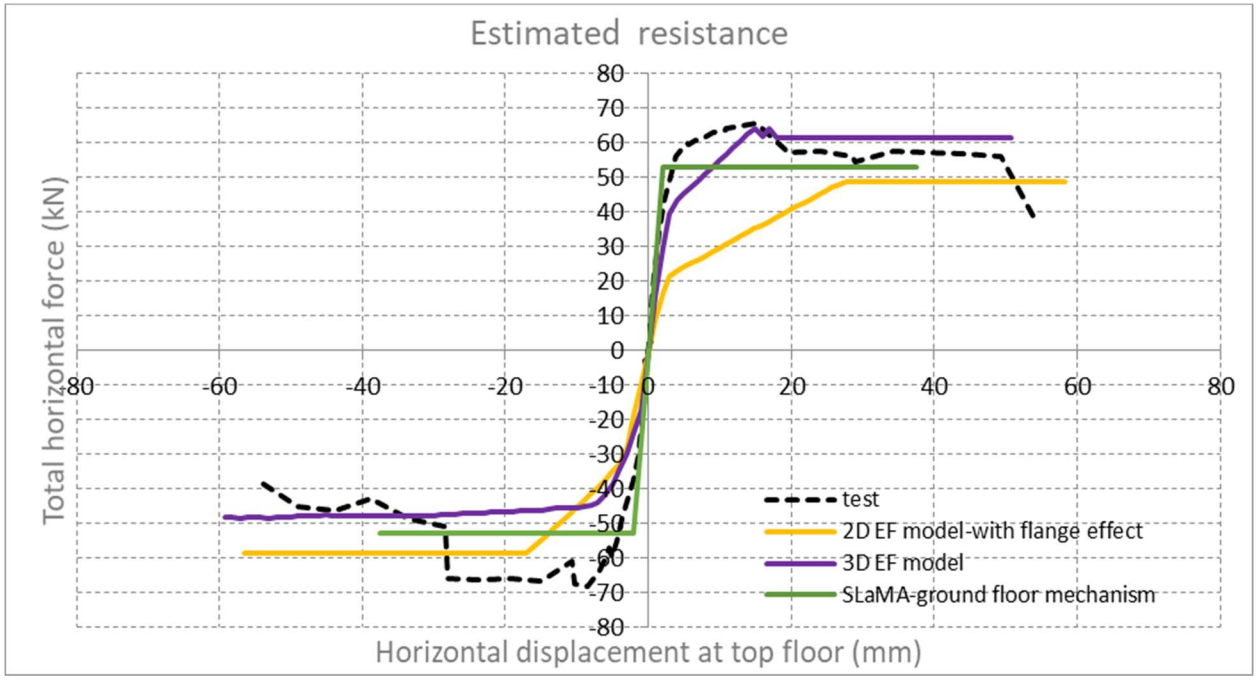

Figure 9.1 Pushover curve comparison

By comparing the different numerical and analytical results, it can be concluded that the 2D Model accounting for the flange effect offers the most realistic results for the structural behavior in terms displacement capacity and failure mode; an underestimation of the force capacity is obtained. It should be noted that the numerical results are obtained by considering only monotonic loading. The SlaMA approach can also be used as a good indication of the most probable failure mechanism, even

though the lateral force capacity is underestimated. It should be remarked that the experimental, numerical and analytical approach only investigate the in-plane failure of the façades piers, discharging possible out-of-plane failure of the transversal walls.

Table 9.1 Maximum base shear force and failure mechanism of the structure

Approach	Direction	Base shear(KN)	Ultimate displacement(mm)	Drift (%)	Failure mode
Experiment	positive	65.7	54.41	1.8	Rocking of the wide pier-ground floor
	negative	68.5	53.81	1.7	Rocking of the wide pier-ground floor
3D EFM	positive	63.95	51.82	1.72	Rocking of the wide pier (top floor)
	negative	47.61	49.17	1.53	Rocking of the wide pier (ground floor)
2D EFM-with flange effect	positive	48.58	58.37	1.52	Rocking of the wide pier (ground floor)
	negative	58.5	56.6	1.52	Rocking of the wide pier (ground floor)
2D SLaMA method-with flange effect	positive	52.70	37.51	1.3	Rocking of all piers (ground floor)
	negative	52.70	37.51	1.3	Rocking of all piers (ground floor)

Although the conclusions here presented are valid only for this selected case study, which presents a simple geometry, it is important to notice that the absence of horizontal elements leads to an increased effort of the user in the definition of the model. The studies presented in the literature study in Section 3 show a better agreement between the equivalent frame modelling approach and the experimental results for other types of structures, where both horizontal and vertical elements are present. This proves that more accurate results can be obtained when a more complex structure is analyzed, in which all the important structural elements can be properly modelled and the global failure can be controlled by more elements. In this case study, the structure has a simple geometry and the failure can only be controlled by the eight piers in the façade. Moreover, given that the floor not considered as a horizontal element which can transfer load between the façade piers, fictitious beams must be inserted in the model to ensure the coupling of the piers in the façade. The selection of the stiffness of these beam elements is of importance, because it controls the level of coupling between the piers. This parameter has a great influence on the global structural behavior and failure mechanism.

For future developments of the EF model, it is recommended to allow the modelling of the flange effect. This effect is of primary importance when the behavior of the structure is primary governed by the in-plane failure of piers.

Additionally, the possibility of computing the out-of-plane failure is of importance. Being the out-of-plane failure a brittle undesired mechanism, its occurrence is generally prevented and the capacity of the structure is evaluated as governed by the in-plane mechanism. This assumption is at the base of EF models leading to a post-verification of the out-of-plane failure mechanisms. The possibility of computing both the in-plane and the out-of-plane failure of the structure will improve the capability of the EF models.

Moreover, it is recommended that future research focuses on the applicability of the EF approach on other types of masonry structures. This thesis only focused on the assessment of a typical Dutch unreinforced masonry building, with a simple geometry and large openings in the façade. To obtain a more exhaustive conclusion on the ability of the EF model approach to predict the structural response of unreinforced masonry buildings, different types of structures have to be evaluated using the same approach. The results of one single analysis cannot serve as the basis of assessing the response of the unreinforced masonry structures in seismic conditions, since the problem is complex and requires a more in-depth investigation.

Appendix A Internal force distribution in the 3D model

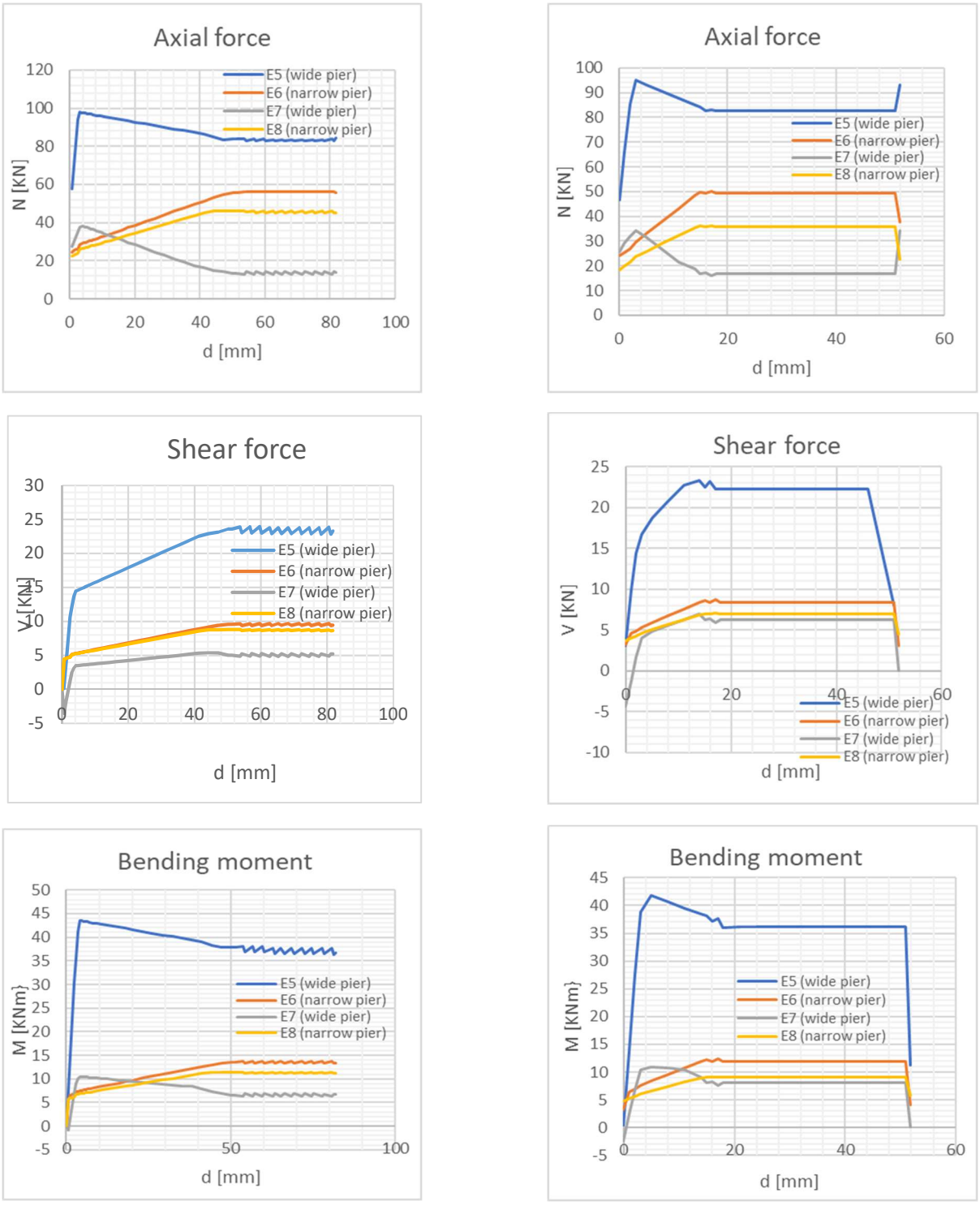

(a) *(b)*

Figure A. 1 Internal forces of piers in positive direction: (a) weak coupling; (b) strong coupling

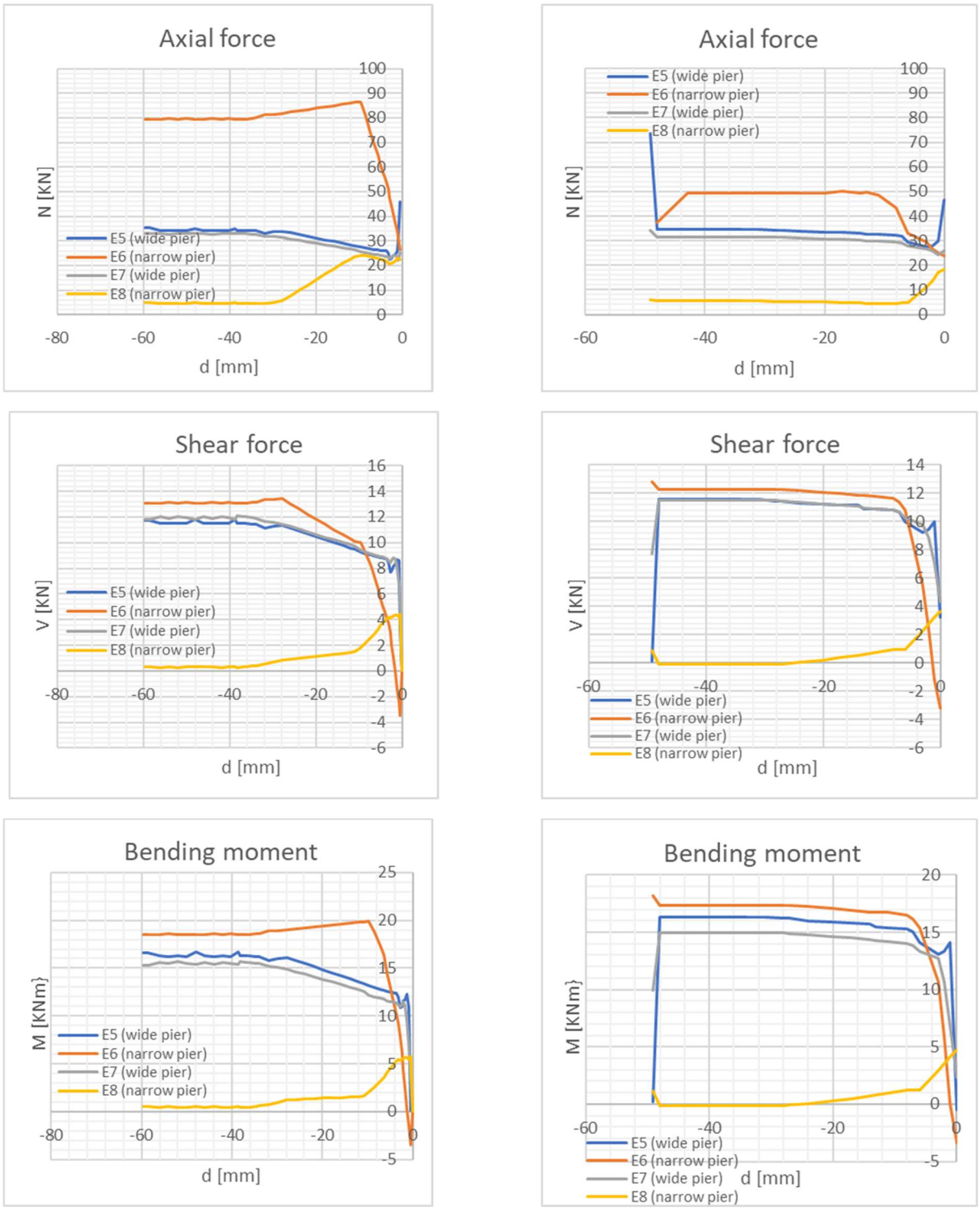

(a) (b)

Figure A. 2 Internal forces of piers in negative direction: (a) weak coupling; (b) strong coupling

Appendix B Results of the 3D model analysis with different load distribution on the piers

Appendix B.1 Model with 95% load on piers

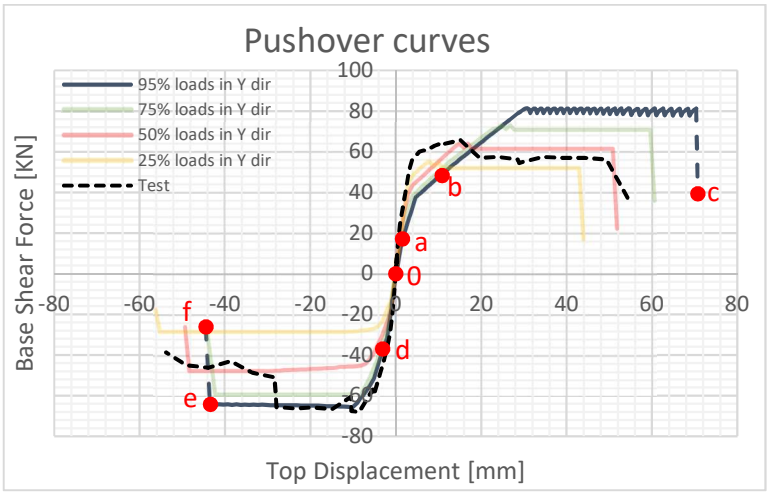

Figure B. 1 Pushover curve of the model with 95% load distribution on piers

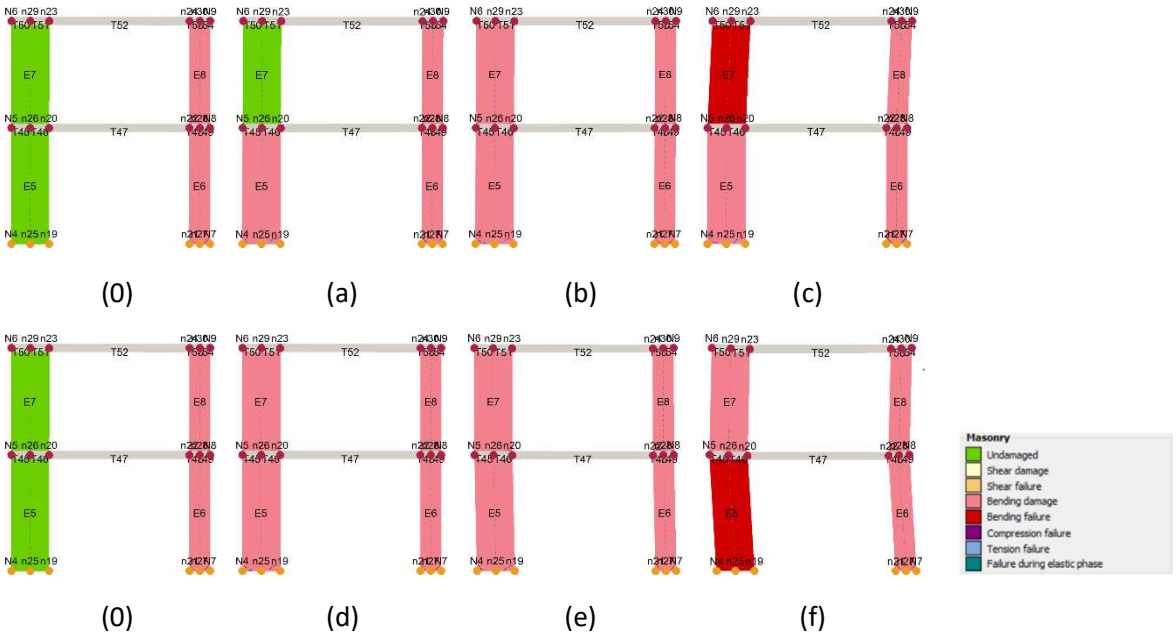

Figure B. 2 Failure progression for 95% load distribution on piers

Appendix B.2 Model with 75% load on piers

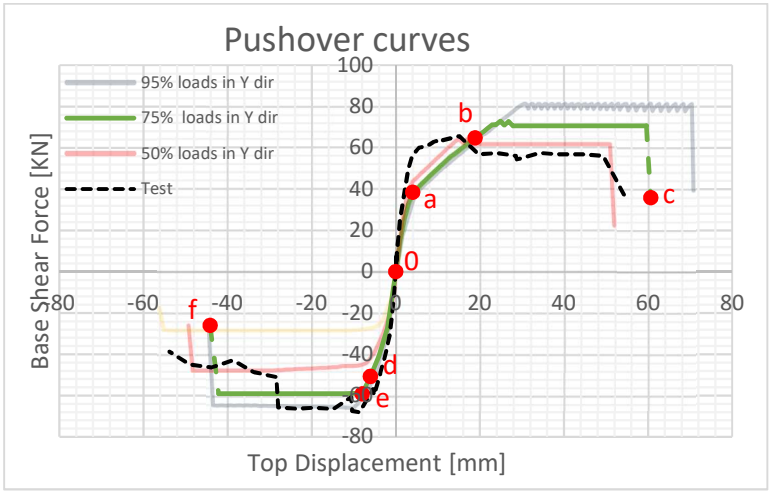

Figure B. 3 Pushover curve of the model with 75% load distribution on piers

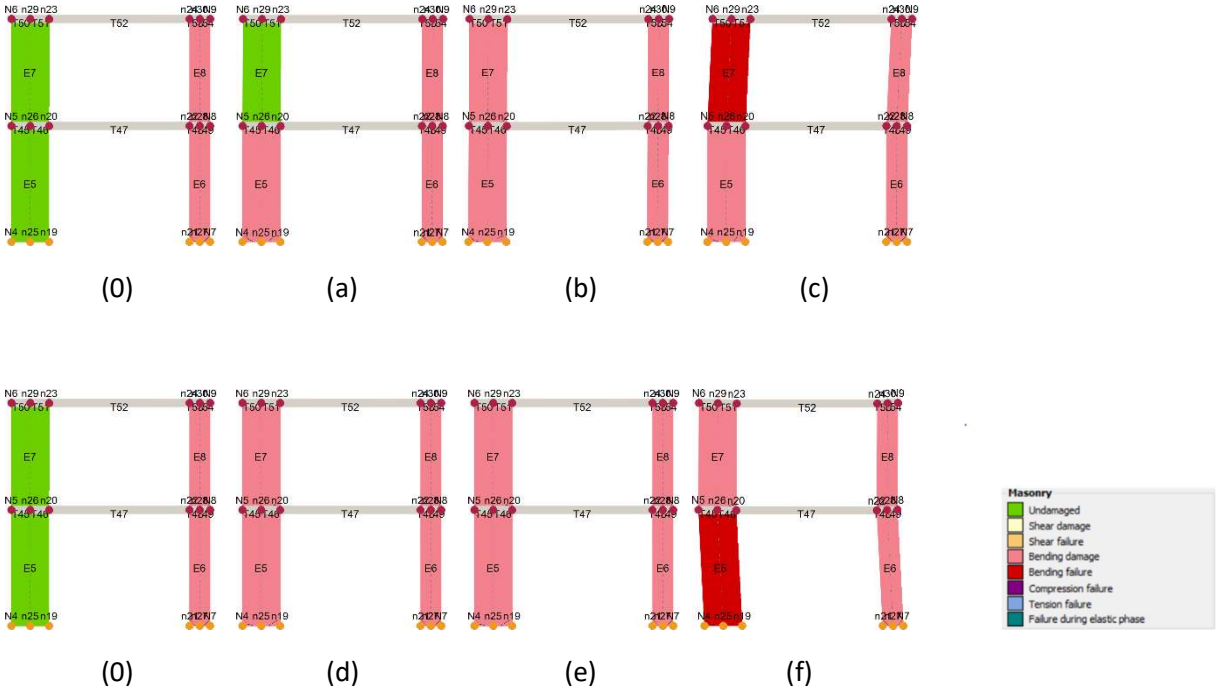

Figure B. 4 Failure progression for 75% load distribution on piers

Appendix B.3 Model with 50% load on piers

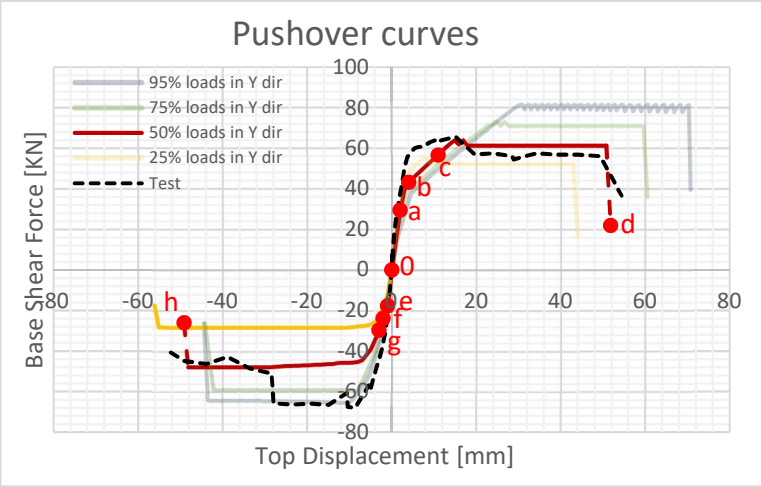

Figure B. 5 Pushover curve of the model with 50% load distribution on piers

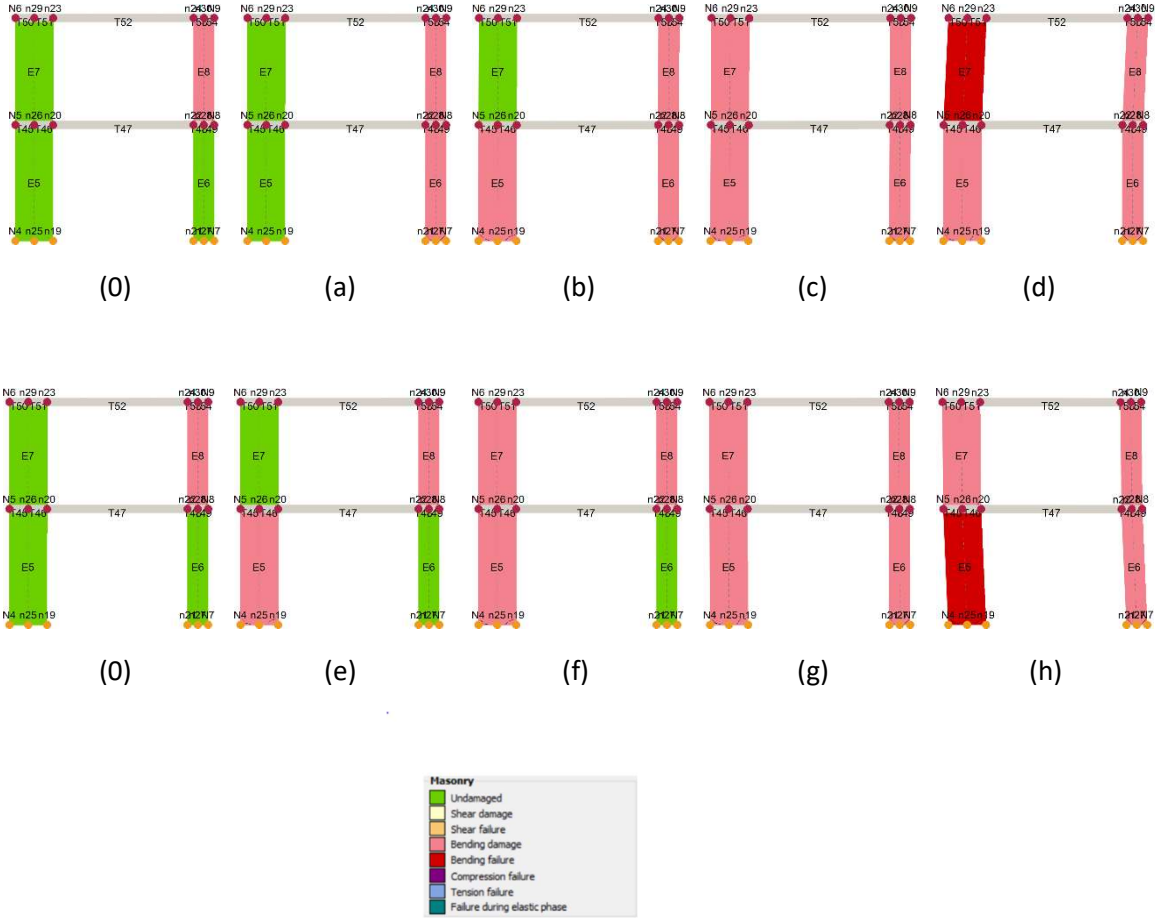

Figure B. 6 Failure progression for 50% load distribution on piers

Appendix B.4 Model with 25% load on piers

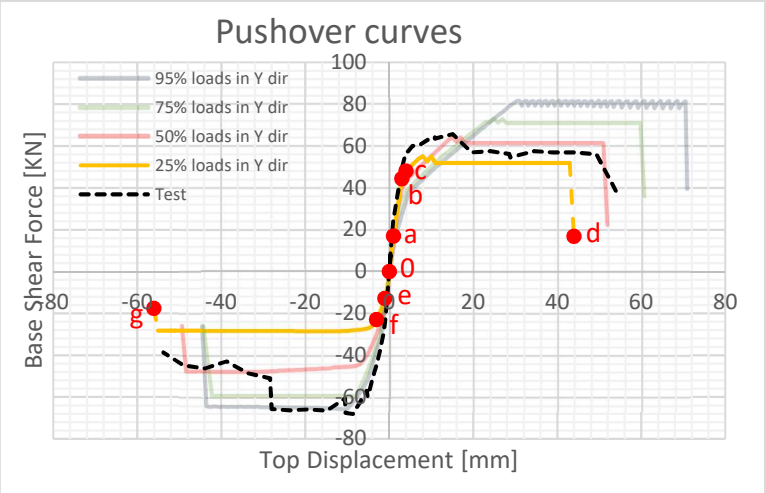

Figure B. 7 Pushover curve of the model with 25% load distribution on piers

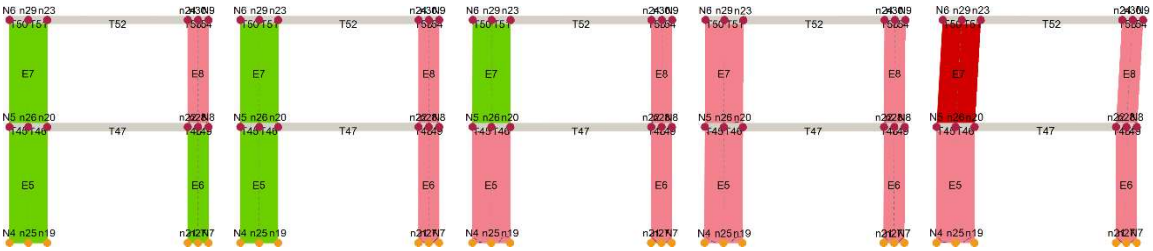

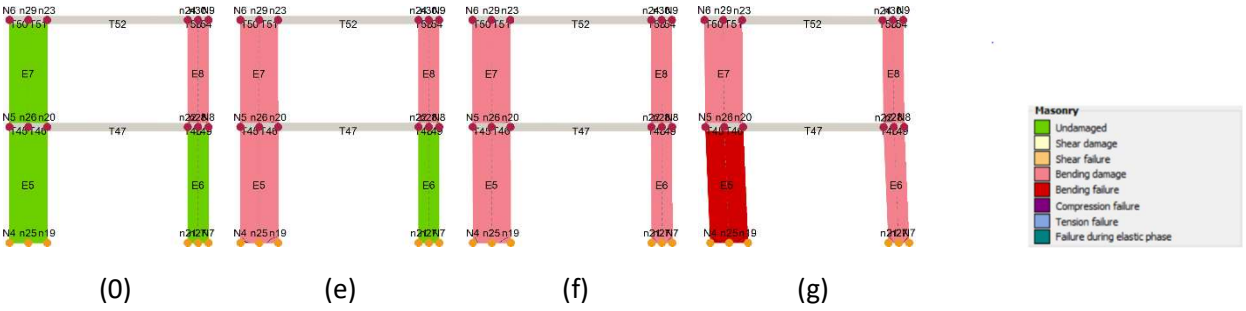

Figure B. 8 Failure progression for 25% load distribution on piers

Appendix C Cantilever wall capacity calculation

Table C. 1 Properties of the cantilever wall

Parameter	Symbol	Units	Value
Length	L	m	0.979
Thickness	T	m	0.1
Height	H	m	2.72
Axial load	N	KN	58.7
Compressive strength	fu	KN/m^2	13390
Shear resistance	τ0	KN/m^2	830

Table C. 2 Flexural capacity of the cantilever wall

Parameter	Symbol	Units	Value
Yielding strain	ε_{cy}	-	0.0014
Masonry ultimate strain	ε_{cu}	-	0.0040
Axial Load	N	KN	58.7
Yielding moment	M_y	KNm	27.02
Length of the compressed zone	$L_{c,u}$	m	0.066
Ultimate moment	M_u	KNm	27.34

Table C. 3 Drift capacity of the cantilever wall

Parameter	Symbol	Units	Value
Yielding curvature	χ_y	m^{-1}	0.00291
Ultimate curvature	χ_u	m^{-1}	0.06083
Shear span	H_0	m	2.72
Yielding displacement	Δ_y	m	0.0009
Plastic length	h_p	m	0.016
Plastic displacement	Δ_p	m	0.0012
Ultimate displacement [Benedetti and Steli]	Δ_u	m	0.0021
Ultimate displacement [Priestley &all]	Δ_u	m	0.0822
Yield drift	θ_y	rad	0.00031
Ultimate drift [Benedetti and Steli]	θ_u	rad	0.00077
Ultimate drift [Priestley &all]	θ_p	rad	0.03021

Appendix D Pier capacity when flange effect is included

Table D. 1 Properties of the URM piers

Parameter	Symbol	Units	Pier			
			WP-GF	NP-GF	WP-FF	NP-FF
Length	L	m	0.979	0.536	0.979	0.536
Thickness	T	m	0.1	0.1	0.1	0.1
Height	H	m	1.42	1.42	1.3	1.3
Axial load	N	KN	62.3	37	32.24	20.8
Compressive strength	fu	KN/m^2	13390	13390	13390	13390
Shear resistance	τ0	KN/m^2	630	630	630	630

Table D. 2 Flexural capacity of the URM piers

Parameter	Symbol	Units	Pier			
			WP-GF	NP-GF	WP-FF	NP-FF
Yielding strain	ε_{cy}	-	0.0014	0.0014	0.0014	0.0014
Masonry ultimate strain	ε_{cu}	-	0.0040	0.0040	0.0040	0.0040
Axial Load	N	KN	60	35	32.24	20.8
Yielding moment	M_y	KNm	27.58	8.77	15.26	5.36
Length of the compressed zone	$L_{c,u}$	m	0.067	0.039	0.036	0.023
Ultimate moment	M_u	KNm	27.91	8.88	15.36	5.40

Table D. 3 Drift capacity of the URM piers

Parameter	Symbol	Units	Pier			
			WP-GF	**NP-GF**	**WP-FF**	**NP-FF**
Yielding curvature	ϕ_y	m^{-1}	0.00291	0.00532	0.00291	0.00532
Ultimate curvature	ϕ_u	m^{-1}	0.05951	0.10202	0.11075	0.17167
Shear span	H_0	m	1.42	1.42	1.30	1.30
Yielding displacement	Δ_y	m	0.0011	0.0020	0.0005	0.0010
Plastic length	h_p	m	0.017	0.009	0.004	0.005
Plastic displacement	Δ_p	m	0.0014	0.0012	0.0006	0.0010
Ultimate displacement [Benedetti and Steli]	Δ_u	m	0.0024	0.0032	0.0011	0.0021
Ultimate displacement [Priestley &all]	Δ_u	m	0.04199	0.03924	0.07378	0.06222
Yield drift	θ_y	rad	0.00075	0.00140	0.00038	0.00078
Ultimate drift [Benedetti and Steli]	θ_u	rad	0.00170	0.00228	0.00082	0.00159
Ultimate drift [Priestley &all]	θ_u	rad	0.01479	0.01382	0.02838	0.02393

References

Ademović, N., & Oliveira, D. V. (2012). *Seismic assessment of a typical masonry residential building in Bosnia and Herzegovina.* Paper presented at the 15th World Conference on Earthquake Engineering.

Bakeer, T. T. (2009). *Collapse analysis of masonry structures under earthquake actions* (Vol. 8): Tammam Bakeer.

Barazza, J. A. C. (2012). *Numerical Model for Nonlinear Analysis of Masonry Walls.* Rheinisch-Westfälischen Technischen Hochschule Aachen, Rheinisch-Westfälischen Technischen Hochschule Aachen.

Benedetti, A., & Steli, E. (2008). Analytical models for shear–displacement curves of unreinforced and FRP reinforced masonry panels. *Construction and Building Materials, 22*(3), 175-185.

Brencich, A., Gambarotta, L., & Lagomarsino, S. (1998). *A macroelement approach to the three-dimensional seismic analysis of masonry buildings.* Paper presented at the 11th European Conference on Earthquake Engineering.

Calvi, G. M., Pinho, R., Magenes, G., Bommer, J. J., Restrepo-Vélez, L. F., & Crowley, H. (2006). Development of seismic vulnerability assessment methodologies over the past 30 years. *ISET journal of Earthquake Technology, 43*(3), 75-104.

Damiola, M., & Pagani, A. (2016). *In-plane behaviour of unreinforced masonry walls: Litarature review and experimental campaign of the Groningen case study.* UNIVERSITA DEGLI STUDI DI BRESCIA.

Del Vecchio, C., Gentile, R., & Pampanin, S. (2017). The Simple Lateral Mechanism Analysis (SLaMA) for the seismic performance assessment of a case study building damaged in the 2011 Christchurch earthquake. University of Canterbury Department of Civil and Natural Resources Engineering. *University of Canterbury technical report*.

EN1996-1-1. (2005). Eurocode 6: Design of masonry structures–Part 1–1: Common rules for reinforced and unreinforced masonry structures.

EN1998-1. (2004). *Eurocode 8: Design of structures for earthquake resistance-Part 1:General rules, seismic actionsand rules for buildings*

EN1998-3. (2005). Eurocode 8: Design of structures for earthquake resistance – Part 3: Assessment and retrofitting of buildings.

Esposito, R., Jafari, S., Ravenshorst, G., Schipper, R., & Rots, J. G. (2018). *Influence of the behaviour of calcium silicate brick and element masonry on the lateral capacity of structures*. Paper presented at the 10th Australasian Masonry Conference, Syd.

Esposito, R., & Ravenshorst, G. (2017). *Quasi-static cyclic in-plane tests on masonry componentsn 2016/2017*. Retrieved from Delft University of Technology:

Esposito, R., Schipper, R., & Ravenshorst, G. (2017). *Structural behavior of a calcium silicate element masonry assemblage: Quasi-static cyclic pushover test*. Retrieved from Delft University of Technology:

Esposito, R., Terwel, K. C., Ravenshorst, G., Schipper, R., Messsali, F., & Rots, J. G. (2017). *CYCLIC PUSHOVER TEST ON AN UNREINFORCED MASONRY STRUCTURE RESEAMBLING A TYPICAL DUTCH TERRACED HOUSE*. Paper presented at the 16th World Conference on Earthquake, 16WCEE 2017, Santiago Chile.

Farshchi, D. M., Motavalli, M., Schumacher, A., & Marefat, M. S. (2009). Numerical modelling of in-plane behaviour of URM walls and an investigation into the aspect ratio, vertical and horizontal post-tensioning and head joint as a parametric study. *Archives of Civil and Mechanical Engineering, 9*(1), 5-27.

Galasco, A., Lagomarsino, S., & Penna, A. (2006). *On the use of pushover analysis for existing masonry buildings.* Paper presented at the Proceedings of the 1st European Conference on Earthquake Engineering and Seismology.

Galasco, A., Lagomarsino, S., Penna, A., & Cattari, S. (2002). TREMURI Program: Seismic Analyser of 3D masonry buildings. *University of Genoa*.

Galasco, A., Lagomarsino, S., Penna, A., & Resemini, S. (2004). *Non-linear seismic analysis of masonry structures.* Paper presented at the Proc. 13th WCEE.

Gupta, A. K. (1992). *Response spectrum method in seismic analysis and design of structures* (Vol. 4): CRC press.

Jafari, S., & Esposito, R. (2017). *Material tests for the characterisation of replicated solid clay brick masonry*. Retrieved from Delft University of Technology:

Kaushik, H. B., Rai, D. C., & Jain, S. K. (2007). Stress-strain characteristics of clay brick masonry under uniaxial compression. *Journal of materials in Civil Engineering, 19*(9), 728-739.

Kilar, V., & Fajfar, P. (1997). Simple push-over analysis of asymmetric buildings. *Earthquake Engineering & Structural Dynamics, 26*(2), 233-249.

Krawinkler, H., & Seneviratna, G. (1998). Pros and cons of a pushover analysis of seismic performance evaluation. *Engineering Structures, 20*(4-6), 452-464.

Lagomarsino, S., Penna, A., Galasco, A., & Cattari, S. (2013). TREMURI program: an equivalent frame model for the nonlinear seismic analysis of masonry buildings. *Engineering Structures, 56*, 1787-1799.

Lourenço, P., Rots, J. G., & Blaauwendraad, J. (1995). Two approaches for the analysis of masonry structures: micro and macro-modeling.

Lourenço, P. B. (1996). Computational strategies for masonry structures.

Magenes, G., & Calvi, G. M. (1997). In-plane seismic response of brick masonry walls. *Earthquake Engineering & Structural Dynamics, 26*(11), 1091-1112.

Magenes, G., Kingsley, G. R., & Calvi, G. M. (1995). *Seismic testing of a full-scale, two-story masonry building: test procedure and measured experimental response*: Consiglio nazionale delle ricerche, Gruppo nazionale per la Difesa dai terremoti.

Moon, F. L., Yi, T., Leon, R. T., & Kahn, L. F. (2006). Recommendations for seismic evaluation and retrofit of low-rise URM structures. *Journal of structural engineering, 132*(5), 663-672.

Mosalam, K., Glascoe, L., & Bernier, J. (2009). Mechanical Properties of Unreinforced Brick Masonry, Section1. *Documented to US Department of Energy by Lawrence Livermore National Laboratory*.

Muir, C. A., Beazley, P. L., Jury, R. D., Kam, W. Y., & den Hertog, P. D. (2017). *Terraced House – Practical application of NZSEE principles in the Netherlands*. Paper presented at the NZSEE Conference.

Ng andu, B. M., Martens, D. R., & Vermeltfoort, A. T. (2006). The contribution of CASIEL infill walls to the shear resistance of steel frames. *HERON-ENGLISH EDITION-, 51*(4), 201.

NZSEE. (2015). Assessment and Improvement of the Structural Performance of Buildings in Earthquakes. Section 10 Revision Seismic Assessment of Unreinforced Masonry Buildings.

NZSEE. (2016). The seismic assessment of existing buildings, Part C8: Seismic assessment of unreinforced masonry buildings. Wellington, New Zealand: MBIE, EQC, SESOC, NZSEE and NZGS.

Panyakapo, P. (2014). Cyclic pushover analysis procedure to estimate seismic demands for buildings. *Engineering Structures, 66*, 10-23.

Penna, A. (2005). Seismic assessment ofmasonry structures by non-linear macro-element analysis.

Petry, S. (2015). Force-displacement response of unreinforced masonry walls for seismic design.

Petry, S., & Beyer, K. (2014). *Flexural deformations of URM piers: Comparison of analytical models with experiments.* Paper presented at the 9th International Masonry Conference.

Priestley, M., Calvi, G., & Kowalsky, M. (2007). Direct displacement based design of buildings: IUSS Press, Pavia, Italy.

Rizzano, G., & Sabatino, R. (2010). *An equivalent frame model for seismic analysis of masonry structures'.* Paper presented at the Proceedings of the 8th National Conference on Seismology and Earthquake Engineering, Aveiro, Portugal.

Roca, P., González, J., Oñate, E., & Lourenço, P. (1998). Experimental and numerical issues in the modelling of the mechanical behaviour of masonry. *Structural Analysis of Historical Constructions II. CIMNE, Barcelona*.

Russell, A., & Ingham, J. (2008). *Flange effects of an unreinforced masonry wall subjected to pseudo-static in-plane seismic forces.* Paper presented at the The 14th World Conference on Earthquake Engineering.

Russell, A., & Ingham, J. (2010). *The influence of flanges on the in-plane seismic performance of URM walls in New Zealand buildings.* Paper presented at the NZSEE Conference.

S.T.A.DATA. (n.d.-a). 3Muri Validation Manual.

S.T.A.DATA. (n.d.-b). User Manual.

Salonikios, T., Karakostas, C., Lekidis, V., & Anthoine, A. (2003). Comparative inelastic pushover analysis of masonry frames. *Engineering Structures, 25*(12), 1515-1523.

Schipper, R., Ham, P., & Ravenshorst, G. (2017). *Proposal of a quasi-static cyclic pushover test on an assembled structure in CS elements*. Retrieved from Delft University of Technology:

Sionti, E. (2016). *Non-linear seismic assessment & retrofitting of unreinforced masonry buildings.* Delft University of Technology.

Themelis, S. (2008). *Pushover analysis for seismic assessment and design of structures.* Heriot-Watt University.

Tomaževič, M. (2009). Shear resistance of masonry walls and Eurocode 6: shear versus tensile strength of masonry. *Materials and structures, 42*(7), 889-907.

Tondelli, M., & Beyer, K. (2014). *Observations on out-of-plane behaviour of URM walls in buildings with RC slabs.* Paper presented at the 9th International Masonry Conference.

USGS. (2017). Earthquake glossary. Retrieved from https://earthquake.usgs.gov/learn/glossary/?term=earthquake

van der Mersch, w. a. (2015). *Modelling of the seismic response of an unreinforced masonry structure.* TU Delft.

van der Voort, N., & Vanclay, F. (2015). Social impacts of earthquakes caused by gas extraction in the Province of Groningen, The Netherlands. *Environmental Impact Assessment Review, 50*, 1-15.

Van Eck, T., Goutbeek, F., Haak, H., & Dost, B. (2006). Seismic hazard due to small-magnitude, shallow-source, induced earthquakes in The Netherlands. *Engineering Geology, 87*(1), 105-121.

Vermeltfoort, A. (2008). *Mechanical properties and application features of CASIELS.* Paper presented at the Proceedings of the 14th International Brick and Block Masonry Conference.

Yi, T. (2004). *Experimental investigation and numerical simulation of an unreinforced masonry structure with flexible diaphragms.* Georgia Institute of Technology.